DOTTORATO DI RICERCA IN

Scienze Applicate a Benessere e Sostenibilità

CICLO XXXVIII

COORDINATORE Prof. Carlo Baldari

TITOLO

Spatio-Temporal Landslide Susceptibility Modeling Using High-Resolution Rainfall and Soil Moisture Data with Machine Learning

Settore Scientifico Disciplinare CEAR-05/A Geotecnica

Dottorando
Dott. Yaser Peiro

Tutor
Prof. Elisabetta Cattoni

Co-Tutor
Dr. Luca Ciabatta

Co-Tutor
Prof. Luigi Lombardo

Spatio-Temporal Landslide Susceptibility Modeling Using High-Resolution Rainfall and Soil Moisture Data with Machine Learning

by

Yaser Peiro

A thesis submitted for the degree of

Doctor of Philosophy in Applied Sciences to Wellness and Sustainability

in the

Department of Theoretical and Applied Sciences, eCampus University, Italy

Supervisors:

Prof. Elisabetta Cattoni

Dr. Luca Ciabatta

Prof. Luigi Lombardo

Cycle XXXVIII(38^{th}) – 2022-2025

Abstract

Shallow landslides threaten communities and infrastructure in mountainous regions, where climate change is intensifying and triggering rainfall events. There is a fundamental limitation for the current landslide detection approaches: methods based solely on rainfall duration and intensity achieve high detection rates but deliver excessive false alarm ratios, while methods using only terrain susceptibility fail to capture the temporal dynamics of triggering events. This persistent problem results in difficulties for the operational deployment of early warning systems. In this direction, the current research aims to develop an integrated machine learning framework that achieves notable false alarm reduction by explicitly coupling static terrain vulnerability with dynamic rainfall and soil moisture conditions.

The methodology is based on a combination of the Random Forest algorithms with high-resolution satellite-derived precipitation and soil moisture data across 7,200 slope units in the northern Apennines of Italy. Using a comprehensive inventory of 412 landslide events documented over five years (2016–2021), the methodology follows three steps: (1) characterization of static environmental controls, including topography, geology, and land cover; (2) integration of dynamic meteorological variables to enable temporal prediction; and (3) development of a novel multi-criteria threshold framework designed to reduce false alarm rates.

The core of the technique is a multi-criteria framework that fundamentally differs from existing approaches by requiring independent exceedance of two separate thresholds before announcing a warning. Unlike conventional methods that apply a single decision criterion—where terrain susceptibility or rainfall duration and intensity exceeds a threshold—the proposed framework implements an AND-logic operator: warnings are issued only when terrain susceptibility exceeds its calibrated threshold and soil moisture and rainfall simultaneously exceed their independent thresholds.

In the current study, the proposed framework was evaluated against two single-criterion approaches that represent current practice: terrain-based thresholds alone and hydrological thresholds alone. The Combined Layers approach, which required simultaneous satisfaction of both criteria, achieved a 73.4% probability of detection with only a 10.8% false alarm ratio, representing a 74% reduction in false alarms compared to hydrological threshold methods and a 49% reduction compared to terrain-based methods. This performance improvement originated from filtering two categories of false alerts: vulnerable slopes experiencing insufficient rainfall and stable slopes withstanding elevated rainfall that their favourable characteristics accommodate. Only in the case of vulnerable terrain encountering critical rainfall and soil moisture, which represents the convergence of independent predisposing and triggering factors, does the system activate warnings.

Overall, the proposed methodology provides a practical pathway toward reliable operational landslide early warning, achieving false alarm rates manageable for civil protection agencies (10.8%) while maintaining detection rates sufficient for public safety (73.4%). Since climate change intensifies extreme precipitation events across vulnerable mountainous regions, the current multi-criteria integration strategy offers a rigorous yet operationally feasible framework for warning systems that balance detection sensitivity with the reliability essential for sustained stakeholder confidence and effective risk reduction.

Acknowledgments

I would like to express my deepest gratitude to my supervisors for their invaluable guidance and unwavering support throughout my doctoral journey. I am profoundly grateful to Prof. Elisabetta Cattoni and Dr. Luca Ciabatta for their continuous mentorship, patience, and encouragement during my PhD studies in Italy. Their expertise and constructive feedback have been instrumental in shaping this research.

I extend special thanks to Prof. Luigi Lombardo for his exceptional guidance and support during my research visit at the University of Twente in the Netherlands. This experience greatly enriched my research perspective and contributed significantly to the development of this work.

I would like to express my sincere appreciation to the Italian National Research Council (CNR-IRPI) for hosting me as a Research Associate for three years and continuing to support me during my doctoral studies. The collaborative environment and resources provided by CNR-IRPI have been essential to this research.

I also wish to thank my family, friends, and colleagues who have supported me in countless ways throughout this journey. Their encouragement and understanding have been invaluable to the completion of this thesis.

Contents

List of Figures

List of Tables

List of Abbreviations

2

API ..... Application Programming Interface

ASCAT ..... Advanced Scatterometer

AUC ..... Area Under the Curve

AVI ..... Aree Vulnerate Italiane

CHELSA ..... Climatologies at High resolution for the Earth's Land Surface Areas

CIESIN ..... Center for International Earth Science Information Network

CLC ..... Corine Land Cover

CNR ..... Consiglio Nazionale delle Ricerche

CPC ..... Climate Prediction Center

CSV ..... Comma-Separated Values

DEM ..... Digital Elevation Model

DTM ..... Digital Terrain Model

DTVT ..... Double Threshold Validation Tool

EPSG ..... European Petroleum Survey Group

ESA ..... European Space Agency

ESACCI ..... ESA Climate Change Initiative

EU ..... European Union

EUMETSAT ..... European Organisation for the Exploitation of Meteorological Satellites

FAR ..... False Alarm Ratio

FN ..... False Negative

FP ..... False Positive

FPR ..... False Positive Rate

GEE ..... Google Earth Engine

GIS ..... Geographic Information System

GLEAM ..... Global Land Evaporation Amsterdam Model

GPM ..... Global Precipitation Measurement

GRASS ..... Geographic Resources Analysis Support System

HSAF ..... Hydrology Satellite Application Facility

IFFI ..... Inventario dei Fenomeni Franosi in Italia

IMERG ..... Integrated Multi-satellitE Retrievals for GPM

IRPI ..... Istituto di Ricerca per la Protezione Idrogeologica

ISPRA ..... Istituto Superiore per la Protezione e la Ricerca Ambientale

ITALICA ..... ITAlian rainfall-induced LandslIdes CAtalogue

KNN ..... K-Nearest Neighbors

LR ..... Late Run

MDA ..... Mean Decrease Accuracy

MDG ..... Mean Decrease Gini

METOP ..... Meteorological Operational Satellite

ML ..... Machine Learning

MODIS ..... Moderate Resolution Imaging Spectroradiometer

NASA ..... National Aeronautics and Space Administration

NDVI ..... Normalized Difference Vegetation Index

NDWI ..... Normalized Difference Water Index

NOAA ..... National Oceanic and Atmospheric Administration

NSIDC ..... National Snow and Ice Data Center

OOBE ..... Out-of-Bag Error

POD ..... Probability of Detection

RBF ..... Radial Basis Function

RF ..... Random Forest

ROC ..... Receiver Operating Characteristic

SAR ..... Synthetic Aperture Radar

SLTPPT ..... Silt Percentage

SM2RAIN ..... Soil Moisture to Rain

SMAP ..... Soil Moisture Active Passive

SNR ..... Signal-to-Noise Ratio

SRTM ..... Shuttle Radar Topography Mission

SVM ..... Support Vector Machine

TN ..... True Negative

TP ..... True Positive

UNESCO ..... United Nations Educational, Scientific and Cultural Organization

USGS ..... United States Geological Survey

Chapter 1

Introduction

Landslides represent one of the most destructive natural hazards worldwide, resulting in substantial annual economic, societal, and environmental consequences along with fatalities (Bubeck et al., 2025; Froude and Petley, 2018; Kirschbaum et al., 2015). Climate change and environmental shifts point to growing landslide hazards of particularly fast-moving, rainfall-induced landslides (Ozturk et al., 2022; Gariano and Guzzetti, 2016). Reliable landslide predictions are foundational for landslide early warning systems (LEWS) and can help reduce the impacts of landslides. Thus, ensuring reliable predictions of landslides and their resultant impacts is paramount. Nevertheless, the success of such predictions is intrinsically linked to a comprehensive understanding of the underlying factors driving slope instability.

The evolution of landslide forecasting methodologies reflects a progressive sophistication in both theoretical understanding and computational capabilities. Early approaches were dominated by physically based models that employed intricate mathematical relationships to reproduce the physical processes leading to slope instability (Montgomery and Dietrich, 1994a; Baum et al., 2008; Rossi et al., 2013; Medina et al., 2021; Bout et al., 2018; Reid et al., 2015). Although these models offer high accuracy through faithful representation of underlying mechanisms, their extensive hydrological and geotechnical parameter requirements render them suitable primarily for slope or catchment-level applications, with limited scalability to regional assessments due to extreme parameter heterogeneity. As a result, the application of such models is often confined to small scale scenarios (Bicocchi et al., 2019; Alvioli and Baum, 2018; Corominas et al., 2014).

The recognition of these scalability limitations catalyzed a methodological shift toward

empirical and statistical approaches, particularly rainfall threshold models, which bypass complex physical processes to establish empirical relationships between precipitation triggers and landslide outcomes (Martelloni et al., 2012). Since Caine (1980) pioneering work, rainfall thresholds have evolved to become the predominant tool in landslide forecasting literature, representing critical precipitation levels that can trigger slope instability (Guzzetti et al., 2008a; Segoni et al., 2018a; Piciullo et al., 2018a; Dixit et al., 2024; Semnani et al., 2025; Cavagnaro et al., 2025). Their operational advantages—rapid response capability, adequate regional-scale accuracy, and straightforward implementation—have established rainfall thresholds as the current state-of-the-art for regional LEWS assessments (Segoni et al., 2018a).

However, this methodological pragmatism comes with significant theoretical limitations. Rainfall threshold models depend fundamentally on a single triggering process, systematically neglecting the influence of other factors that can substantially contribute to landslide initiation, including soil moisture conditions, snowmelt contributions, and antecedent hydrological states (Piciullo et al., 2018a; Gariano et al., 2020). This reductionist approach, while operationally expedient, fails to capture the multivariate nature of landslide triggering processes and limits the models' ability to adapt to changing environmental conditions or to provide insights into the underlying physical mechanisms governing slope stability.

The emergence of machine learning (ML) methodologies in the early 2000s marked a paradigmatic shift in landslide research, offering the potential to transcend the limitations of both physically based and simple statistical approaches (Lee et al., 2003; Brenning, 2005; Ermini et al., 2005; Catani et al., 2013; Pham et al., 2016; Reichenbach et al., 2018a; Merghadi et al., 2020a; Liu et al., 2021). The fundamental advantage of ML lies in its skill to process extensive, multidimensional datasets and identify complex, non-linear relationships among variables that may escape conventional statistical methods. This capability has proven particularly valuable in landslide susceptibility mapping (LSM), where algorithms can integrate several conditioning factors—geomorphological characteristics, thematic factors, hydrological parameters, and proximity variables—to produce spatial probability assessments of landslide occurrence (Catani et al., 2013; Micheletti

et al., 2014; Reichenbach et al., 2018a; Frodella et al., 2022; Rosi et al., 2023b; Lima et al., 2022a).

The proliferation of ML applications in landslide research has been remarkable, with studies demonstrating the effectiveness of various algorithms including support vector machines, artificial neural networks, Random Forest (RF), and ensemble methods in producing landslide susceptibility maps. Advanced ML techniques have further enhanced interpretability through sophisticated feature importance measures, including Out-of-Bag Error (OOBE), Partial Dependence Plots (PDPs), and Shapley values, enabling researchers to quantify variable influence on model predictions and validate algorithmic logic against physical understanding (Catani et al., 2013; Rosi et al., 2023b; Dahal and Lombardo, 2023).

Despite these advances, a critical limitation persists across the vast majority of ML applications in landslide research: the fundamental focus on spatial probability assessment without temporal consideration. Landslide susceptibility maps express only the spatial probability of landslide occurrence in response to natural or anthropogenic factors, explicitly excluding temporal probability assessment (Brabb, 1995; Fell et al., 2008). This temporal blindness stems from the classic static approach employed in susceptibility analyses, which treats conditioning factors as time-invariant characteristics of the landscape. The main triggering factors for the initiation of landslides are two: short-duration and intense rainfall for shallow landslides and debris flow, resulting in rapid infiltration of abundant water into the top decimeters of soil and the consequent increase in water pressure; and antecedent rainfalls for deep-seated landslides, as they require longer infiltration times, but can also influence shallow landslides and debris flow initiation (Guzzetti et al., 2008a; Martelloni et al., 2012; Kim et al., 2021; Pereira et al., 2012; Giannecchini et al., 2012; Di Napoli et al., 2021). In addition, other highly influential but less explored triggering factors are soil moisture, which can decrease the rainfall needed to induce slope failure (Rosi et al., 2021; Kim et al., 2021; Piciullo et al., 2022); snowmelt, which increases the amount of infiltrated water (Camera et al., 2021; Gariano and Guzzetti, 2016; Krøgli et al., 2018), and the shaking effect due to seismic activity (Pyakurel et al., 2023; Rosi

et al., 2023b; Schilirò et al., 2023). Such dynamic features cannot be directly used as model input parameters for susceptibility mapping due to their time dependency, which is inconsistent with the classic static approach used in susceptibility analyses. Therefore, although LSMs are accurate, simple, and quick to develop, they are challenging to implement in LEWS due to their limitations in temporal forecasting and find more applications in urban planning.

The recognition of this temporal limitation has sparked recent efforts to incorporate dynamic elements into landslide prediction frameworks. Segoni et al. (2018b) combine the susceptibility map with rainfall thresholds to develop a hazard matrix to obtain a spatial and temporal definition of landslide hazard. This technique has also been adopted by other authors (Park et al., 2019; Lu et al., 2020; Pecoraro and Calvello, 2021; Palau et al., 2022). Alternatively, some authors applied various machine learning models exclusively for rainstorm-induced (Ng et al., 2021; Liu et al., 2021) or earthquake-induced (Lombardo and Tanyas, 2020; Pyakurel et al., 2023; Dahal and Lombardo, 2023) landslide inventories, using the associated dynamic variables, to obtain a landslide probability map valid only for such events. Distefano et al. (2022) introduces an innovative methodology for a dynamic application of the Artificial Neural Networks algorithm. This approach is not directly related to landslide probability mapping, but it aims to automatically detect the intensity-duration rainfall thresholds with the highest performance by feeding the model with a spatially and temporally explicit landslides database. These works represent significant advancements compared to traditional static machine learning approaches and serve as a promising starting point towards the main objective: mapping the spatiotemporal landslide probability using machine learning techniques.

However, the spatiotemporal prediction of landslides combining static and dynamic parameters in ML algorithms is still in a preliminary phase (Collini et al., 2022; Distefano et al., 2022). At present, and to the best of our knowledge, only a few studies have successfully produced a landslide probability map through ML. For instance, studies have focused on selecting non-landslide cells across space and time, enabling the inclusion of snow water equivalent and soil moisture content data as dynamic input parameters for

ML models; mapping the landslide probability on a global scale (Li et al., 2022).

This limited progress reflects several fundamental challenges that have constrained the development of truly dynamic landslide prediction systems. First, the existing literature lacks comprehensive exploration of spatiotemporal identification of non-landslide events, a critical requirement for training ML algorithms that must distinguish between landslide and stable conditions across both space and time. Second, established procedures for calibrating dynamic ML models to generate landslide probability maps with optimal predictive capabilities remain undeveloped. Third, validation methodologies and probability threshold definition for operational warning purposes have not been systematically addressed. Finally, the integration of diverse dynamic variables—including soil moisture, snowmelt, antecedent precipitation, and seasonal factors—requires sophisticated temporal sampling strategies that extend beyond conventional susceptibility mapping approaches.

These methodological gaps represent not merely technical challenges but fundamental barriers to operational implementation of ML-based spatiotemporal landslide forecasting systems. The transition from static susceptibility assessment to dynamic probability prediction requires a comprehensive reconceptualization of how landslide prediction models are constructed, calibrated, and validated. This transformation must address the inherent tension between the spatial focus of traditional susceptibility mapping and the temporal requirements of early warning systems, while maintaining the interpretability and physical consistency that are essential for operational acceptance.

The research presented in this thesis addresses these fundamental challenges through the development of a novel methodology for spatiotemporal landslide forecasting using ML approaches. The central innovation lies in the systematic integration of spatially and temporally explicit landslide inventories with dynamic environmental variables through RF algorithms, enabling the production of landslide probability maps that incorporate both spatial predisposition and temporal triggering factors. The RF approach was selected for its robust handling of mixed data types, built-in feature importance measures

(OOBE and PDPs), and demonstrated performance in environmental modeling applications (Liaw and Wiener, 2002; Friedman, 2001).

The methodology developed herein transcends existing approaches by implementing a comprehensive framework for spatiotemporal identification of both landslide and non-landslide events, enabling the integration of dynamic variables as primary model inputs rather than secondary constraints. This approach necessitates the employment of spatially and temporally explicit landslide inventories that provide precise dating of landslide events, a requirement that has limited previous research but is essential for training algorithms capable of capturing the temporal dynamics of landslide initiation processes.

1.1 Research Objective

This research focuses on developing and applying dynamic RF models for landslide prediction, utilizing a case study in Italy to demonstrate the methodology's effectiveness across different geographical and geological contexts. The primary goal of this work is to advance spatiotemporal landslide susceptibility mapping by incorporating both static geo-environmental factors and dynamic meteorological variables into predictive models.

The main objectives of this thesis are threefold:

Characterizing static environmental controls on shallow landslide occurrence: This research examines how various environmental factors, including topographic characteristics (slope, aspect, elevation), geological properties (lithology, structural features), and land cover conditions, control shallow landslide susceptibility. A thorough understanding of these fundamental controls provides the foundation for robust predictive modeling and ensures that the dynamic components are built upon solid physical understanding.

Integrating dynamic precipitation and soil moisture conditions into susceptibility assessment: The work incorporates dynamic meteorological variables, particularly rainfall patterns and soil moisture variations, into the susceptibility assessment

framework. This integration allows the model to capture the temporal evolution of landslide hazard in response to triggering events, transitioning from static susceptibility maps toward dynamic risk assessment that reflects real-world conditions.

Developing a Double Threshold Validation Framework for Improving Landslide Prediction Accuracy: The thesis establishes a methodological approach for analyzing landslide susceptibility changes over time, with particular attention to reducing false alarm rates in both landslide-prone and stable locations. This framework incorporates preparatory factors, including antecedent soil moisture conditions, to better distinguish between landslide and non-landslide events during critical periods.

The work contributes to landslide susceptibility mapping by demonstrating how ML techniques, specifically RF algorithms, can effectively integrate spatiotemporal data to improve prediction accuracy. The resulting methodology provides more comprehensive hazard assessment tools that account for both spatial predisposition and temporal variability, offering practical applications for risk management and land-use planning in landslide-prone regions.

1.2 Structure of Thesis

The thesis is organized to align with its sub-objectives, where each chapter serves as a building block for the next, forming a cohesive research narrative. The chapters are interconnected, addressing specific aspects of landslide susceptibility modeling and prediction. Chapter 2 establishes the theoretical foundation for landslide susceptibility modeling. It examines shallow landslide processes, reviews existing modeling approaches, and introduces the data-driven machine learning methods used in this study. Chapter 3 addresses the first research sub-objectives, characterizing static environmental controls on shallow landslide occurrence. It integrates dynamic factors, such as precipitation and soil moisture conditions, into susceptibility assessments and describes the machine learning algorithms applied. Chapter 4 develops a temporal framework to enhance the accuracy of landslide predictions by incorporating time-dependent factors. Chapter 5 presents a

Double Threshold Validation Framework designed to improve landslide prediction accuracy and reduce false alarm rates, a key objective of this research. Chapter 6 provides the conclusions of the study, summarizing the findings and contributions of the research. Future perspective and next steps are here presented as well.

Chapter 2

Theoretical Background and Methodological Framework

This chapter establishes the theoretical foundation for spatiotemporal landslide susceptibility modeling by examining shallow landslide processes, reviewing modeling approaches, and introducing the machine learning framework employed in this research. The chapter progresses from fundamental landslide concepts through methodological evolution to the specific algorithms and integration strategies that form the basis of this study.

2.1 Shallow Landslides: Characteristics and Mechanisms

2.1.1 Definition and Classification Framework

Landslides represent one of the most significant and widespread geomorphological processes controlling landscape evolution across diverse environmental settings. These phenomena constitute complex mass wasting processes during which soil and rock materials composing hillslopes are displaced downward under the predominant influence of gravitational forces (Varnes, 1978; Hungr et al., 2014). The fundamental mechanism underlying all landslide processes involves the critical moment when forces acting on a slope exceed the available strength of the constituent materials, initiating downward movement that can range from imperceptibly slow creep to catastrophically rapid flows (Hungr et al., 2014). The scientific understanding of landslides has evolved significantly since early

attempts to describe and classify these phenomena. The complexity and diversity of gravitational mass movements have led to numerous classification systems, each developed according to specific criteria and objectives. Among the most influential and widely adopted frameworks, the classification proposed by Varnes (Varnes, 1978) provided a foundational definition: "a downward and outward movement of a mass of rock, debris, or earth down a slope, under the influence of gravity." This seemingly simple definition encompasses the fundamental physical process while acknowledging the diverse materials, mechanisms, and scales involved in landslide phenomena (Cruden and Varnes, 1996; Hungr et al., 2014). The evolution of landslide classification systems reflects the growing complexity of scientific understanding and the need for standardized terminology across different disciplines. The original Varnes classification was subsequently modified and updated (Cruden and Varnes, 1996) to address limitations and incorporate new understanding of slope failure mechanisms. The modified Varnes classification, approved by the IAEG Commission UNESCO Working Party on World Landslide Inventory, represents a comprehensive framework that considers multiple aspects of mass movements including material properties, movement types, activity levels, distribution patterns, and style characteristics (Hungr et al., 2014). Two prominent classification paradigms have emerged within the scientific community: the system proposed by Hutchinson (Hutchinson, 1968; Hungr et al., 2001) and the framework developed by Varnes (Varnes, 1978; Cruden and Varnes, 1996). While these classification schemes share fundamental similarities in recognizing basic movement types, they differ in emphasis and organizational structure. Hutchinson's approach tends to privilege the kinematic characteristics and type of movement, providing detailed subdivision based on mechanical behavior and movement patterns. Conversely, Varnes' system focuses more comprehensively on the conditions and contexts of slope failure, incorporating broader consideration of predisposing and triggering factors (Lu and Godt, 2013a; Hungr et al., 2014). Both classification systems recognize five primary types of movement: falls, topples, slides, spreads, and flows. Each category encompasses distinct mechanical processes and characteristic behaviors.

Falls involve detachment and free-fall or bouncing movement of rock or debris. Top-

ples describe forward rotation of units about pivotal points. Slides encompass movement along discrete failure surfaces, which can be planar, curved, or irregular. Spreads involve lateral extension and subsidence of coherent rock or soil masses. Flows represent continuous deformation and movement resembling viscous fluid behavior (Cruden and Varnes, 1996; Hungr et al., 2014). Within this more inclusive classification scheme, shallow landslides represent a particularly significant subset that has attracted considerable scientific attention due to their widespread occurrence and substantial impact on human activities. Although not explicitly defined as a separate category in classical classification systems, shallow landslides can be characterized as predominantly translational slides affecting surficial soil layers with limited thickness, typically ranging between 0.5 and 2.0 meters (Bandis et al., 1996; Mason and Little, 2002; Sidle and Bogaard, 2006; Lagomarsino et al., 2017). These phenomena generally develop within unconsolidated or weakly consolidated materials overlying more competent bedrock or substantially stronger substrate materials. The geometric characteristics of shallow landslides distinguish them from deeper-seated slope failures in several important ways. The failure surfaces are typically parallel or sub-parallel to the ground surface, following the contact between surficial materials and underlying substrate or developing within zones of weakness such as the interface between different soil horizons. The relatively shallow depth of these failures results in high length-to-depth ratios, often exceeding 10:1, which influences both the mechanical behavior during failure and the potential for post-failure transformation into flow- like movements (Montgomery and Dietrich, 1994b; Hungr et al., 2014). Figure 2.1 presents a comprehensive classification framework that integrates multiple dimensions of landslide characterization, including material type, movement mechanism, and activity state.

Type of Movement	Material Classification			Activity Classification			First Movement				Second Movement			
	Material Type			State	Distribution	Style	Rate	Water	Material	Type	Rate	Water	Material	Type
	Bedrock	Coarse Soils	Fine Soils	Primary	Spatial	Pattern	Velocity	Content	Type	Motion	Velocity	Content	Type	Motion
Fall	Rock fall	Debris fall	Earth fall	Active	Advancing	Complex	Extremely rapid	Dry	Rock	Fall	Extremely rapid	Dry	Rock	Fall
Topple	Rock topple	Debris topple	Earth topple	Reactivated	Retrogressive	Composite	Very rapid	Moist	Soil	Topple	Very rapid	Moist	Soil	Topple
Slide	Rock slide	Debris slide	Earth slide	Suspended	Widening	Multiple	Rapid	Wet	Earth	Slide	Rapid	Wet	Earth	Slide
Spread	Rock spread	Debris spread	Earth spread	Inactive	Enlarging	Successive	Moderate	Very wet	Debris	Spread	Moderate	Very wet	Debris	Spread
Flow	Rock flow	Debris flow	Earth flow	Dormant	Confined	Single	Slow	—	—	Flow	Slow	—	—	Flow
Extended Activity	—	—	—	Abandoned	Diminishing	—	Very slow	—	—	—	Very slow	—	—	—
Stabilized States	—	—	—	Stabilized	Moving	—	Extremely slow	—	—	—	Extremely slow	—	—	—
Relict	—	—	—	Relict	—	—	—	—	—	—	—	—	—	—

Classification Categories Legend:

Material Classification Activity Classification First Movement Second Movement

Figure 2.1: Comprehensive landslide classification system integrating material composition, activity states, and movement characteristics(Lombardo, 2015)

2.1.2 Mechanical Framework and Failure Mechanisms

The mechanical framework governing shallow landslide initiation and development is fundamentally rooted in classical soil mechanics and slope stability principles. The limit-equilibrium concept provides the theoretical foundation for understanding failure conditions, defining the critical state when shear stresses acting along potential failure surfaces reach equality with the available shear strength of the involved materials. This equilibrium condition represents the threshold between stable and unstable slope configurations, with failure occurring when driving forces exceed resisting forces by any margin (Terzaghi, 1950; Duncan, 1996). The infinite slope model represents the most widely applied analytical framework for shallow landslide analysis due to its appropriate geometric assumptions and mathematical formulation. This model considers slopes of theoretically infinite extent with uniform properties and consistent conditions at any given depth below the surface. All forces are assumed to act either normal or parallel to the slope surface, simplifying the complex three-dimensional stress state to a more manageable two- dimensional problem. Under these assumptions, the factor of safety can be expressed as the ratio of available shear strength to applied shear stress along potential failure planes (Milledge et al., 2014; Montgomery and Dietrich, 1994b). The factor of safety calculation incorporates several critical components including effective stress conditions, soil strength parameters and geometric factors. The effective stress principle governs the mechanical behavior of soils, recognizing that soil strength depends on effective normal stress, which represents total stress minus pore water pressure. This relationship proves particularly crucial for understanding rainfall-induced slope failures, as changes in pore water pressure directly influence effective stress conditions and consequently affect slope stability (Fredlund and Rahardjo, 1993; Lu and Godt, 2013b).

Soil strength parameters include both cohesive and frictional components, typically expressed through the Mohr-Coulomb failure criterion. Cohesion represents the intrinsic bonding between soil particles, including both true cohesion from chemical and physical bonding and apparent cohesion from soil suction in unsaturated conditions. The friction

angle reflects the internal friction characteristics of the soil, related to particle shape, size distribution, density, and mineralogical composition. These parameters exhibit substantial spatial and temporal variability, contributing to the complexity of slope stability assessment (Fredlund and Rahardjo, 1993; Lu and Godt, 2013b). Soil strength parameters include both cohesive and frictional components, typically expressed through the Mohr-Coulomb failure criterion. Cohesion represents the intrinsic bonding between soil particles, including both true cohesion from chemical and physical bonding and apparent cohesion from soil suction in unsaturated conditions. The friction angle reflects the internal friction characteristics of the soil, related to particle shape, size distribution, density, and mineralogical composition. These parameters exhibit substantial spatial and temporal variability, contributing to the complexity of slope stability assessment (Fredlund and Rahardjo, 1993; Lu and Godt, 2013b). The role of water in shallow landslide mechanisms cannot be overstated, as hydrological processes represent the primary triggering mechanism for most shallow slope failures. Water influences slope stability through multiple interconnected mechanisms, including increased unit weight of soil mass, reduced effective stress through elevated pore water pressures, decreased apparent cohesion in unsaturated soils, and enhanced weathering processes that degrade soil strength over time (Iverson, 2000; Lu and Godt, 2013b). Rainfall-induced landslides develop through complex infiltration processes that depend on rainfall characteristics, soil properties, initial moisture conditions, and topographic factors. During rainfall events, water infiltration increases soil moisture content and raises pore water pressures within the soil mass. In initially unsaturated soils, infiltration may initially increase stability by enhancing apparent cohesion through increased soil suction. However, continued infiltration eventually leads to saturation of critical zones, eliminating beneficial suction effects and creating positive pore water pressures that reduce effective stress and trigger failure (Iverson, 2000; Lu and Godt, 2013b).

The temporal evolution of pore pressure during rainfall events follows patterns that depend on rainfall intensity, duration, and distribution, as well as soil hydraulic properties including saturated hydraulic conductivity, water retention characteristics, and initial

moisture conditions. High-intensity, short-duration rainfall events may trigger failures through rapid pore pressure increases in near-surface layers, while prolonged, moderate-intensity events can lead to deeper moisture penetration and potentially more extensive failures (Iverson, 2000).

2.1.3 Conditioning and Triggering Factors

The comprehensive understanding of shallow landslide occurrence requires careful distinction between conditioning factors and triggering factors, as these two categories of influences operate on different temporal scales and through different mechanisms. This distinction, while conceptually clear, involves complex interactions in natural systems where multiple factors operate simultaneously across various time scales. Conditioning factors represent the intrinsic characteristics and long-term processes that establish the predisposition or susceptibility of slopes to failure under appropriate triggering conditions. These factors operate over extended time periods, ranging from years to geological time scales, and gradually modify slope stability conditions without necessarily causing immediate failure. The cumulative effects of conditioning factors determine the background stability state and establish the threshold conditions required for failure initiation. Topographic conditioning factors encompass slope geometry, drainage patterns, and morphological characteristics that influence stress distributions and hydrological processes. Slope angle represents the most fundamental topographic parameter, directly controlling gravitational stress components and influencing surface and subsurface water flow patterns. Steeper slopes experience higher gravitational driving forces, while gentler slopes may be more susceptible to prolonged moisture retention and gradual strength degradation.

Slope aspect affects solar radiation receipt, evapotranspiration rates, and prevailing weather exposure, creating microclimatic variations that influence moisture regimes and weathering processes (Fell et al., 2008; Guzzetti et al., 2006). Geological conditioning factors include bedrock lithology, structural features, weathering characteristics, and soil properties that control material strength and hydrological behavior. Bedrock geology influences groundwater flow patterns, weathering rates, and the characteristics of overlying soil

materials. Structural features such as fracture systems, bedding planes, and joint orientations create planes of weakness that may control failure surface development. The degree and nature of bedrock weathering determine the thickness and properties of surficial materials susceptible to shallow landsliding (Cruden and Varnes, 1996; Hungr et al., 2014). Soil properties represent critical conditioning factors that directly control slope stability through their influence on strength parameters and hydrological behavior. Soil texture, structure, density, and mineralogical composition determine hydraulic conductivity, water retention characteristics, and strength parameters. Fine-grained soils with high clay content may exhibit significant strength variations with moisture content changes, while coarse-grained soils typically show more consistent behavior but may be susceptible to rapid drainage and suction loss during intense rainfall (Fredlund and Rahardjo, 1993; Lu and Godt, 2013b). Vegetation characteristics constitute important conditioning factors through multiple mechanisms affecting both mechanical stability and hydrological processes. Root systems provide mechanical reinforcement through tensile strength and apparent cohesion enhancement, with effectiveness depending on root density, distribution, and tensile properties. Vegetation influences surface hydrology through interception, evapotranspiration, and modification of infiltration patterns.

Canopy effects on rainfall distribution and energy dissipation can significantly alter moisture inputs to slopes. However, vegetation effects are complex and sometimes contradictory, as tree loading may destabilize slopes under certain conditions, and root decay following vegetation removal can create temporary weakness zones (Masi et al., 2021; Schwarz et al., 2010; Roering et al., 2003). Human activities represent increasingly important conditioning factors in many environments, modifying natural slope conditions through construction activities, land use changes, and infrastructure development. Cut and fill operations alter natural slope geometries and drainage patterns, potentially creating unstable configurations. Deforestation and agricultural practices modify vegetation cover and associated hydrological and mechanical effects. Urban development introduces additional loading, modifies surface drainage, and may alter groundwater flow patterns (Guzzetti et al., 2006; Reichenbach et al., 2018b).

Triggering factors represent the immediate processes or events that disrupt the existing force equilibrium and initiate slope failure. Unlike conditioning factors, triggers operate over short time periods, ranging from minutes to seasons, and cause rapid changes in slope stability conditions. The most common triggering mechanism for shallow landslides involves rainfall events that modify pore water pressure conditions and reduce effective stress along potential failure surfaces (Guzzetti et al., 2008b; Iverson, 2000). Rainfall triggering mechanisms operate through several interconnected processes that depend on rainfall characteristics, initial slope conditions, and soil properties. Rainfall intensity affects infiltration rates and the depth of moisture penetration during events. High-intensity rainfall may exceed soil infiltration capacity, leading to surface runoff and reduced infiltration effectiveness.

Conversely, moderate-intensity rainfall over extended periods may achieve deeper penetration and more effective pore pressure increases. Rainfall duration determines the total moisture input and the time available for infiltration and pressure equilibration processes (Guzzetti et al., 2008b). Antecedent rainfall conditions significantly influence triggering effectiveness by establishing initial moisture states and pore pressure conditions. Dry antecedent conditions may require substantial rainfall amounts to achieve critical moisture levels, while wet antecedent conditions may result in rapid failure initiation with relatively modest additional rainfall inputs. The temporal distribution of antecedent rainfall affects its influence, with recent rainfall typically having greater impact than rainfall occurring weeks or months previously (Guzzetti et al., 2008b). Earthquake triggering represents another significant mechanism, particularly in seismically active regions. Ground acceleration during seismic events increases shear stresses on slopes while simultaneously reducing effective stress through dynamic pore pressure increases in saturated materials. The effectiveness of seismic triggering depends on earthquake magnitude, duration, frequency content, and distance from the epicenter, as well as local site conditions including topographic amplification effects and soil properties (Keefer, 1984). Other triggering mechanisms include rapid snowmelt, which can provide intense hydrological loading similar to heavy rainfall, freeze-thaw processes that may alter soil properties and create

hydraulic pressures, and human activities such as construction operations or utility failures that rapidly alter slope loading or drainage conditions (Guzzetti et al., 2006).

2.2 Landslide Susceptibility Modeling Approaches

2.2.1 Conceptual Framework and Theoretical Foundations

Landslide susceptibility modeling represents a fundamental component of comprehensive landslide risk assessment, addressing the critical question of spatial probability for slope failure occurrence. The concept of landslide susceptibility is formally defined as "the likelihood of a landslide occurring in an area on the basis of local terrain conditions" (Brabb, 1984), representing the degree to which terrain can be affected by future slope movements based on the spatial distribution of conditioning factors that have controlled past landslide occurrences (Reichenbach et al., 2018b). The theoretical framework underlying landslide susceptibility assessment rests on four fundamental assumptions that provide the scientific validity and operational foundation for these approaches (Guzzetti et al., 2006; Reichenbach et al., 2018b).

The first assumption establishes that slope failures leave discernible features that can be recognized, classified, and mapped through field investigations or remote sensing techniques, particularly stereoscopic aerial photography interpretation. This assumption enables the compilation of comprehensive landslide inventories that form the empirical foundation for susceptibility modeling efforts.

The second fundamental assumption recognizes that landslides are controlled by mechanical laws that can be determined through empirical, statistical, or deterministic approaches. This principle acknowledges that conditions causing landslides, whether directly or indirectly linked to slope failures, can be systematically collected, quantified, and utilized to construct predictive models of landslide occurrence (Carrara et al., 1991a,b).

The third assumption embodies the principle that "for landslides, the past and present are

keys to the future," implying that future slope failures will be more likely to occur under conditions similar to those that led to past and present instability. This uniformitarian principle provides the temporal framework for susceptibility assessment, suggesting that understanding past failures is essential for assessing future landslide hazard. The assumption enables the use of historical landslide information to predict future spatial patterns of slope instability.

The fourth assumption establishes that landslide occurrence, whether in space or time, can be inferred from heuristic investigations, computed through analysis of environmental information, or derived from physical models. This principle enables territorial zoning into susceptibility or hazard classes ranked according to different probabilities of landslide occurrence, providing the operational framework for practical susceptibility mapping applications (Fell et al., 2008). The evolution of landslide susceptibility modeling has been profoundly influenced by technological advances, particularly the development and widespread adoption of Geographic Information Systems (GIS) technology. Since its emergence several decades ago, GIS has revolutionized spatial data management across numerous scientific disciplines, including landslide susceptibility assessment. The ability to collect, manipulate, and analyze diverse spatial and non-spatial data related to landslide geometries, extent, recognition, and causal factors within integrated digital environments has enabled unprecedented advances in susceptibility modeling capabilities.

The integration of multiple data types within GIS environments has facilitated sophisticated analytical approaches that were previously impossible or impractical. These capabilities include complex spatial calculations, advanced statistical analyses, and implementation of various methodological approaches that have led to continuous improvements in landslide susceptibility assessment accuracy and reliability (Carrara et al., 1991a; Nagarajan et al., 1998; Conoscenti et al., 2008). Contemporary susceptibility modeling approaches encompass a broad spectrum of methodologies that can be categorized into three primary paradigms: knowledge-driven methods that rely on expert judgment and qualitative assessment, data-driven methods that utilize statistical or machine learning techniques to identify quantitative relationships between conditioning factors and land-

slide occurrence, and physically based methods that apply mechanistic models to simulate slope failure processes based on physical laws and material properties (Reichenbach et al., 2018b; Merghadi et al., 2020b). The selection among these methodological approaches depends on multiple factors including data availability and quality, spatial scale of analysis, intended applications, available expertise and computational resources, and specific objectives of the susceptibility assessment. Each approach offers distinct advantages and limitations that must be carefully considered in relation to project requirements and constraints. The spatial scale of susceptibility assessment represents a critical consideration that influences methodological selection and implementation strategies. Local-scale assessments, typically covering individual slopes or small watersheds, enable detailed investigation of site-specific processes and conditions but require intensive data collection and analysis efforts. Regional-scale assessments, covering watersheds to entire mountain ranges, provide broader territorial coverage for planning applications but must rely on generalized data sources and simplified analytical approaches.

2.2.2 Knowledge-Driven Versus Data-Driven Methods

The methodological landscape for landslide susceptibility assessment encompasses two fundamentally different paradigmatic approaches that reflect distinct philosophical perspectives on understanding and predicting slope failure patterns. Knowledge-driven methods emphasize expert understanding and qualitative assessment of geomorphological processes, while data-driven methods focus on quantitative analysis of empirical relationships derived from observational data (Van Westen et al., 2008; Carrara et al., 1991a; Reichenbach et al., 2018b). Knowledge-driven methods encompass direct geomorphological mapping, inventory-based analysis, and spatial multi-criteria evaluation techniques that rely fundamentally on expert judgment and professional experience. These approaches utilize comprehensive understanding of complex processes governing landslide occurrence that cannot be easily quantified through purely statistical methods. The theoretical foundation rests on the premise that experienced professionals can recognize subtle geomorphological indicators, appreciate process interactions, and integrate diverse forms of evidence

including field observations and historical information (Ozturk et al., 2022; Van Westen et al., 2008; Fell et al., 2008). Direct geomorphological mapping represents the most traditional approach, involving detailed field investigation and interpretation of landslide features and terrain characteristics. Spatial multi-criteria evaluation techniques provide frameworks for systematically combining expert knowledge about multiple conditioning factors through structured weight assignment procedures. These methods prove particularly valuable in data-poor environments where insufficient quantitative information exists to support sophisticated statistical approaches. The advantages of knowledge-driven approaches include their ability to incorporate comprehensive geomorphological understanding extending beyond quantifiable variables, flexibility in addressing diverse terrain conditions, and capability to integrate qualitative observations and local expertise. However, significant limitations include the subjective nature of expert judgment that may affect reproducibility, dependency on expert quality and experience, and challenges in documentation and validation of qualitative assessments (Lima et al., 2022b). Data-driven methods represent a paradigmatic approach emphasizing systematic identification and quantification of empirical relationships between conditioning factors and landslide occurrence patterns through statistical analysis and machine learning techniques (Carrara et al., 1991a; Van Westen et al., 2008; Reichenbach et al., 2018b). The theoretical foundation rests on two fundamental assumptions: that future landslide occurrences are more likely under conditions similar to past events, and that landslide occurrence can be modeled through systematic analysis of environmental variables. Data-driven algorithms can be categorized into statistically-based methods (discriminant analysis, logistic regression, generalized additive models) that rely on established mathematical relationships, and machine learning techniques that utilize pattern recognition capabilities (Brenning, 2005; Micheletti et al., 2014; Merghadi et al., 2020b). Statistical methods provide interpretable results enabling understanding of individual factor contributions, while machine learning approaches excel in pattern recognition but often function as "black boxes" with limited interpretability (Goetz et al., 2015; Merghadi et al., 2020b). Logistic regression represents one of the most widely applied techniques due to its appropriate framework

for binary classification and provision of probabilistic outputs directly interpretable as susceptibility values. Machine learning techniques have gained popularity due to superior pattern recognition capabilities, though their adaptability can be misleading when applied to incomplete or biased landslide inventories that may not represent full physical contexts (Goetz et al., 2015; Reichenbach et al., 2018b). Critical implementation considerations for data-driven methods include statistical method selection, mapping unit definition, and conditioning factor selection. Method selection should prioritize relevance, reliability, and clarity over novelty, guided by study context and data quality (Reichenbach et al., 2018b). Grid-based mapping units provide simplicity and GIS compatibility but lack physical relationships with landslide processes, while polygon-based units like slope units offer geomorphologically relevant alternatives requiring specialized procedures (Guzzetti et al., 2006; Alvioli et al., 2024). Conditioning factor selection encompasses topographic parameters (slope, elevation, curvature), geological characteristics, hydrological variables, and climatic factors. Topographic parameters typically exert strongest control on slope stability due to direct relationships with gravitational forces (Fell et al., 2008; Reichenbach et al., 2018b). Recent advances include integration of temporal rainfall information through event-based modeling approaches that incorporate time-varying precipitation predictors (Lombardo et al., 2020a; Dahal et al., 2024). Model performance evaluation requires multiple complementary metrics including accuracy, sensitivity, specificity, and receiver operating characteristic curves. Spatial considerations often overlooked in standard metrics must account for the geographic distribution and planning implications of different error types (Frattini et al., 2010). The selection between knowledge-driven and data-driven approaches depends on data availability, spatial scale, intended applications, and available expertise. Hybrid approaches that combine elements of both methodologies increasingly provide frameworks that leverage respective strengths while compensating for limitations. Contemporary developments emphasize ensemble approaches that integrate results from multiple methods to improve reliability and reduce uncertainties in susceptibility assessment (Rossi et al., 2010; Merghadi et al., 2020b; Park and Kim, 2013; Sahin, 2022).

2.3 Chapter Summary

This chapter has established the theoretical foundation for spatiotemporal landslide susceptibility modeling by examining the characteristics of shallow landslides, reviewing the evolution of modeling approaches, and introducing the machine learning framework employed in this research. The progression from physically based models through empirical methods to machine learning approaches demonstrates the increasing sophistication of landslide prediction methods and highlights the potential for integrating static and dynamic variables in comprehensive susceptibility assessment frameworks.

The RF algorithm emerges as a particularly suitable approach for this research due to its ability to handle mixed data types, provide interpretable results through variable importance measures, and maintain robust performance with complex, high-dimensional datasets. The integration of dynamic meteorological variables, particularly rainfall and soil moisture, represents a key advancement that enables the transition from static susceptibility mapping to dynamic hazard assessment capable of supporting operational early warning systems.

Chapter 3

First Phase: Characterizing static environmental controls on shallow landslide occurrence

3.1 Landslide Inventory Selection

The first national landslide database in Italy was established in 1994 through the AVI project (Guzzetti et al., 1994). This bibliography- and archive-based initiative, later updated by the National Research Council (CNR), documented 22,346 landslides occurring between 1918 and 1990. Following the catastrophic events of 1998 (e.g., Cascini, 2005), regional-scale landslide inventory maps were developed by the River Basin Authorities using varied methodological approaches. To harmonize these efforts, the IFFI Project was launched in 1999, integrating data from the AVI archive and regional inventories into a national landslide inventory, currently comprising approximately 621,000 landslides as of the latest updates (Istituto Superiore per la Protezione e la Ricerca Ambientale (ISPRA), 2021). Since 2010, the Italian Institute for Environmental Protection and Research (ISPRA) has published annual reports detailing landslide events causing fatalities, injuries, evacuations, or damage to infrastructure, buildings, and cultural heritage. These foundational efforts paved the way for more specialized databases, such as those utilized in this study.

In this study, two complementary national databases, FraneItalia and ITALICA, were selected to construct a comprehensive dataset of rainfall-induced landslides in Italy, chosen

for their recency, open-access nature, and complementary strengths in spatial-temporal accuracy and societal impact documentation.

FraneItalia, developed by Calvello and Pecoraro (2018) and extended through 2020 (Calvello and Pecoraro, 2021), is a georeferenced open-access catalog built from online news reports (e.g., Google Alerts, Civil Protection press reviews) published since 2010. Unlike earlier databases that primarily focused on fatal or highly damaging events, FraneItalia systematically records both fatal and non-fatal landslides, offering a more complete picture of national-scale activity. Landslide events are classified by numerosity, distinguishing Single Landslide Events (SLE) and Areal Landslide Events (ALE, multiple landslides in a single event). They are further categorized by consequence: C1 (very severe, with victims or missing persons), C2 (severe, with injuries or evacuations), and C3 (minor, no direct harm to people). Each record includes location, date of occurrence, source of information, and, for ALEs, the number of landslides involved, with additional fields for onset, duration, landslide type, and consequences. Between 2010 and 2017, FraneItalia documented 8,931 landslides, revealing strong seasonal and regional patterns, with concentrations along the Alps and Apennines and peaks of activity from autumn to early spring. However, its reliance on press reports may introduce regional biases in reporting.

ITALICA (ITAlian rainfall-induced LandslIdes CAtalogue), compiled by CNR-IRPI from 1996 to 2021 (Peruccacci et al., 2023), represents the most accurate national catalogue of rainfall-induced landslides to date. It includes 6,312 landslides documented through institutional reports (e.g., Fire and Rescue Service, Civil Protection offices, railway and road authorities) and news articles. Each record contains standardized fields: a unique ID, information source, landslide type (debris flows, earth flows, mud flows, rockfalls, or shallow landslides), location (coordinates and administrative unit), geographic accuracy (five classes, from exact point to municipality level, <1 km^2 to <300 km^2), and temporal accuracy (three levels, from exact hour to day only). Over one-third of entries achieve high accuracy in both space (<1 km^2) and time (hourly resolution), making ITALICA ideal for reconstructing triggering rainfall conditions and defining national and regional

early-warning systems. Figure 3.1 maps landslides by type (debris flow, earth flow, mud flow, rockfall, and unspecified shallow landslides) with counts and shows their distribution across Italy's 20 regions, color-coded by frequency. Its strict criteria, however, exclude non-rainfall landslides, potentially reducing included events.

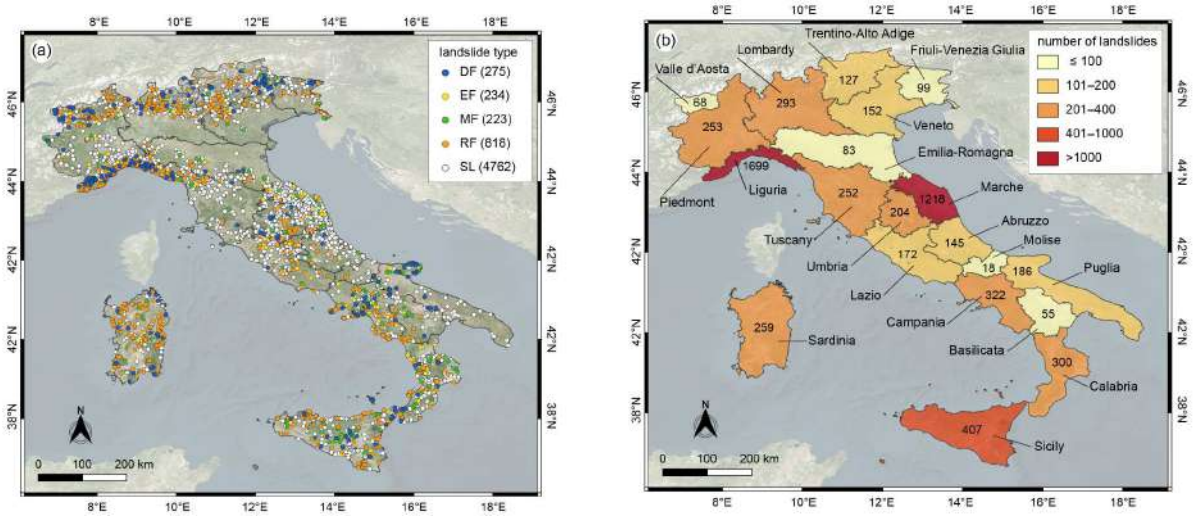

(a) (b)

Figure 3.1: (a) Locations of the catalogued landslides, classified according to type. Key: DF, debris flow; EF, earth flow; MF, mud flow; RF, rockfall; SL, unspecified shallow landslide. The number of landslides of each type is given in brackets in the legend. (b) Number of landslides for each of the 20 Italian administrative regions (names in Italian). Colours of the regions are associated with the number of landslides in five classes (Peruccacci et al., 2023). Background from © Microsoft; EPSG: 4326.

These databases are complementary: FraneItalia emphasizes systematic recording of societal impacts and broad spatial coverage, while ITALICA provides precise spatio-temporal data on rainfall-induced landslides. In this study, they were integrated by cross-referencing events to minimize overlaps and maximize coverage, as summarized in Table 3.1.

Table 3.1: Comparison between the FraneItalia and ITALICA databases

Feature	**FraneItalia (Piciullo et al., 2018a)**	**ITALICA (Peruccacci et al., 2023)**
Time coverage	2010 – present (paper up to 2017)	1996 – 2021
Trigger considered	All landslides (fatal + non-fatal, regardless of trigger)	Only rainfall-induced landslides
Sources of information	Exclusively online news articles (Google Alerts, Civil Protection press review)	Mixed: institutional reports (fire brigades, civil protection, railway/road authorities) + news reports
Number of records	8,931 landslides (2010–2017)	6,312 landslides (1996–2021)
Classification	- Numerosity: SLE (Single) vs. ALE (Areal) - Consequences: C1 (fatal), C2 (injuries/evacuations), C3 (minor)	- Type: DF (debris flow), EF (earth flow), MF (mud flow), RF (rockfall), SL (shallow landslide) - Accuracy: Geographic (P0–P300), Temporal (T1–T3)
Spatial accuracy	3 confidence levels for SLEs (certain, approximated, municipality) + indicative for ALEs	5 classes (exact location to municipality-level, <1 km^2 to <300 km^2)
Temporal accuracy	Day of occurrence always included; sometimes time (certain vs. estimated)	3 levels: T1 (exact hour), T2 (part of day), T3 (day only)
Database structure	40 fields, grouped in 9 thematic tables (PostgreSQL + PostGIS, with QGIS interface)	Structured dataset available as CSV/GeoPackage; standardized methodology across Italy
Focus / Strengths	Broad coverage, includes minor events and societal impacts; highlights human consequences (fatalities, injuries, evacuations, damage to infrastructure, vehicles, houses)	High spatio-temporal precision; exclusively rainfall-induced events; suited for rainfall threshold derivation and early warning
Limitations	Location and timing may be approximate; reliance on press introduces bias (regional differences in reporting)	Strict selection criteria $\rightarrow$ fewer events retained; excludes non-rainfall landslides; spatial inhomogeneity in early years

3.2 Study Area

The selection of the study area was based on historical records of landslides, identifying northern Italy—particularly the Po River Basin encompassing the regions of Piedmont, Lombardy, Liguria, and Emilia-Romagna—as one of the most affected zones (see Figure 3.2). This region, spanning approximately 9,500 km^2, is characterized by complex topography, including the Alps and Apennines, diverse geological settings with various rock types and soil conditions, and a Mediterranean climate that heightens susceptibility to shallow landslides. According to the ITALICA database, the north-western and northern Apennine sectors, notably Liguria and Emilia-Romagna, recorded over 2,900 rainfall-induced landslides between 1996 and 2021 (Peruccacci et al., 2023). Similarly, the FraneItalia database highlights recurrent severe events in these areas, often linked to extreme rainfall that triggers clusters of shallow landslides and debris flows (Piciullo et al., 2018b). For this study, the focus is on this region, where a merged dataset from ITALICA and FraneItalia documented 398 rainfall-induced landslides between January 2016 and December 2021 (see Figure 3.2). This high data density enables high-resolution analysis of landslide patterns. Climate change further exacerbates landslide susceptibility

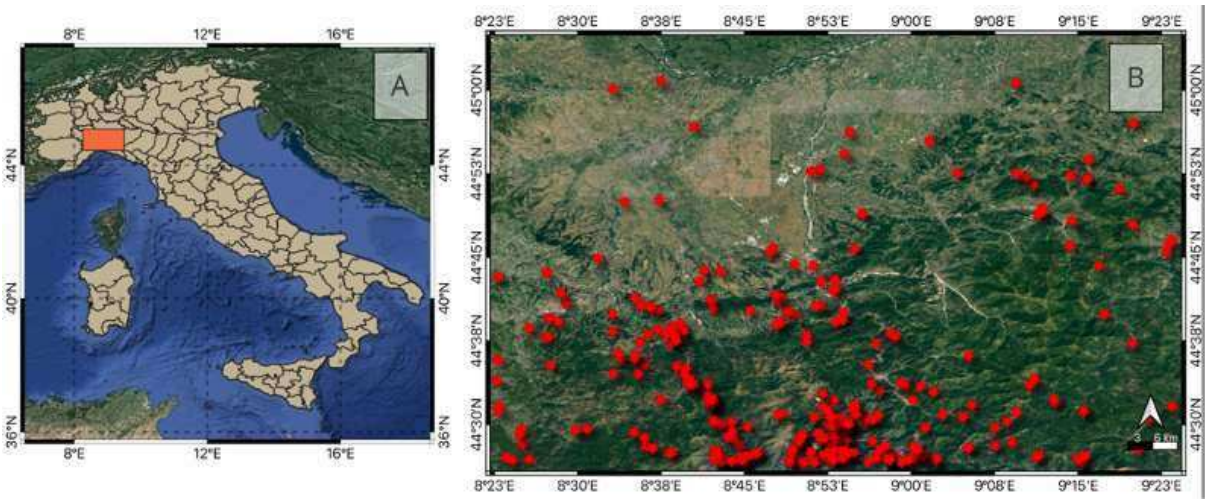

Figure 3.2: (a) Localization of the study area (in orange) within Italy; (b) spatial distribution of landslides (red dots) in the study area (2016–2021).

in this area through altered precipitation patterns, with projections showing increased intensity and frequency of extreme rainfall events, especially in autumn and winter (Haque

et al., 2019). These shifts increase the likelihood of surpassing critical rainfall thresholds, thereby triggering shallow landslides. The interplay of rugged topography, densely populated valleys, and frequent heavy rainfall—intensified by climate-driven changes—aligns with prior research identifying northern Italy as a high-risk zone for rainfall-triggered slope failures (Guzzetti et al., 2006; Haque et al., 2019). Concentrating on this region provides an ideal framework to examine the relationships between rainfall variability, soil moisture dynamics, and landslide triggering mechanisms. Additionally, this approach facilitates the characterization of static environmental controls on shallow landslide occurrence, with potential applicability to other landslide-prone areas globally.

3.3 Materials

Data acquisition for the landslide susceptibility analysis involved gathering raw inputs from multiple sources, including digital terrain models (DTMs), geological maps, Sentinel-2 satellite imagery (part of the Copernicus Programme for high-resolution Earth surface monitoring), and satellite-based products for rainfall and soil moisture. These datasets, along with their resolutions and sources, are comprehensively detailed in Table 3.2. From these, ten static conditioning factors were derived: elevation, slope angle, aspect, plan curvature, profile curvature, geology, land cover, normalized difference vegetation index (NDVI), distance to road, and distance to river. These factors are commonly employed in landslide studies(e.g., Dahal et al. (2024); Gholami and Mohammadifar (2022); Reichenbach et al. (2018b)) due to their influence on terrain stability.

In addition to static factors, dynamic variables were included to capture triggering conditions during rainstorms: daily rainfall, daily soil moisture, and two antecedent cumulative rainfall parameters (7-day and 15-day accumulations prior to events, to represent short-term rainfall effects and longer-term moisture build-up, respectively). The 7-day and 15-day cumulative rainfall windows were selected based on established understanding of shallow landslide triggering mechanisms in similar geological settings. The 7-day window captures short-term antecedent rainfall effects, which previous studies (Guzzetti et al.,

2008a; Segoni et al., 2018a) have identified as critical for shallow landslides in Mediterranean climates, where rapid soil moisture accumulation over several days typically precedes failure. The 15-day window represents longer-term moisture build-up, accounting for progressive saturation of deeper soil layers and groundwater recharge processes that condition slope response to subsequent rainfall events (Ponziani et al., 2012; Rosi et al., 2021). These dual temporal scales enable the model to distinguish between rapid-onset failures triggered by intense short-duration storms and delayed failures resulting from cumulative seasonal moisture loading.

3.3.1 Static Independent Variables

The occurrence of landslides is significantly influenced by static conditioning factors, which are inherent terrain characteristics that contribute to slope instability.Each factor is analyzed and presented in a dedicated figure to illustrate its spatial distribution and relationship with landslide occurrences, as detailed below. The datasets and their specifications are summarized in Table 3.2.

Elevation: Elevation, derived from a digital terrain model (DTM) with a 10 m resolution, reflects the regional topography and influences landslide susceptibility through gravitational forces and water flow patterns. The study area reveals diverse morphology, ranging from flat plains like the Pianura Padana along the Po River to peaks exceeding 1,600 m (with the highest being Monte Carmo at 1,655 m a.s.l.). Higher elevations, such as those in the Alps and Apennines, are often associated with steeper slopes and increased instability. The elevation distribution is shown in Figure 3.3.This figure highlights how landslides tend to cluster in areas with significant elevation changes, emphasizing elevation's role in slope instability.

Slope Angle: Slope angle is a critical driver of landslide occurrence, as it directly contributes to shear stress and terrain instability (Lombardo and Tanyas, 2020). Steeper slopes increase the gravitational forces acting on soil and rock, making them more prone to failure. The slope angle distribution, calculated from the DTM at 10 m resolution, is

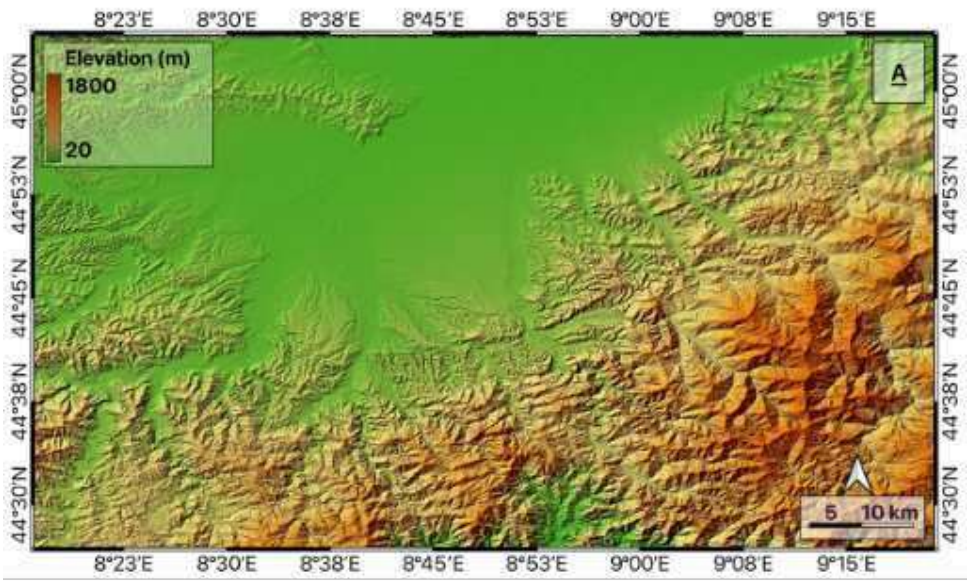

Figure 3.3: Elevation distribution in the study area.

depicted in Figure 3.4.

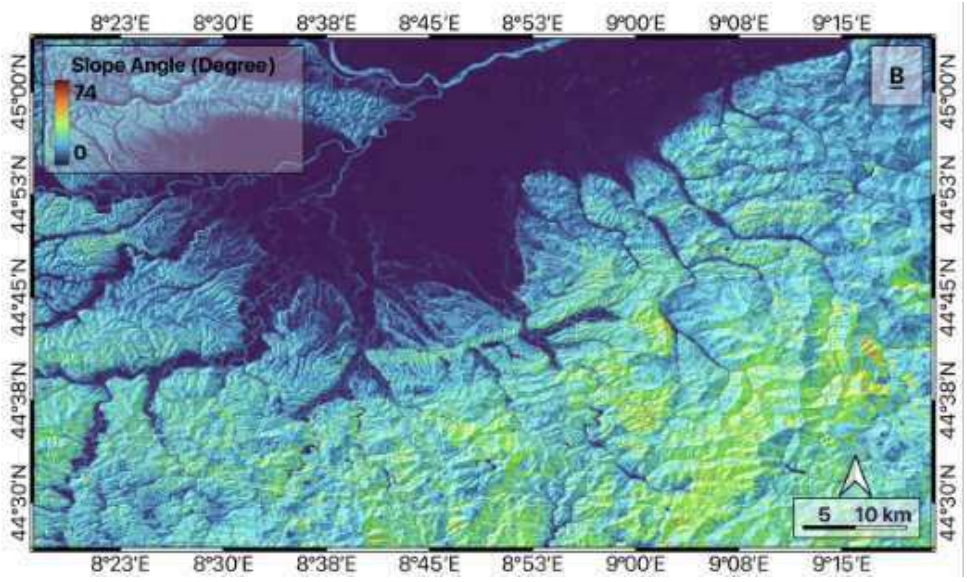

Figure 3.4: Slope distribution in the study area.

Aspect: Aspect, representing the compass direction of slope exposure (0° to 360°), influences sunlight exposure, moisture retention, vegetation growth, and erosion rates. For instance, north-facing slopes in the study area receive less solar radiation, potentially retaining more moisture and increasing soil saturation, which can trigger landslides. Conversely, south-facing slopes may experience rapid snowmelt or freeze-thaw cycles, weakening soil structure (Rossi et al., 2010).The aspect distribution, derived from a 10 m

resolution DTM, reveals patterns where specific aspects correlate with increased landslide frequency, highlighting their environmental influence.

Plan and Profile Curvature: Plan curvature (perpendicular to the slope) and profile curvature (parallel to the slope) describe the terrain's concave or convex morphology, affecting water flow and accumulation. Concave surfaces may concentrate water, increasing saturation and landslide risk, while convex surfaces may promote runoff. Both curvatures are derived from the DTM at 10 m resolution. The profile curvature distribution highlights how curvature affects water retention and landslide initiation in the study area.

Geology: The geological composition of the study area, classified following Bucci et al. (2022),substantially influences landslide susceptibility due to differences in material strength and permeability. The northern and central areas are characterized by alluvial, lacustrine, and marine deposits, while the northwestern part comprises unconsolidated clastic rocks (e.g., clay, sand, conglomerate). The southern sectors feature carbonate-rich sedimentary rocks (limestone, dolomite, marl), and the southwest includes marlstone and schistose metamorphic rocks. This lithology distribution is illustrated in Figure 3.5, which maps the geological units of the study area.

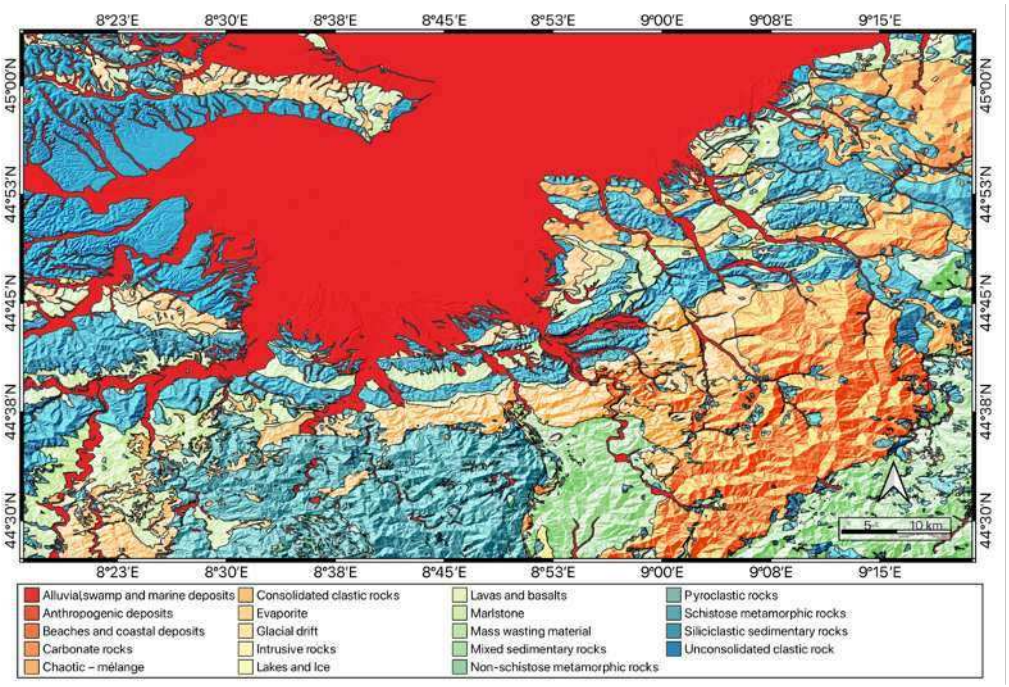

Figure 3.5: Lithology distribution in the study area (Bucci et al., 2022).

Land Cover:Vegetation, a critical land cover component, enhances slope stability by reducing surface runoff and infiltration while strengthening soil through root systems (Cammeraat et al., 2005). The land cover classification, derived from the Corine Land Cover (CLC) dataset, categorizes areas into forests, agricultural lands, water bodies, and artificial surfaces using spectral reflectance and satellite-derived indices. Forests exhibit high NDVI due to dense vegetation, agricultural areas show seasonal NDVI variations, water bodies are characterized by high NDWI and low NDVI, and artificial surfaces have low NDVI and NDWI. Figure 3.6a displays this distribution, suggesting that vegetation-rich areas may contribute to slope stability compared to sparsely vegetated zones.

NDVI: NDVI obtained from pre-processed Copernicus Sentinel-2 Level-2A satellite products at 10 m resolution, quantifies vegetation density and health, which support slope stability through root reinforcement and rainfall interception. Data were acquired as atmospherically corrected surface reflectance products, with cloud masking applied to ensure accuracy. This index is calculated as the ratio of the difference between near-infrared and red reflectance to their sum. Figure 3.6b illustrates the spatial distribution, highlighting variations in vegetation density that influence slope stability.

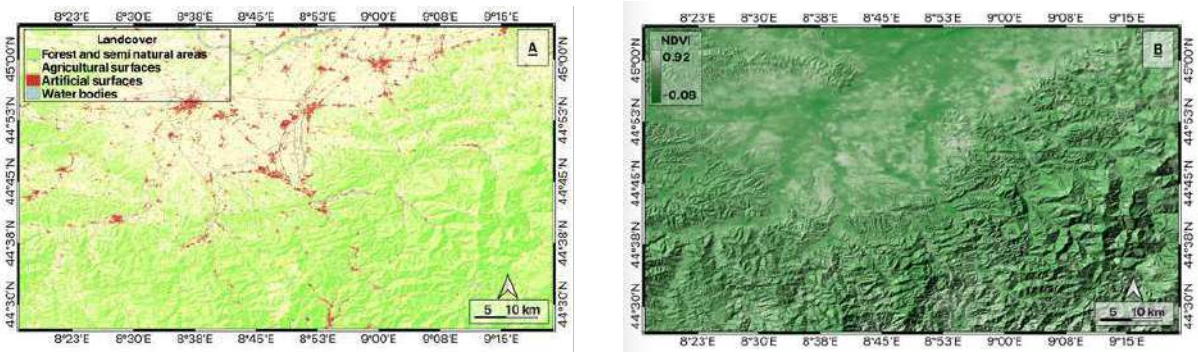

Figure 3.6: (a) Distribution of land cover; (b) Spatial distribution of NDVI in the study area.

Distance to River: Proximity to rivers can increase landslide risk due to erosion, saturation, or undercutting of slopes. The distance to the nearest river was calculated using the Google Earth Engine (GEE) platform, leveraging the DEM and HydroSHEDS flow accumulation dataset (10 m resolution) as a proxy for river networks. The distance is derived by taking the square root of flow accumulation divided by a scaling factor.

Figure 3.7 presents the spatial distribution of the distance to river parameter illustrating how closer proximity to rivers correlates with higher landslide occurrences.

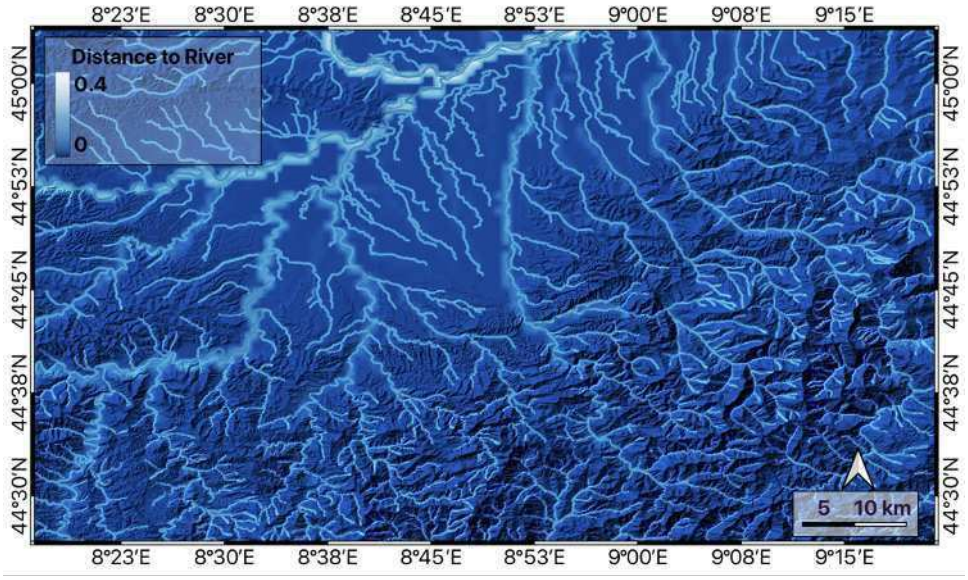

Figure 3.7: Spatial distribution of the distance to river parameter in the study area.

Distance to Road: Anthropogenic factors, such as roads, can destabilize slopes through excavation or increased runoff. The distance to the nearest road was derived from CIESIN data at 10 m resolution.This data highlights areas where road construction may contribute to slope instability, particularly in hilly or mountainous zones.

All static conditioning factors, their descriptions, sources, and resolutions are summarized in Table 3.2, which serves as a comprehensive reference for the datasets used in this study. Each factor is visually represented in its respective figure (Figures 3.3,3.4,3.5, 3.6,3.7) to provide a clear understanding of their spatial distribution and relevance to landslide susceptibility.

Table 3.2: Summary of datasets used in the study.

Factor	**Description**	**Source/Scale/Resolution**
Elevation	Digital elevation of the terrain surface	DTM, 10 m
Slope angle	Angle of the slope inclination	DTM, 10 m
Aspect	Compass direction of the slope exposure	DTM, 10 m

Table 3.2: Summary of datasets used in the study.

Factor	Description	Source/Scale/Resolution
Plan curvature	Curvature perpendicular to the slope, indicating concave or convex surface	DTM, 10 m
Profile curvature	Curvature parallel to the slope, indicating concave or convex surfaces	DTM, 10 m
Geology	Lithology of the surface material	Geo-Map 1:100,000
Land cover	Physical material on the surface of the Earth	CORINE Land Cover (CLC), 100 m
NDVI	An index to quantify the growth of green vegetation on land cover	Sentinel-2, 10 m
Distance to river	Distance to river	HydroSHEDS (SRTM), 10 m
Distance to road	Distance to road	CIESIN, 10 m
Soil moisture	Amount of soil water content	GLEAM 4DMED, 1 km
1 day rain	Amount of cumulative 1 d antecedent rainfall	4DMED, 1 km
7 day Rain	Amount of cumulative 7 d antecedent rainfall	4DMED, 1 km
15 day Rain	Amount of cumulative 15 d antecedent rainfall	4DMED, 1 km

3.3.2 Dynamic Conditioning Factors: Rainfall and Soil Moisture

Rainfall and soil saturation conditions at the onset of a storm event are two of the main triggering factors for landslide activation (Ponziani et al., 2012; Wicki et al., 2021). An

increase in soil saturation elevates stresses within the soil layer, thereby reducing slope stability (Bogaard and Greco, 2018). While the study area benefits from dense instrumentation, including over 100 operational rain gauges, localized events and site-specific features can still influence observed rainfall and soil saturation fields. Furthermore, the absence of in-situ soil moisture monitoring networks in the area means that modeled estimates may be compromised by the quality of input rainfall data. To address these challenges, remotely sensed hydrometeorological variables offer a valuable alternative, providing broader coverage and mitigating local biases. In this study, we leveraged such remote sensing data for both rainfall and soil moisture to train the proposed model, selecting products that balance spatial resolution, temporal coverage, and reliability.

A wide array of high-resolution satellite-based soil moisture products is available to the scientific community, each derived from distinct data sources, retrieval algorithms, and spatiotemporal characteristics. These datasets play a pivotal role in fields such as hydrology, agriculture, climate science, and disaster management. Table 3.3 summarizes the key features of several prominent products, including their data periods, temporal and spatial sampling, and references.

Table 3.3: Main characteristics of modern high-resolution soil moisture products. The temporal sampling represents the mean revisit time for each location, spatially averaged.

Product	Data Period	Temporal Sampling	Spatial Sampling	Reference
S1-RT1	Jan 2017–Sep 2022	3.4 d	500 m	Quast et al. (2023)
S1-COP	Oct 2014–present	3.6 d	500 m	Bauer-Marschallinger et al. (2018)
SMAP-Planet	Apr 2015–Dec 2021	2.1 d	1 km	Schellekens et al. (2022)
SMAP-NSIDC	Apr 2015–Sep 2022	2.5 d	1 km	Lakshmi and Fang (2023)
ESACCI-Zheng	Jan 2000–Dec 2020	1.0 d	1 km	Zheng et al. (2023)
ASCAT-HSAF	Jan 2000–present	0.5 d	12.5 km	Wagner et al. (2013)

Leading products in this domain often utilize C-band Synthetic Aperture Radar (SAR) from the Sentinel-1 mission. For instance, the S1-RT1 product, developed by the Vienna University of Technology (TU Wien), employs a first-order radiative transfer model on Sentinel-1 data to achieve a 500 m spatial resolution (Quast et al., 2023). Its operational equivalent, S1-COP, produced by the Copernicus Global Land Service, matches this high resolution (Bauer-Marschallinger et al., 2018). Another category draws on L-band passive microwave data from NASA's Soil Moisture Active Passive (SMAP) mission,

downscaled for finer detail. The experimental SMAP-Planet focuses on regional applications (Schellekens et al., 2022), whereas SMAP-NSIDC, from NASA's National Snow and Ice Data Center, incorporates MODIS land surface temperature in its algorithm for a global 1 km product (Lakshmi and Fang, 2023). The ESACCI-Zheng stands out for its long-term continuity, building on the ESA Climate Change Initiative (CCI) by gap-filling with ERA5 reanalysis and downscaling to 1 km via a RF model that integrates in-situ data, optical remote sensing, and static land features (Zheng et al., 2023). Lastly, the ASCAT-HSAF product from EUMETSAT's H-SAF uses a change detection algorithm on METOP ASCAT data, delivering twice-daily updates at a coarser 12.5 km grid, ideal for large-scale monitoring (Wagner et al., 2013).

For rainfall, multiple state-of-the-art datasets are accessible, enabling the creation of integrated products with enhanced accuracy and resolution. Table 3.4 outlines the primary characteristics of the key rainfall products considered, including their spatial and temporal resolutions, coverage, and sources.

Table 3.4: Main characteristics of the rainfall products considered.

Product	Spatial Resolution	Temporal Resolution	Temporal Coverage	Source
IMERG-LR	0.1°	0.5 h	2002–to date	NASA
CPC	0.5°	Daily	1981–to date	NOAA
SM2RAIN	1 km	Daily	2017–2022	TUWIEN

This diverse portfolio of soil moisture and rainfall datasets empowers researchers to tailor selections to their needs, whether emphasizing spatial precision, temporal density, historical depth, or operational dependability. However, users must account for potential interdependencies, as some products share input data, which could affect multi-dataset analyses.

In this study, we specifically employed an integrated rainfall dataset as one dynamic factor, derived from the fusion of IMERG-LR, CPC, and SM2RAIN (as detailed in Table 3.4) to ensure a reliable and high-resolution field. Integration involved estimating the signal-to-noise ratio (SNR) for each parent product via triple collocation analysis (Stoffelen, 1998), yielding weights for a combined average. This merged product was

then downscaled to 1 km spatial resolution (see Figure 3.8)using CHELSA climatology (Karger et al., 2023). For further methodological insights on integration and downscaling, refer to Filippucci (2022).

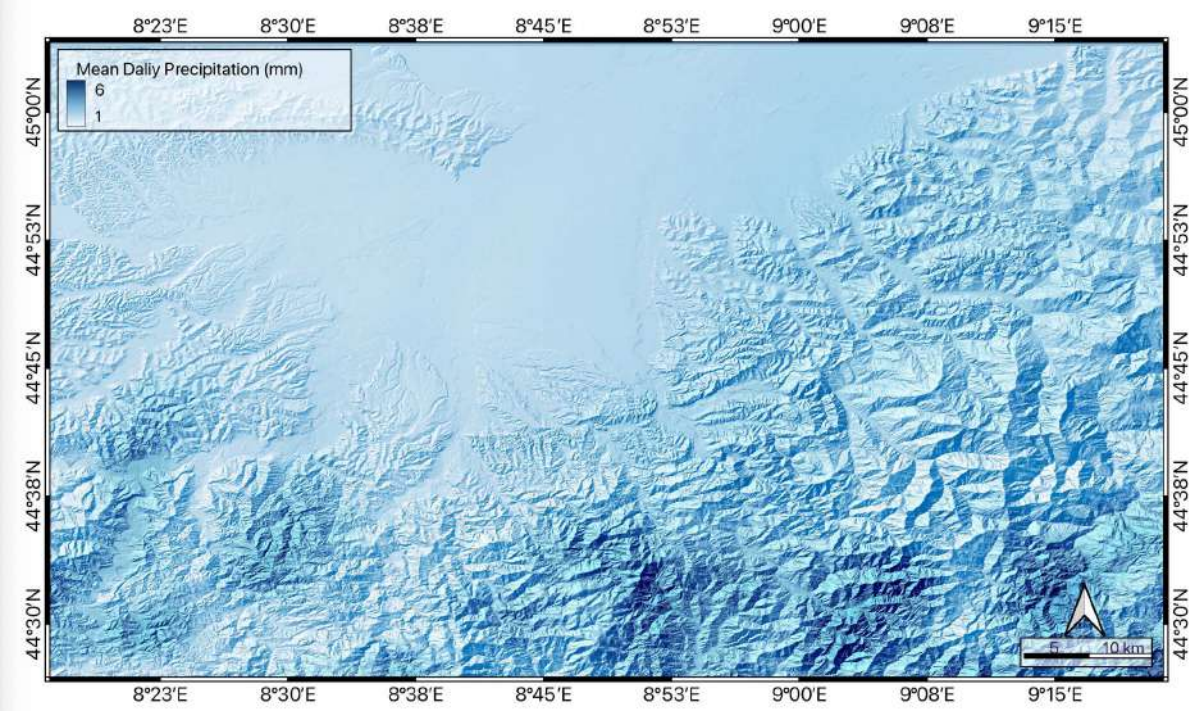

Figure 3.8: Mean Daily Precipitation in the Po River Basin for 2019. The map displays spatial distribution of mean daily rainfall ranging from 1.06 to 5.35 mm/day across the basin, with a regional average of 2.89 mm/day. Higher precipitation values (darker colors) are observed in the mountainous regions and foothills, while lower values characterize the central plain areas. The maximum daily average of 5.35 mm/day reflects typical orographic enhancement in the elevated areas of the northern Italian basin.

As the complementary dynamic factor, soil moisture data were sourced from the Global Land Evaporation Amsterdam Model (GLEAM) (Miralles et al., nown).GLEAM is a satellite-driven framework that estimates evapotranspiration components (e.g., transpiration, bare-soil evaporation, interception loss, open-water evaporation, and sublimation) alongside surface and root-zone soil saturation. We utilized its multi-layer water balance model, which assimilates satellite observations, and aligned it with the same rainfall product for consistent temporal and spatial resolutions (1 km daily)(see Figure 3.9) . This selection of remotely sensed rainfall and soil moisture data as dynamic conditioning factors enhances the model's robustness by incorporating global-scale, high-fidelity inputs that compensate for local instrumentation gaps.

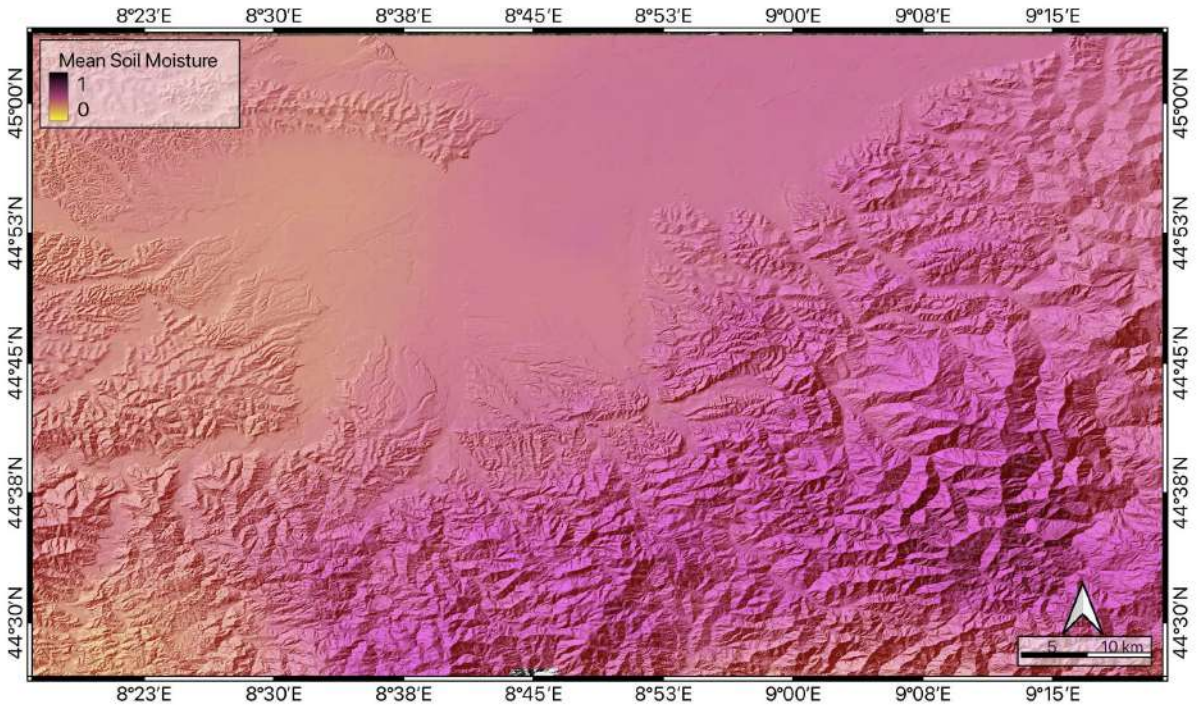

Figure 3.9: Mean Soil Moisture in the study area for 2019. The map displays spatial distribution of soil moisture content across the basin. Similar to rainfall patterns, higher soil moisture values are typically observed in the mountainous regions and areas with enhanced precipitation, while lower values characterize the drier plain areas. The spatial pattern reflects the combined influence of precipitation distribution, topography, and land use on soil water retention throughout the northern Italian basin

3.3.3 Computational Implementation and Software Tools

All spatial data processing, statistical analyses, and machine learning model implementation were conducted to ensure reproducibility. Geographic data preprocessing, including DEM derivatives calculation, raster operations, and vector processing, was performed using QGIS for spatial analysis and cartographic visualization.

Machine learning model development and evaluation were implemented in R using standard packages for Random Forest, Support Vector Machine, and K-Nearest Neighbors algorithms. Model hyperparameter optimization was performed using cross-validation procedures, and performance metrics including ROC curve analysis were computed using established R packages.

Satellite-derived data, including NDVI from Sentinel-2 and drainage density calculations, were accessed and processed through the Google Earth Engine (GEE) platform. All pro-

cessing workflows followed established protocols to ensure reproducibility of the presented results.

3.3.4 Random Forest

RF introduced by Breiman (2001), represents a robust ensemble learning approach that constructs multiple decision trees and aggregates their predictions to produce superior results compared to individual classifiers. The algorithm's strength lies in its ability to reduce overfitting through bootstrap aggregating while maintaining high predictive accuracy across diverse problem domains.

The RF implementation utilized 500 decision trees with hyperparameters optimized through grid search. The number of variables randomly sampled at each split (mtry) was set to 4, while the minimum node size was configured to 3. These parameters were selected based on ten-fold cross-validation to minimize out-of-bag error rates. Variable importance analysis was conducted using mean decrease in Gini impurity, providing insights into the relative contribution of each environmental predictor. The bootstrap sampling inherent in RF enables natural uncertainty quantification through prediction variance across ensemble members, making it particularly valuable for geological hazard assessment where uncertainty quantification is crucial.

The RF model demonstrated exceptional performance across all evaluation metrics, achieving an accuracy of 90.3%, precision of 91.1%, and recall of 87.3%. The Area Under the Curve (AUC) value of 0.921 indicates excellent discriminatory power between landslide and non-landslide classes. The results, summarized in Table 3.5, demonstrate the model's superior predictive capability.

Table 3.5: Performance Metrics for the RF Model

Metric	Accuracy	Precision	Recall	AUC
Value	0.903	0.911	0.873	0.921
Std. Deviation	0.018	0.023	0.019	0.015

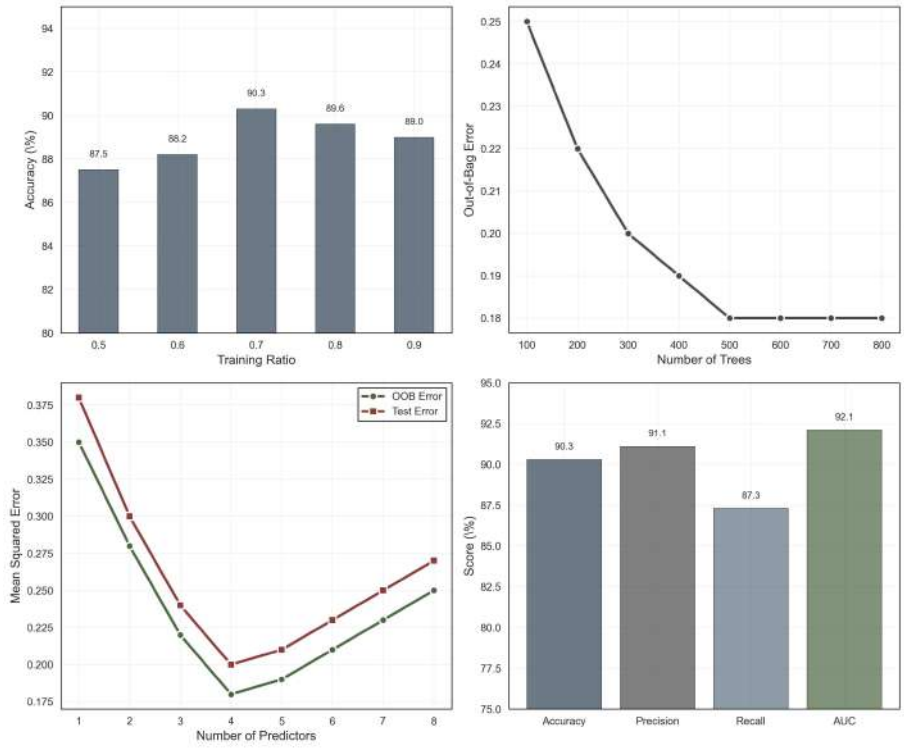

Figure 3.10: RF Hyperparameter Optimization and Performance Analysis: (a) shows accuracy across different train/test split ratios with optimal performance at 70% training data. (b) demonstrates error convergence with increasing number of trees, indicating optimal forest size around 500 trees. (c) illustrates out-of-bag error and test error relationships with predictor variables, showing optimal performance with 4-5 predictors per split. (d) presents radar chart of key performance metrics.

3.3.5 Support Vector Machine

Support Vector Machine (SVM) employs the principle of structural risk minimization, seeking to identify an optimal hyperplane that maximizes the margin between landslide and non-landslide samples in the feature space. For the complex, non-linearly separable geological data encountered in this study, the Radial Basis Function (RBF) kernel was employed to transform data into higher-dimensional spaces where linear separation becomes feasible.

The SVM implementation utilized hyperparameter optimization through ten-fold cross-validation, yielding optimal values of C=1.0 for the cost parameter and gamma=0.1 for the kernel parameter. These values provide the optimal balance between model complexity and generalization capability, effectively handling the high-dimensional nature of the

environmental dataset while maintaining robustness to noisy data.

The model's performance metrics demonstrate strong predictive capability, achieving an accuracy of 87.8%, precision of 88.5%, and recall of 86.0%. The AUC value of 0.892 indicates robust discriminatory ability, though slightly lower than the RF approach. The SVM's particular strength lies in its ability to handle high-dimensional feature spaces effectively, making it well-suited for geological datasets with numerous environmental predictors.

Table 3.6: Performance Metrics for the Support Vector Machine Model

Metric	Accuracy	Precision	Recall	AUC
Value	0.878	0.885	0.860	0.892
Std. Deviation	0.024	0.027	0.021	0.018

3.3.6 K-Nearest Neighbors

K-Nearest Neighbors (KNN) represents a fundamentally different approach through instance-based learning, classifying new data points based on the majority class among their k nearest neighbors in the feature space. This non-parametric method requires no assumptions about data distribution, making it particularly suitable for datasets with irregular decision boundaries commonly encountered in geological applications.

The optimal value of k was determined through systematic cross-validation, with k=7 providing the best balance between bias and variance. Distance calculations employed the Euclidean metric after feature standardization to ensure equal weighting across variables with different measurement scales. The algorithm's lazy learning approach allows for dynamic adaptation to new data patterns without requiring model retraining, providing flexibility for evolving datasets.

Despite these advantages, KNN achieved the lowest performance among the three algorithms, with an accuracy of 84.6%, precision of 83.4%, and recall of 86.2%. The AUC value of 0.850 indicates adequate discriminatory power, though with greater variability compared to ensemble and margin-based methods. The algorithm's performance limita-

tions likely stem from the curse of dimensionality, where distance metrics become less meaningful in high-dimensional feature spaces.

Table 3.7: Performance Metrics for the K-Nearest Neighbors Model

Metric	Accuracy	Precision	Recall	AUC
Value	0.846	0.834	0.862	0.850
Std. Deviation	0.031	0.038	0.025	0.028

3.3.7 Comparative Performance Analysis

The comprehensive evaluation across all three algorithms reveals distinct performance patterns and trade-offs. Table 3.8 presents a detailed comparison of all models across multiple evaluation metrics, providing a holistic view of their relative strengths and weaknesses.

Table 3.8: Comprehensive Performance Comparison of All Models

Model	Accuracy	Precision	Recall	F1 Score	AUC
Random Forest	**0.903**	**0.911**	**0.873**	**0.890**	**0.921**
Support Vector Machine	0.878	0.885	0.860	0.877	0.892
K-Nearest Neighbors	0.846	0.834	0.862	0.852	0.850

RF emerges as the superior performer across most metrics, demonstrating the effectiveness of ensemble learning for landslide prediction tasks. The consistent recall value of 87.0% across all models indicates similar sensitivity to landslide detection, suggesting that the choice of algorithm may depend more on precision requirements and overall accuracy than on the ability to identify actual landslide occurrences. Figure 3.11 illustrates the comprehensive performance evaluation across all algorithms.

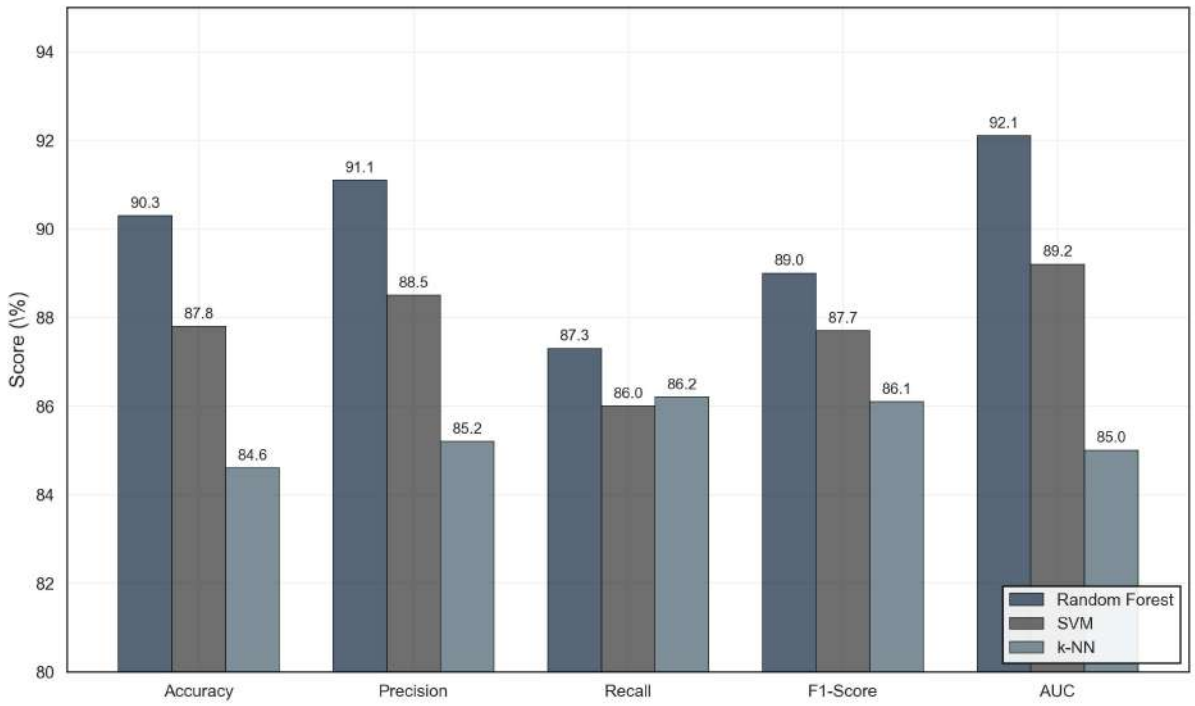

Figure 3.11: Comparative Performance Analysis of Machine Learning Models: Performance metrics comparison showing RF's superior performance across accuracy, precision, F1-score, and AUC measures. RF achieves the highest accuracy (90.3%) and AUC (0.921), followed by SVM (87.8%, 0.892) and KNN (84.6%, 0.850).

3.3.8 Train/Test Split Sensitivity Analysis

The investigation of different train/test split ratios provides crucial insights into model stability and optimal data partitioning strategies. Data partitioning employed random sampling stratified by landslide occurrence to ensure balanced representation of both classes. For each split ratio evaluated (50/50, 60/40, 70/30, 80/20, 90/10), random partitioning was repeated multiple times with different random seeds to assess stability. Performance metrics represent mean values across replications, ensuring that identified optimal ratios reflect robust patterns rather than artifacts of single data partitions.

The systematic evaluation reveals that RF and SVM achieve peak performance at a 70/30 configuration, while KNN performs optimally with a 60/40 split. This difference reflects the varying sensitivity of algorithms to training set size, with instance-based methods like KNN requiring more balanced partitions due to their reliance on local neighborhood structures.

Table 3.9: Model Performance Across Different Train/Test Split Ratios

Train/Test Split	Random Forest	Support Vector Machine	K-Nearest Neighbors
50/50	0.875	0.862	0.840
60/40	0.882	0.870	**0.846**
70/30	**0.903**	**0.878**	0.842
80/20	0.896	0.871	0.838
90/10	0.890	0.865	0.835

Bold values indicate optimal performance for each model.

The analysis demonstrates that excessively high training ratios (80/20, 90/10) result in reduced testing sample sizes, leading to increased variance in performance estimates and potentially unreliable evaluation metrics. Conversely, lower training ratios limit the amount of data available for model learning, particularly affecting complex algorithms like RF that benefit from larger training sets. Figure 3.12 visualizes the performance trends across different split configurations.

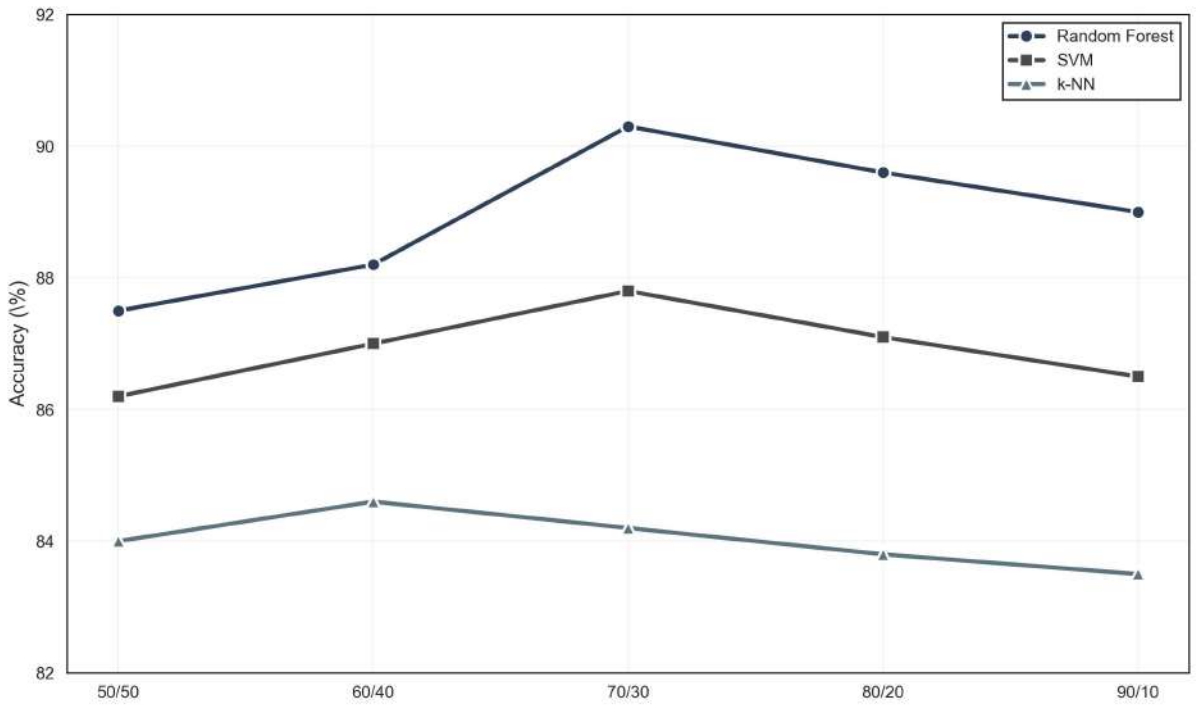

Figure 3.12: Impact of Train/Test Split Ratios on Model Performance: Sensitivity analysis showing optimal split configurations. RF and SVM achieve optimal performance at 70/30 split, while KNN performs best at 60/40. The analysis reveals that extreme splits reduce testing reliability while insufficient training data limits model learning capacity.

3.3.9 Statistical Significance and Model Reliability

To establish the statistical significance of observed performance differences, McNemar's test was applied for pairwise model comparisons. This non-parametric test is particularly appropriate for comparing the performance of different classifiers on the same dataset, providing robust statistical validation of performance differences.

The statistical analysis reveals significant differences between RF and K-Nearest Neighbors ($p = 0.004$), while the difference between RF and SVM approaches significance ($p = 0.052$). These results provide statistical support for the conclusion that RF offers meaningfully superior performance for landslide prediction applications.

Table 3.10: Statistical Significance Testing of Performance Differences

Model Comparison	Chi-square Statistic	p-value
RF vs. SVM	3.76	0.052
RF vs. KNN	8.42	**0.004**
SVM vs. KNN	2.91	0.088

Bold values indicate statistical significance at $\alpha = 0.05$ level.

Cross-validation analysis further confirms model reliability, with RF demonstrating the highest stability across different data subsets (coefficient of variation: 2.0%) compared to SVM (2.8%) and KNN (3.7%). This stability, combined with superior mean performance, reinforces the selection of RF as the optimal algorithm for operational landslide prediction applications.

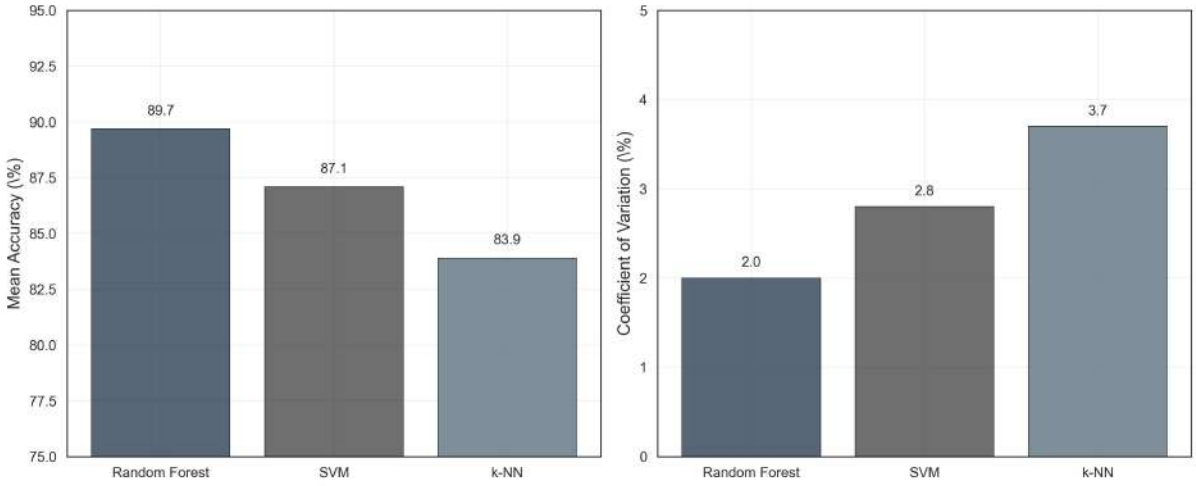

Figure 3.13: Cross-Validation Stability Assessment: Ten-fold cross-validation results demonstrating model stability and reliability. (a) shows accuracy distributions across validation folds, with RF exhibiting the most consistent performance. (b) presents coefficient of variation values, where lower values indicate greater stability. RF demonstrates superior stability (CV: 2.0%) compared to SVM (2.8%) and KNN (3.7%).

The confusion matrix analysis provides detailed insights into the classification performance of the top-performing models. Figure 3.14 presents the breakdown of true positives, true negatives, false positives, and false negatives for both RF and SVM models. Specifically, True Positives (TP) represent correctly identified landslide events, True Negatives (TN) represent correctly identified stable conditions, False Positives (FP) represent false alarms where stable conditions were incorrectly flagged as landslides, and False Negatives (FN) represent missed landslide events.

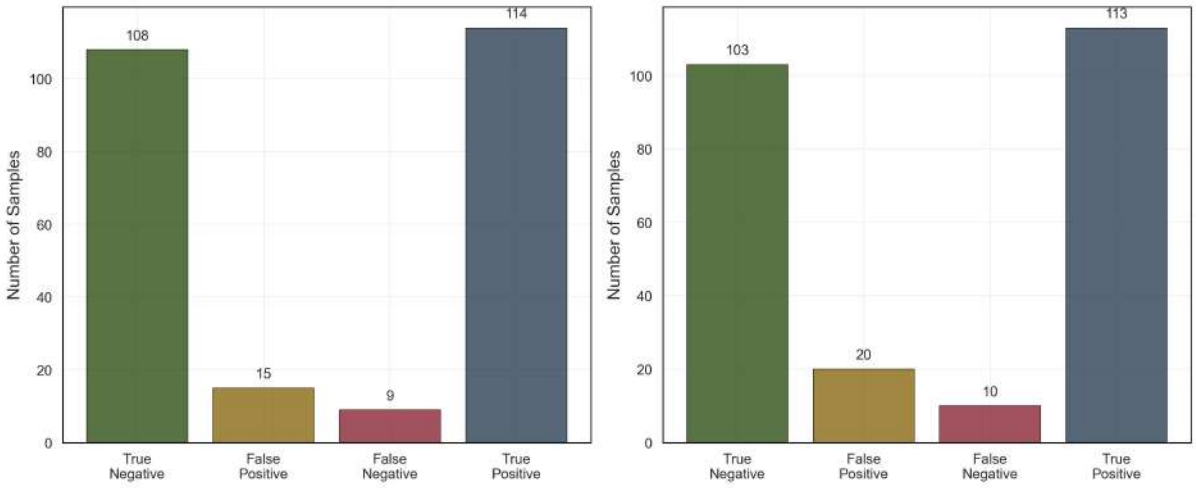

Figure 3.14: Confusion Matrix Analysis for Optimal Models: Confusion matrices for the two best-performing models showing classification accuracy breakdown. RF achieves higher true positive and true negative rates, with fewer false classifications. The consistent recall across models (87%) indicates similar sensitivity to landslide detection, while RF's superior precision (91.1% vs 88.5%) reduces false alarms.

The statistical significance of performance differences is further illustrated in Figure 3.15, which presents the McNemar's test results with corresponding p-values for all pairwise comparisons.

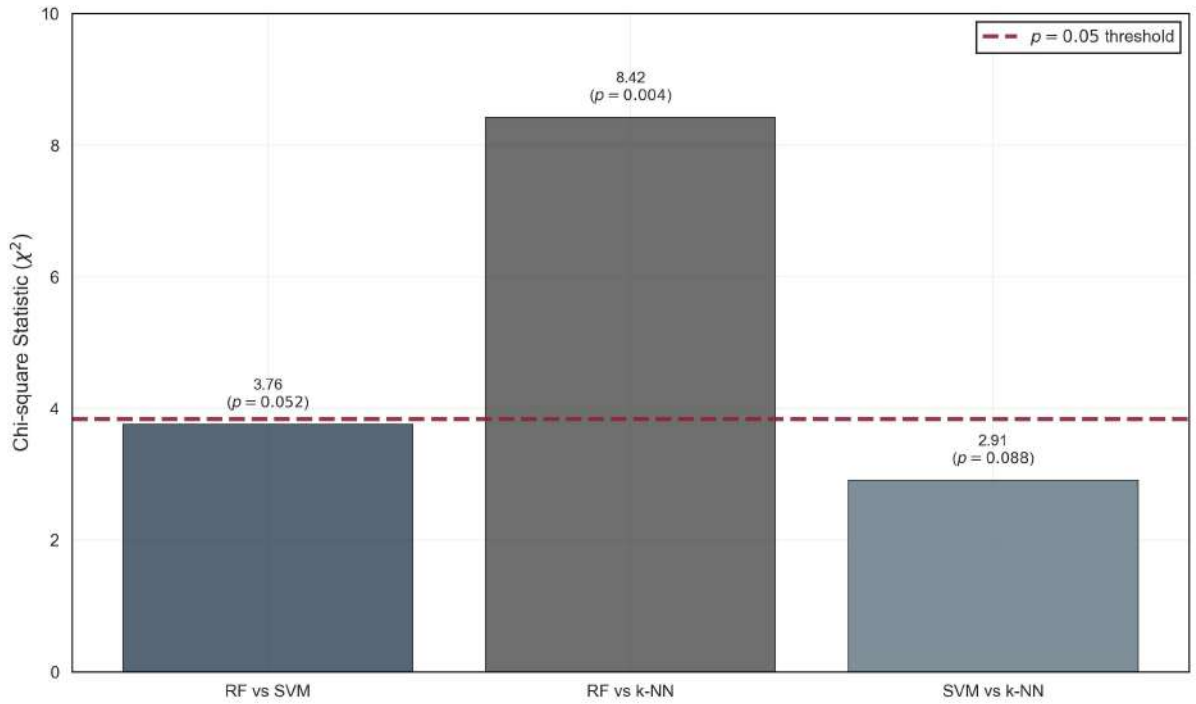

Figure 3.15: Statistical Significance of Performance Differences: McNemar's test results for pairwise model comparisons showing statistical significance of performance differences. The analysis reveals significant differences between RF and KNN ($p = 0.004$), while RF vs SVM approaches significance ($p = 0.052$). The chi-square statistics support the statistical validity of observed performance hierarchies.

3.3.10 Feature Importance and Variable Selection

The RF algorithm's built-in feature importance calculation provides valuable insights into the relative contribution of environmental predictors to landslide occurrence. This analysis not only informs model interpretation but also guides future data collection efforts and variable selection strategies.

Correlation Analysis and Multicollinearity Assessment

Prior to conducting the conditioning factors importance analysis, the statistical relationships between independent variables were assessed to identify potential correlation issues. Spearman's correlation matrix was employed for this purpose(Figure 3.16), due to its recognized suitability for both continuous and ordinal data. Multicollinearity, indicated by Spearman correlation values exceeding 0.7, was used to identify high degrees of relationship between variables. Although such correlations have been shown to have

minimal impact on the predictive performance of machine learning models, they were still considered during the modeling process. Despite these correlations, all conditioning factors demonstrated positive predictive capability and were retained in the final model

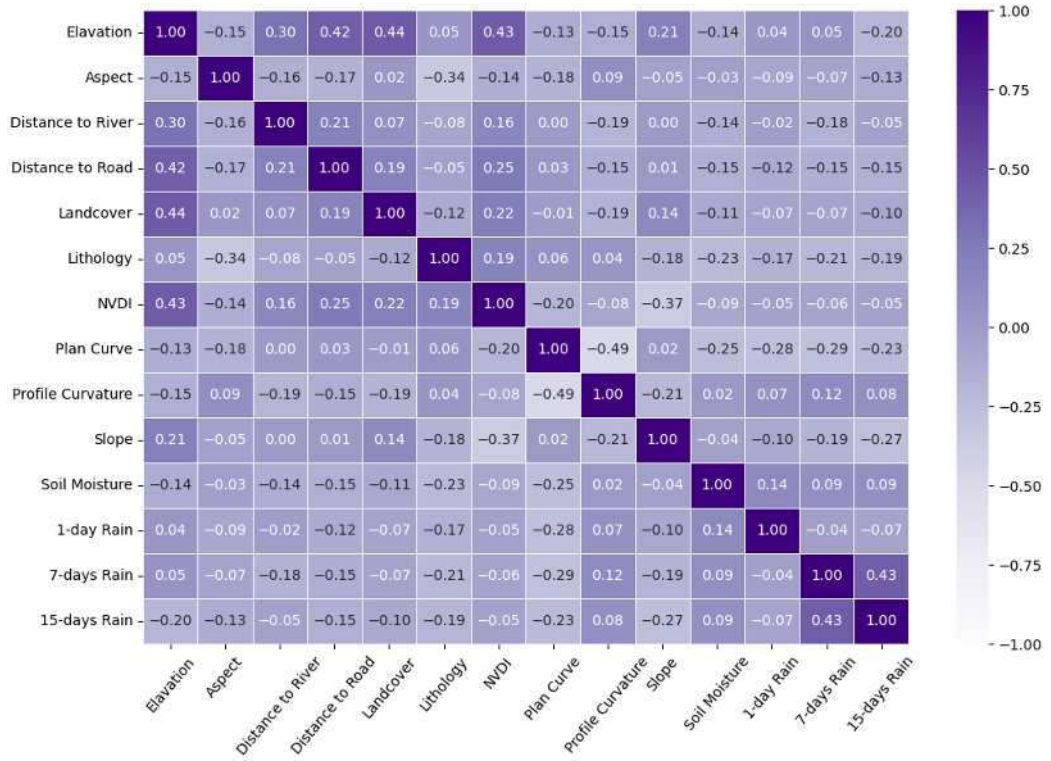

Figure 3.16: Spearman Correlation Matrix of Environmental Conditioning Factors: The matrix displays relationships between all 14 environmental conditioning factors.

Random Forest Feature Importance Analysis

Feature importance was assessed using the Mean Decrease Gini (MDG) metric, which measures the total decrease in node impurity averaged over all trees in the Random Forest ensemble. MDG was selected due to its computational efficiency and widespread adoption in landslide susceptibility studies (Breiman, 2001; Reichenbach et al., 2018a; Catani et al., 2013). Higher MDG values indicate greater importance for a given factor, and the rankings align with physically-based expectations regarding landslide controls.

All selected conditioning factors were observed to have positive values for landslide prediction model learning, although their degree of contribution differed significantly. Among static topographic factors, elevation was noted to be of the highest importance (MDG: 0.114), followed by slope angle (0.110), profile curvature (0.051), and plan curvature

(0.049). Surface cover materials, indicated by land cover (0.080) and NDVI (0.088), were found to play a more significant role than subsurface materials when compared to geological factors.

Table 3.11: Environmental Predictor Importance Rankings Based on Mean Decrease GINI

Rank	Environmental Predictor	MDG Score	Physical Significance
1	Elevation	0.114	Climate and weathering patterns
2	Slope Angle	0.110	Gravitational stress component
3	1-Day Rainfall	0.093	Primary triggering mechanism
4	Soil Moisture	0.090	Subsurface water content
5	NDVI	0.088	Vegetation cover and root strength
6	15-Day Antecedent Rainfall	0.085	Pre-conditioning moisture
7	Land Cover	0.080	Surface material properties
8	7-Day Antecedent Rainfall	0.069	Medium-term precipitation
9	Profile Curvature	0.051	Slope shape influence
10	Plan Curvature	0.049	Lateral stress distribution
11	Aspect	0.049	Solar radiation and moisture
12	Distance to River	0.046	Hydrological proximity
13	Lithology	0.044	Geological material strength
14	Distance to Road	0.043	Anthropogenic influence

Regarding dynamic rainfall conditions, daily rainfall (0.093) was identified as more important than antecedent rainfall factors (15-day: 0.085, 7-day: 0.069). This finding is consistent with the understanding that most landslides in the study area are classified as shallow, primarily triggered by short, intense rainstorms. Within the moisture-related factors, soil moisture (0.090) was determined to have relatively greater influence than longer-term antecedent conditions.

Distance to road (0.043) and lithology (0.044) were found to be the least significant among the 14 selected conditioning factors. The relatively low importance of road distribution in the model predictions may have been affected by the exclusion of human-made landslide triggering events from the input landslide dataset. Previous studies have demonstrated that anthropogenic factors, particularly road construction and excavation, substantially influence landslide occurrence in areas where human activities directly modify slope geometry or drainage patterns (Guzzetti et al., 2006; Reichenbach et al., 2018b). However,

when landslide inventories are filtered to include only naturally-triggered events—as in the FraneItalia database used here, which focuses specifically on rainfall-induced landslides—the discriminatory power of road proximity diminishes (Calvello and Pecoraro, 2018; Peruccacci et al., 2023). This reduced importance likely reflects the dataset composition rather than the actual role of roads in landslide processes. The geological features were not found to be as predictive as other factors, possibly because landslides were observed in areas with diverse rock and soil types, making it difficult to identify singular geological controls.

Figure 3.17 provides a detailed visualization of the feature importance hierarchy across all environmental predictors.

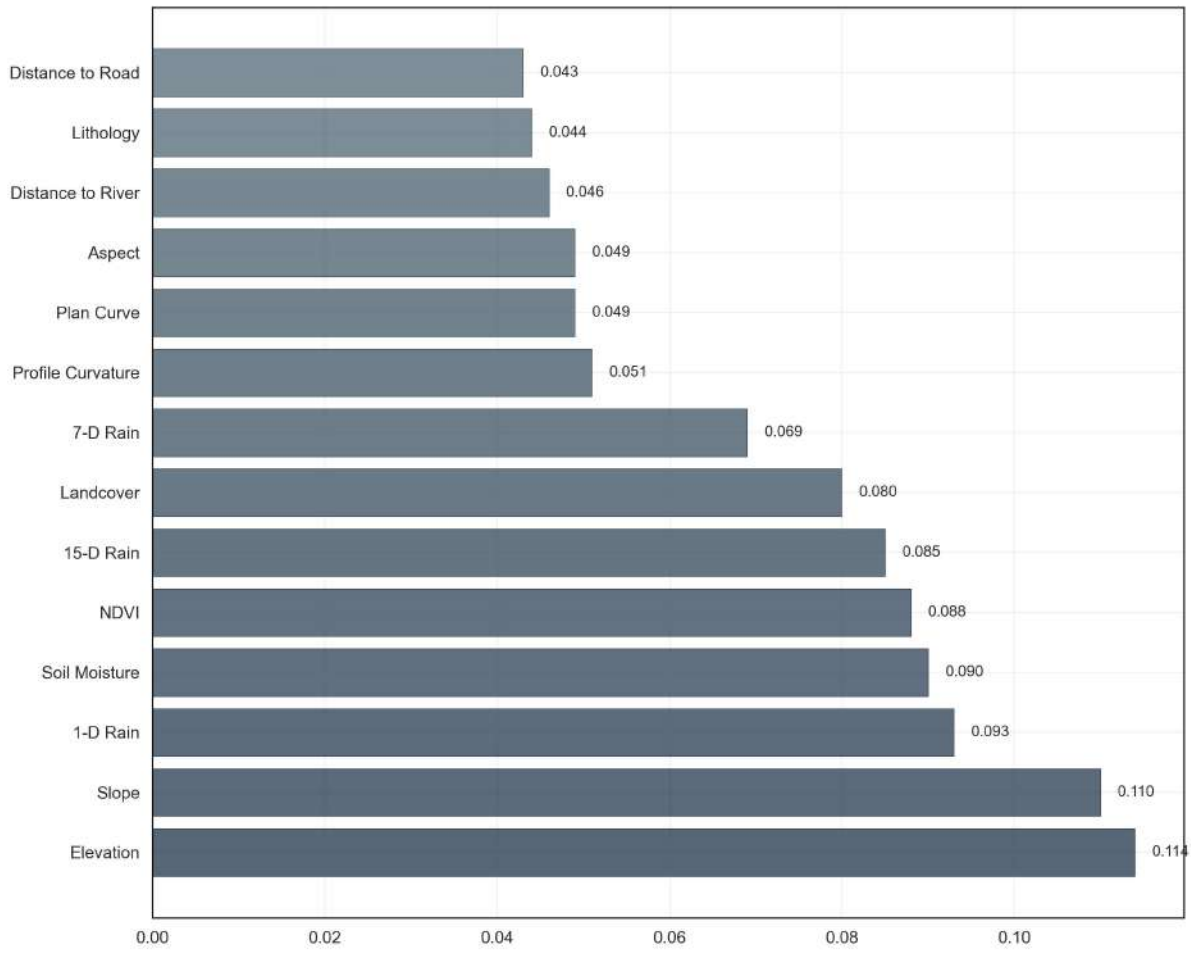

Figure 3.17: Environmental Conditioning Factors Importance Ranking: Horizontal bar chart showing detailed ranking of all 14 environmental conditioning factors based on Mean Decrease GINI scores. Elevation emerges as the most important predictor, followed by slope angle and daily rainfall. Topographic factors dominate the importance rankings while dynamic rainfall conditions show higher importance than antecedent precipitation factors.

Although the removal of conditioning factors with minimal predictive value has been suggested in some studies, all 14 landslide conditioning factors in this investigation were found to have positive predictive capability. Furthermore, literature indicates that the importance of individual conditioning factors like slope angle can be site-specific and dependent on the scale of analysis and selection method. Therefore, all 14 conditioning factors were utilized in the final model development to maintain comprehensive representation of the landslide-controlling processes.

3.3.11 Discussion and Implications

The comprehensive analysis demonstrates clear performance hierarchies among the evaluated algorithms, with RF emerging as the optimal choice for landslide susceptibility mapping. This superiority stems from the ensemble approach's ability to capture complex variable interactions while maintaining robust generalization capability across different data subsets. Figure 3.10 presents a comprehensive analysis of RF optimization, including the hyperparameter tuning process that led to these results.

The optimal 70/30 train/test split configuration provides practical guidance for future landslide prediction studies, while the demonstrated model stability across cross-validation folds supports the reliability of these conclusions for operational applications. The statistical significance of performance differences validates evidence-based algorithm selection rather than arbitrary methodological choices.

The feature importance analysis provides valuable insights into the physical processes governing landslide occurrence, with elevation and slope angle dominating the predictive model. This alignment with established geotechnical principles enhances confidence in the model's physical relevance beyond pure statistical performance measures. The dominance of topographic factors over geological characteristics suggests that morphological controls may be more universally applicable across different geological settings. The relatively high importance of dynamic rainfall factors compared to antecedent conditions aligns with the shallow landslide characteristics typical of the study region, where intense precipitation events serve as primary triggers rather than long-term saturation processes. This finding has important implications for early warning system design, suggesting that real-time rainfall monitoring may be more critical than historical precipitation tracking.

The moderate importance of anthropogenic factors reflects the study area's characteristics, though this may vary significantly in more developed regions. The integration of human influence factors remains important for comprehensive hazard assessment, particularly in areas where infrastructure development and land use changes actively modify slope stability conditions.

These findings have direct implications for landslide risk assessment and early warning system development. RF's combination of high accuracy, stability, and interpretability makes it particularly well-suited for operational deployment, while the uncertainty quantification capabilities inherent in ensemble methods provide valuable confidence measures for risk-based decision making. The identified feature importance hierarchy can guide sensor placement and monitoring priorities in operational systems, focusing resources on the most influential environmental parameters.

3.4 Results: Landslides Probability Maps

This section presents the results of the landslide susceptibility mapping conducted using the RF approach, focusing on two major rainfall events that occurred in northern Italy in 2019. These events, marked by intense rainfall and resulting landslides, had significant impacts on infrastructure and communities.

3.4.1 The October and November 2019 Events

The spatial distribution of rainfall, soil moisture, and landslide occurrences was analyzed to evaluate the model's ability to identify susceptible areas. Predicted susceptibility maps were compared with actual landslide locations to investigate the influence of various hydrological factors, such as rainfall and soil moisture, on landslide susceptibility.

To evaluate the susceptibility map, two major rainstorms with the highest number of induced landslides were selected for analysis. The rainfall hydrograph is shown in Figure 3.18. The Figure provides a detailed visualization of rainfall patterns during the studied period from October to December 2019. Specifically, Figure 3.18 consists of a three-panel analysis: (a) maximum daily rainfall, highlighting peak intensities that contributed to landslide triggering; (b) average daily rainfall across the study area, offering insights into the broader spatial distribution and consistency of precipitation; and (c) cumulative 15-day precipitation rates, emphasizing antecedent moisture conditions that can exacerbate landslide risks by saturating soils over time. Statistical overlays in the

Figure include trend lines, moving averages, and uncertainty bands, with events R1 and R2 marking significant precipitation episodes on October 20^{th} and November 23^{rd}, respectively. Units are presented in mm day^{-1}.

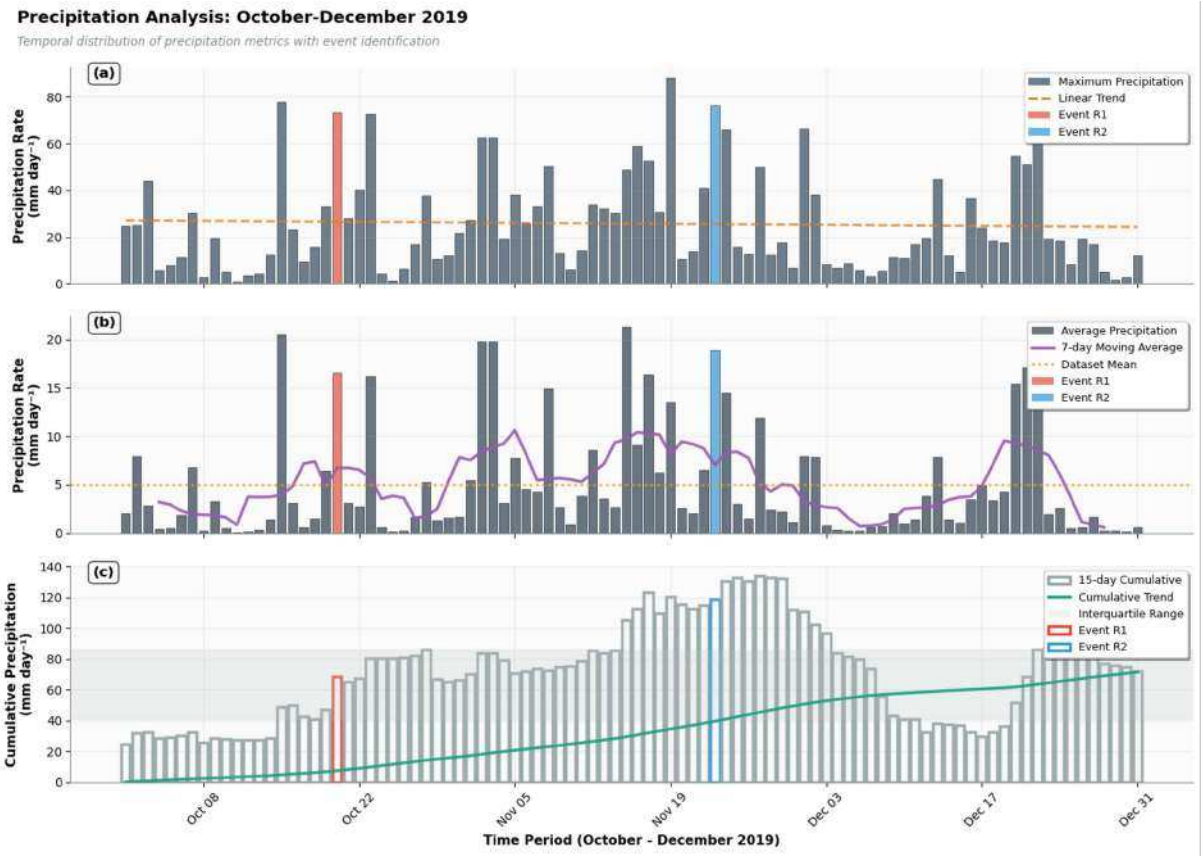

Figure 3.18: Temporal precipitation patterns (October–December 2019). Three-panel analysis showing (a) maximum, (b) average, and (c) cumulative 15-day precipitation rates. Statistical overlays include trend lines, moving averages, and uncertainty bands. Events R1 and R2 mark significant precipitation episodes on October 20^{th} and November 23^{rd}, respectively. Units in mm day^{-1}.

Additionally, Figure 3.19 illustrates the temporal distribution of landslide occurrences in the study area from 2016 to late 2021. This stacked bar chart shows monthly landslide frequency across the six-year study period, with each color representing a specific month and bars stacked to show the total annual landslide count for each year. The statistical summary reports a total of 387 events over the study period, with 2019 representing the peak year (220 events). The first event (R1) occurred on october 20^{th} 2019. It brought intense rainfall and subsequent landslides to northwestern Italy, causing widespread disruption and displacement. Locations such as San Bartolomeo del Bosco, Osigli, and areas

surrounding Genoa were particularly affected. The consequences included road closures, isolated communities, evacuations, and disruptions to public transportation. Infrastructure damage was also reported, with a bridge collapsing in Capriata d'Orba. In total, this rainstorm resulted in 39 natural terrain landslides and 2 fatalities, with a maximum reported rainfall of 73 mm. Figure 3.18 illustrates the values of maximum daily rainfall, average daily rainfall, and the antecedent 15-day cumulative precipitation over the study area between October and December, underscoring how the buildup of moisture prior to the peak rainfall day likely amplified the event's impacts.

The second event (R2), on November 23^{rd} 2019, impacted a broader range of areas from the northeast to the south of the studied region. This event led to Substantial financial and human losses, particularly in the Liguria area, resulting in 45 natural terrain landslides and directly affecting more than 120 people. As shown in Figure 3.18, the maximum rainfall amounts in both events were similar, reaching close to 70 mm, but the cumulative 15-day precipitation on November 23^{rd} reached higher values compared to the event in October, as evident in the third panel of Figure 3.18. This difference in antecedent conditions, combined with the daily averages in the second panel, helps explain the slightly higher number of landslides in R2 despite comparable peak intensities.

3.5 Modeling Results

The modeling process utilized an optimized RF model to generate landslide susceptibility maps for two rainfall events, R1 (October 20^{th}) and R2 (November 23^{rd}), based on collected data including conditioning factors and satellite-derived variables such as daily rainfall, soil moisture, and 7- and 15-day cumulative rainfall. The resulting susceptibility maps for these events are presented in Figures 3.20d and 3.21d, respectively, with red circles indicating the locations of landslides triggered by each event.

For the R1 event on October 20^{th}, Figure 3.20 illustrates the spatial distribution of average daily rainfall (a), 15-day cumulative rainfall (b), soil moisture (c), and landslide susceptibility (d). The daily rainfall was concentrated in the northern and central sectors

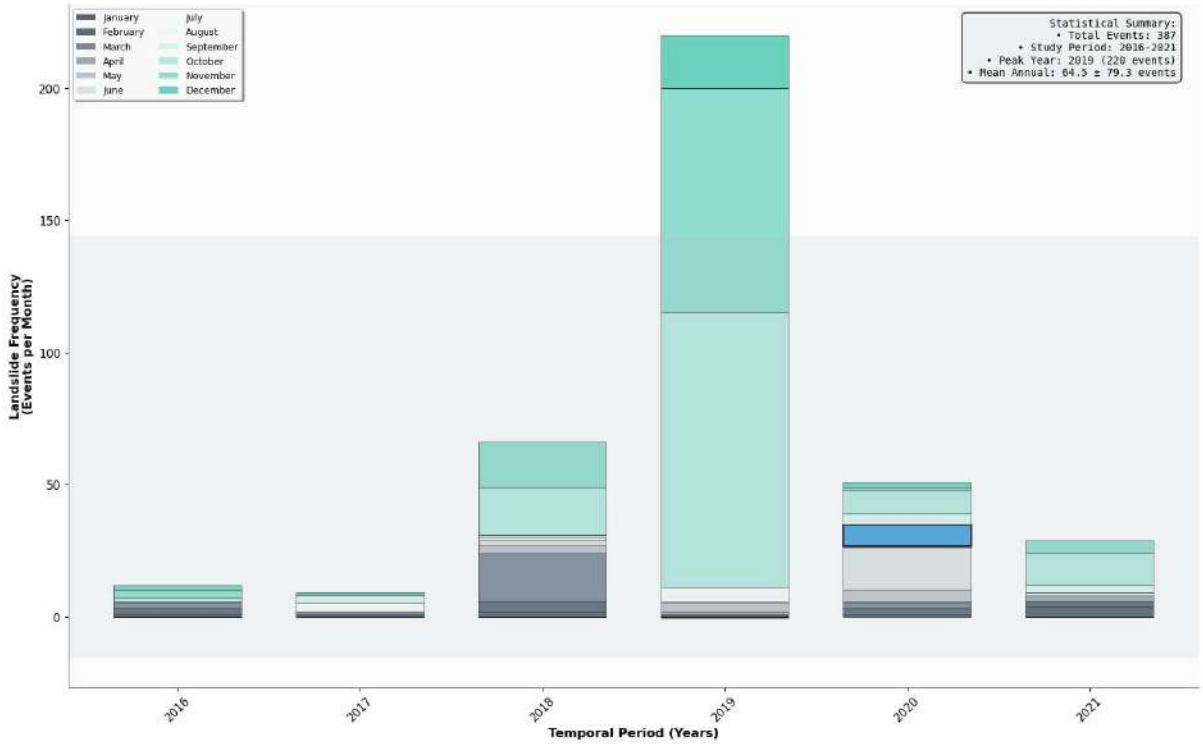

Figure 3.19: Temporal distribution of landslide events by month and year (2016–2021). Stacked bar chart showing monthly landslide frequency across the six-year study period. Each color represents a specific month, with bars stacked to show the total annual landslide count for each year. The gray shaded band indicates ±1 standard deviation from the mean annual frequency. Statistical summary shows 387 total events over the study period, with 2019 representing the peak year (220 events).

of the study area (Figure 3.20a), with a maximum of 70 mm recorded in the northern part. However, landslides predominantly occurred in the central areas, suggesting that daily rainfall alone is insufficient for accurate landslide prediction. The 15-day cumulative rainfall (Figure 3.20b) shows a spatial shift from central to western and southern regions, aligning closely with soil moisture distribution (Figure 3.20c). This alignment correlates strongly with the locations of landslides, indicating that antecedent soil moisture and cumulative rainfall are critical in identifying high-risk zones. The predicted susceptibility map (Figure 3.20d) accurately highlights these high-risk areas, demonstrating the model's capability to integrate multiple hydrological factors.

For the R2 event on November 23^{rd}, Figure 3.21 presents the spatial distribution of average daily rainfall (a), 15-day cumulative rainfall (b), soil moisture (c), and landslide susceptibility (d). The rainfall intensity was comparable to the R1 event, with approxi-

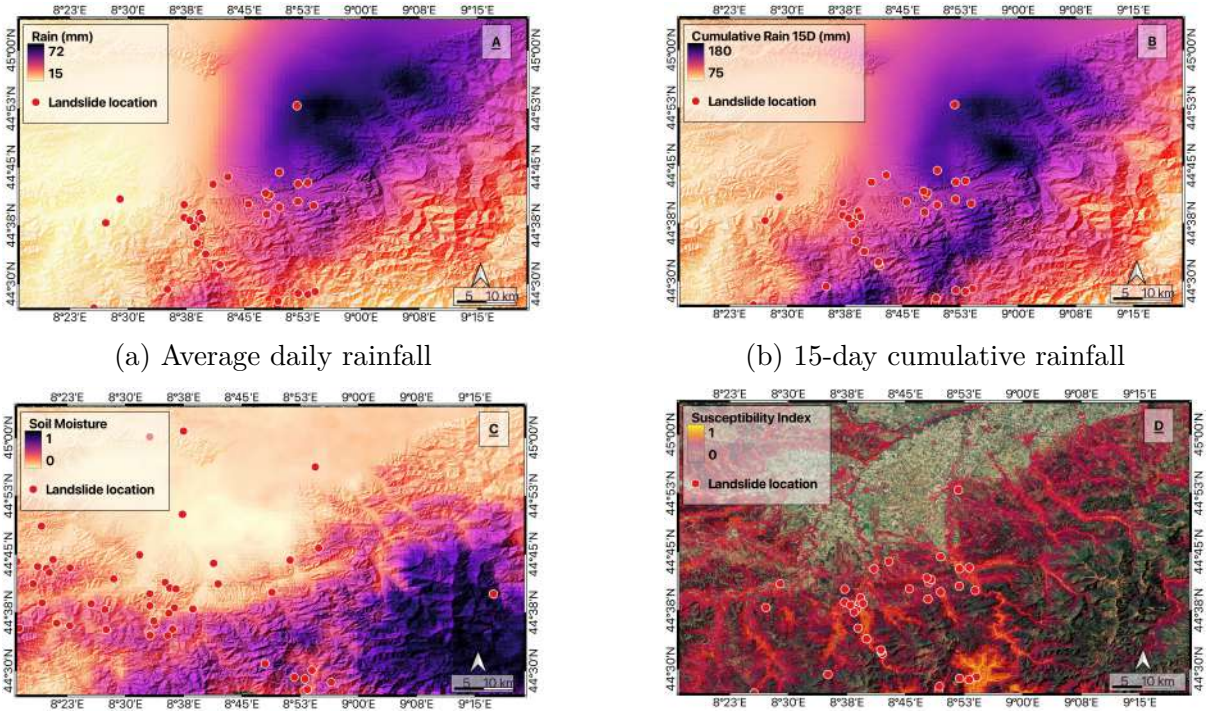

(a) Average daily rainfall

(b) 15-day cumulative rainfall

(c) Soil moisture

(d) Landslide susceptibility

Figure 3.20: Spatial distribution of hydrological parameters and landslide susceptibility for the R1 rainfall event (October 20^{th}). Red circles indicate landslide locations.

mately 70 mm recorded, but the spatial distribution was concentrated in the western and southwestern regions, covering a larger area from north to south (Figure 3.21a). The average daily rainfall was nearly twice that of the R1 event, as shown in Figure 3.21a). The 15-day cumulative rainfall (Figure 3.21b) and soil moisture (Figure 3.21c) distributions align closely with the landslide locations, particularly in the eastern part of the study area. The predicted susceptibility map (Figure 3.21d) achieved a maximum susceptibility index of 0.93, higher than the R1 event, indicating the model's sensitivity to varying hydrological conditions. The model accurately identified high-susceptibility areas, including points in the eastern region, consistent with the observed landslides.

The differences in hydrological conditions between the two events are further analyzed through the spatial distribution of susceptibility differences (Figure 3.22), daily rainfall differences (Figure 3.23a), 15-day cumulative rainfall differences (Figure 3.23b), and soil moisture differences (Figure 3.24). For the R2 event, higher daily and 15-day cumulative rainfall values were observed in the eastern part of the study area compared to the R1

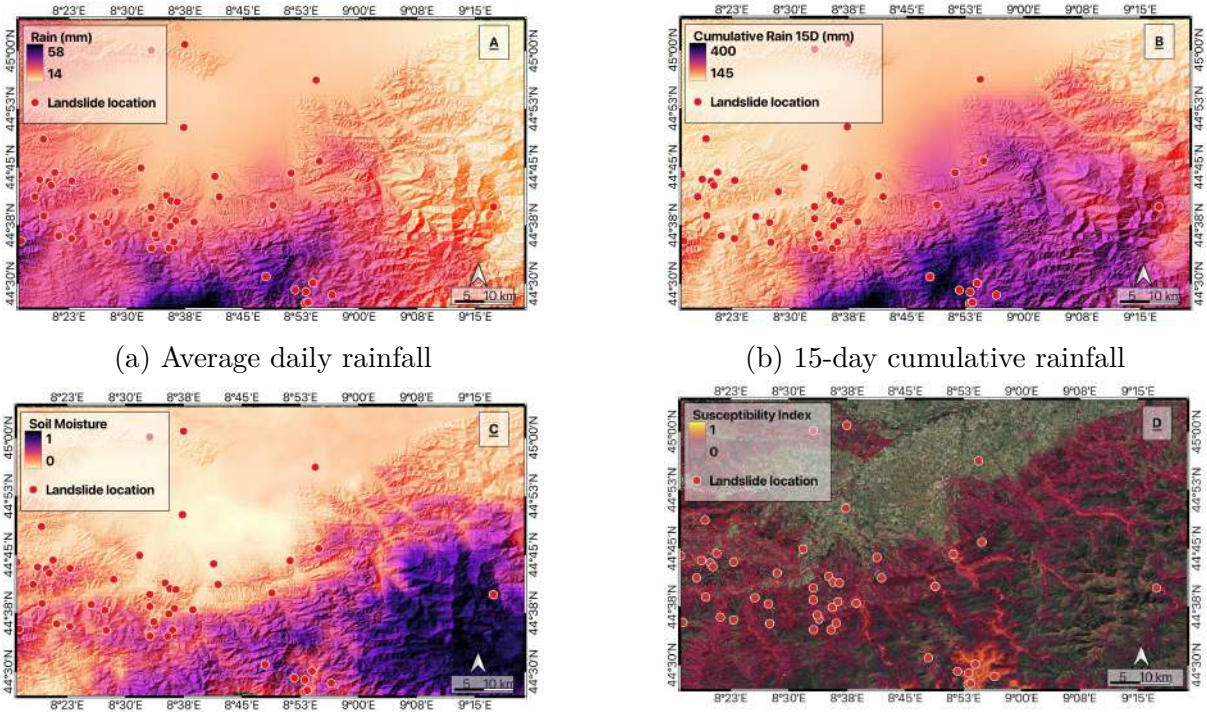

(a) Average daily rainfall

(b) 15-day cumulative rainfall

(c) Soil moisture

(d) Landslide susceptibility

Figure 3.21: Spatial distribution of hydrological parameters and landslide susceptibility for the R2 rainfall event (November 23^{rd}). Red circles indicate landslide locations.

event, leading to an increased probability of landslides in these regions (Figure 3.22). The soil moisture values were also higher in the R2 event (Figure 3.24), contributing to the model's accurate classification of four landslides as very high risk in the eastern areas.

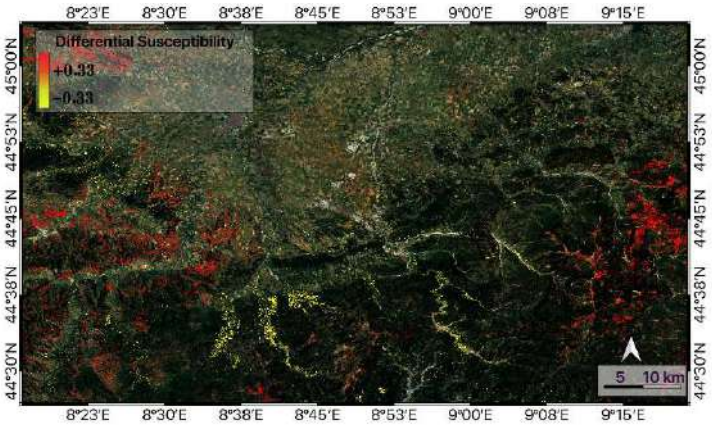

Figure 3.22: Spatial distribution of susceptibility difference between the R1 and R2 rainfall events.

In high-altitude regions like Monte Carmo in the southeast, soil moisture values were higher during the R1 event, yet the susceptibility values were higher during the R2 event due to a 240 mm increase in 15-day cumulative rainfall (Figure 3.23b). This highlights

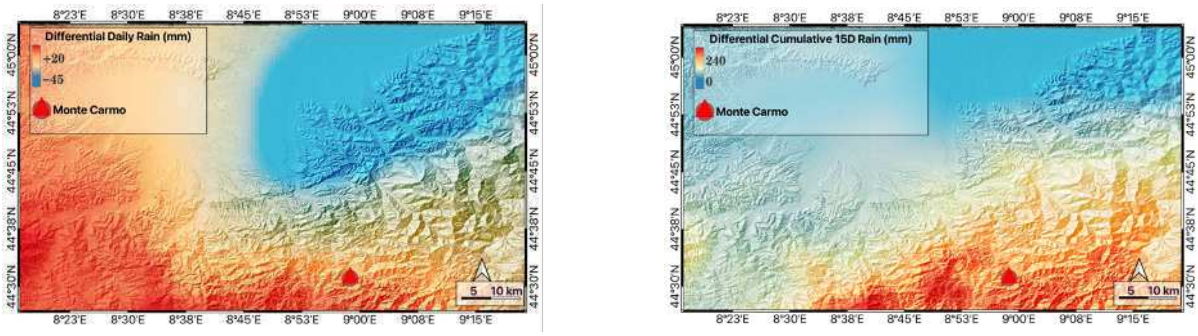

(a) Daily rainfall difference

(b) 15-day cumulative rainfall difference

Figure 3.23: Differences in daily rainfall (a) and 15-day cumulative rainfall (b) between the R1 and R2 rainfall events.

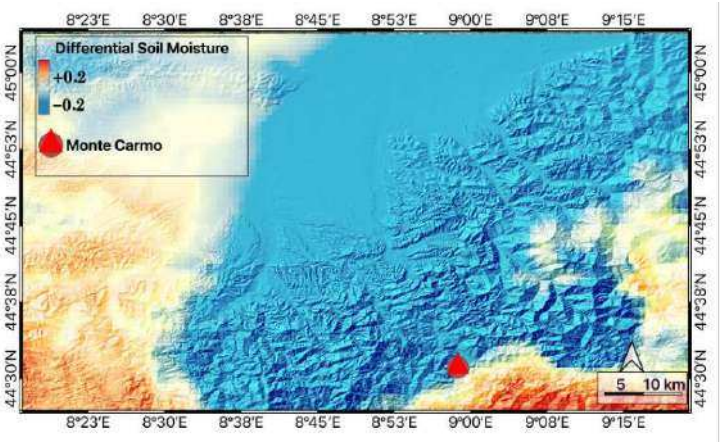

Figure 3.24: Spatial distribution of soil moisture difference between the R1 and R2 rainfall events.

the model's ability to weigh multiple hydrological factors simultaneously. However, these areas exhibited lower landslide probability due to specific landscape characteristics, as shown in Figure 3.22. In the central and southern parts of the study area, higher soil moisture values during the R1 event (Figure 3.24) correlated with accurate predictions of high-probability areas (yellow dots in Figure 3.22). For the R2 event, the western part of the study area experienced a higher number of landslides, driven by concentrated rainfall (Figure 3.21a) and elevated soil moisture (Figure 3.24), which the model successfully identified as high-risk zones.

The model's reliability is evident in its ability to differentiate the impacts of hydrological factors on landslide susceptibility. The findings align with Bogaard and Greco (2018) and Greco et al. (2023), who emphasized the role of antecedent soil moisture in regu-

lating rainwater infiltration for shallow landslides. Additionally, Moreno et al. (2024) highlighted the significance of 14-day cumulative precipitation, while Smith et al. (2023) identified 10-day pre-event rainfall as critical for landslide occurrences, consistent with the 15-day cumulative rainfall parameter used in this study. The proposed spatiotemporal landslide prediction model effectively integrates rainfall and soil moisture data to identify high-risk areas, demonstrating robust performance across varying hydrological conditions. The model's ability to account for dynamic parameters like 15-day cumulative rainfall and soil moisture enhances its predictive accuracy, making it a valuable tool for landslide susceptibility assessments.

3.6 Conclusion

This chapter presented a comprehensive analysis of landslide susceptibility in the Po River region of Italy, utilizing an optimized RF model. By integrating static conditioning factors with high-resolution dynamic variables, including daily and 15-day cumulative rainfall and soil moisture derived from satellite data, the model achieved robust predictive accuracy. The validation of the model against two significant rainstorm events in 2019 demonstrated its ability to effectively capture the spatial and temporal dynamics of landslide occurrences. Specifically, the predicted high-susceptibility zones showed strong alignment with observed landslide locations, highlighting the critical role of hydrological factors such as soil moisture and cumulative rainfall in landslide prediction.

The methodology developed in this study advances the understanding of landslide susceptibility by combining static and dynamic factors within a machine learning framework. The RF model's capability to account for varying intensities and distributions of rainfall and soil moisture underscores its potential as a reliable tool for identifying high-risk areas during extreme weather events. However, the site-specific nature of the results suggests that careful calibration is necessary when applying the model to different geological or climatic contexts.

While this chapter provides a robust foundation for landslide susceptibility assessment,

further exploration is warranted to enhance the model's generalizability. The subsequent chapter will present additional analyses, focusing on complementary approaches to refine the prediction of landslide occurrences and explore the temporal relationships between dynamic variables and landslide events. These efforts aim to build upon the findings presented here, offering a more comprehensive framework for landslide risk management.

Chapter 4

Second Phase: Integrating dynamic precipitation and soil moisture conditions into susceptibility assessment

4.1 Slope Units Delineation and Classification

In Chapter 3, the analysis was based on a pixel-level approach, where the study area was divided into regular raster grids. This method provided detailed insights into landslide susceptibility at a fine spatial resolution. However, the use of uniform pixels introduces an artificial structure that does not always correspond to natural geomorphological or hydrological processes. In Chapter 4, the focus shifts toward slope units (SUs), which represent irregular polygons bounded by drainage and divide lines. Unlike raster cells, slope units capture the natural organization of the landscape: they represent hillslopes as coherent entities, internally homogeneous but contrasting with adjacent units. This conceptual and methodological shift allows the analysis to align more closely with the real dynamics of erosion, water flow, and slope stability, and thus provides more meaningful susceptibility patterns across Italy's varied terrain, from the Apennines to valley systems. Figure 4.1 illustrates the spatial distribution of documented landslides across the slope unit framework, demonstrating the heterogeneous distribution of slope failures within the study area.

For this chapter, slope units were obtained from the benchmark dataset by Alvioli et al. (2024), which includes 7,360 slope units covering approximately 4,100 km^2 in Central

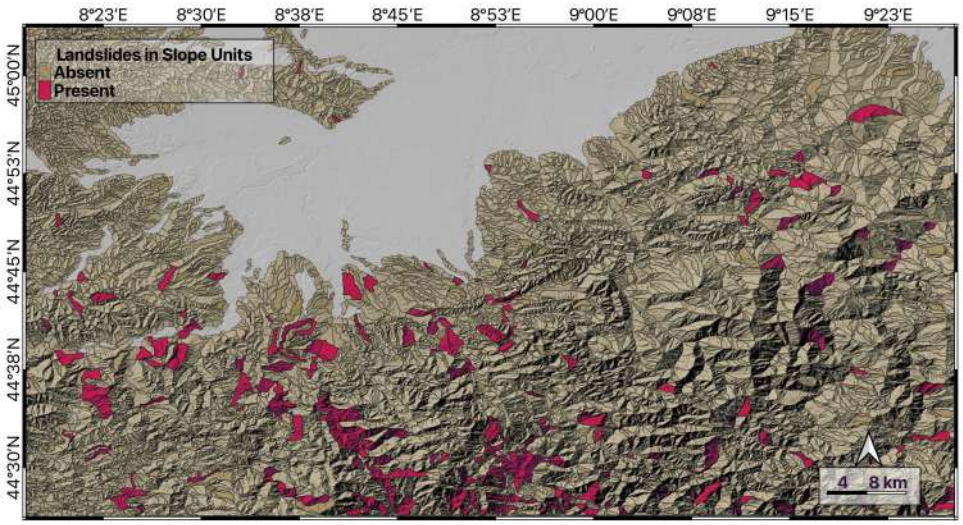

Figure 4.1: Landslide Presents in Study Area based on Slope units

Italy. This dataset is derived from the national slope unit map developed by Alvioli et al. (2020) using the r.slopeunits software. The software, implemented in GRASS GIS, subdivides hydrological basins into slope units by iteratively adapting to local morphology, varying upslope contributing areas and aspect-homogeneity thresholds. This produces units that are larger in flat areas and smaller in steep, rugged terrain. The Central Italian subset was selected by Alvioli et al. (2024) for its diverse physiography (e.g., Umbria–Marche Apennines, Tiber River basin) and was enriched with morphometric variables from the 25-m EU-DEM, soil attributes from SoilGrids(Hengl et al., 2017), and a landslide inventory of translational slides from the ISPRA database(Istituto Superiore per la Protezione e la Ricerca Ambientale (ISPRA), 2021). By adopting this benchmark dataset without modifications, the analysis remains reproducible and consistent with a framework already recognized for comparative landslide susceptibility studies.

To characterize slope units, a set of morphometric, hydrological, and pedological variables was aggregated, reflecting processes relevant to translational landslides. These variables describe terrain shape, slope gradients, curvature, soil properties, and hydrological proxies. Table 4.1 summarizes the features, their acronyms, sources, and intended role in modeling.

For each slope unit, means and standard deviations were computed for the selected fea-

Table 4.1: Features used for slope unit classification

Name	Acronym	Reference
Maximum distance within SU	MD	Forman and Godron (1986)
Maximum distance / $\sqrt{\text{Area}}$	MD/$\sqrt{A}$	Forman and Godron (1986)
Mean slope steepness	Mean Slope	Zevenbergen and Thorne (1987)
SD of slope within SU	SD Slope	Zevenbergen and Thorne (1987)
Eastness	Eastness	Lombardo et al. (2018b)
Northness	Northness	Lombardo et al. (2018b)
Plan curvature	Plan Cur	Heerdegen and Beran (1982)
Profile curvature	Prof Cur	Heerdegen and Beran (1982)
Distance to stream	Dist2Stream	Arabameri et al. (2019)
Depth to bedrock (2.4 m)	BDRICM	Hengl et al. (2017)
Bulk density	BLDFIE	Hengl et al. (2017)
Clay content (%)	CLYPPT	Hengl et al. (2017)
Sand content (%)	SNDPPT	Hengl et al. (2017)
Silt content (%)	SLTPPT	Hengl et al. (2017)

tures.Figure 4.1 illustrates the delineated slope units, while Figure 4.2 presents the distribution of selected features across slope units, including mean elevation (Figure 4.2a), mean slope angle (Figure 4.2b), mean eastness (Figure 4.2c), silt content (Figure 4.2d), sand content (Figure 4.2e), and clay content (Figure 4.2f). These subfigures highlight the contrast between steep Appennine areas and valley floors, capturing variations in terrain and soil properties. An important addition to the classification comes from SoilGrids data, which provide soil-related variables such as bulk density and particle size fractions at 250-m resolution. These were averaged for each unit, linking subsurface conditions with slope stability. For example, a higher proportion of clay (CLYPPT, Figure 4.2f) indicates lower permeability and potential zones of instability, while silt (SLTPPT, Figure 4.2d) and sand (SNDPPT, Figure 4.2e) content influence drainage and shear strength. By incorporating these attributes, the analysis accounts for both surface morphology and soil characteristics, offering a more robust basis for landslide susceptibility modeling. This approach is consistent with Alvioli et al. (2024) in promoting reproducible, data-driven assessments of landslide hazards in complex terrains.

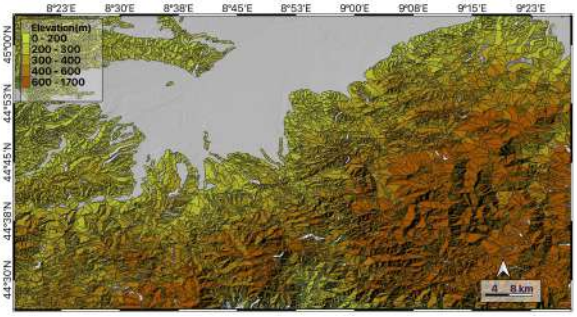

(a) Mean Elevation

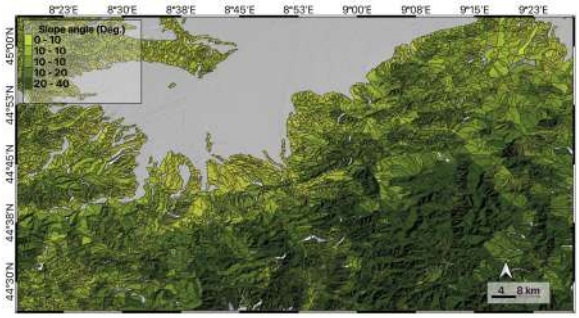

(b) Mean Slope Angle

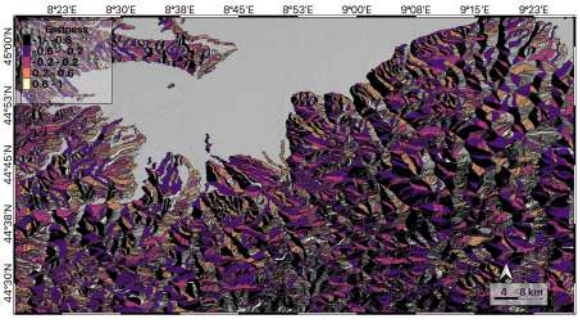

(c) Mean Eastness

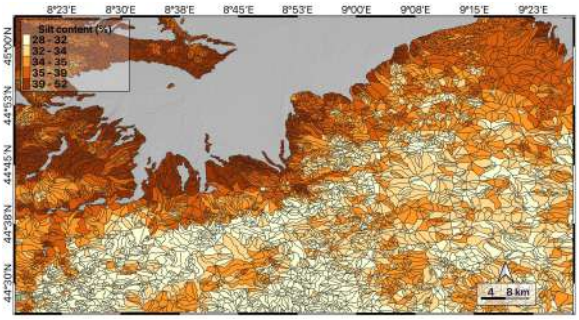

(d) Silt Content

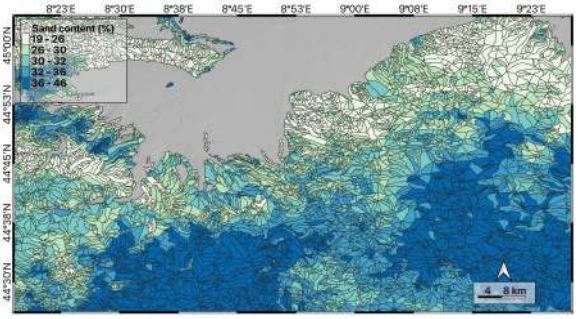

(e) Sand Content

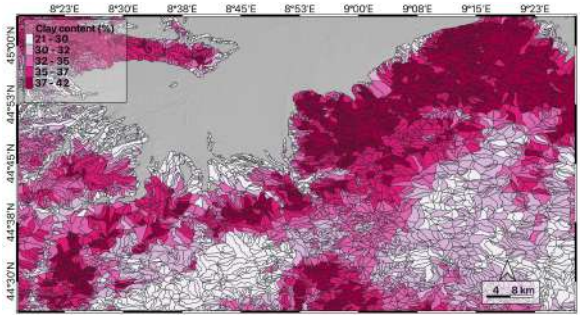

(f) Clay Content

Figure 4.2: Distribution of selected features across slope units: mean elevation, mean slope angle, mean eastness, and soil particle size fractions (silt, sand, clay).

4.2 Dynamic RF Model Configuration

To build a strong system for assessing landslide probability, three methods were developed to identify non-landslide events. These methods used different spatial and temporal criteria compared to known landslide events, with the goal of determining which approach best distinguished landslide and non-landslide conditions. The experiment explored spatial rules (same slope unit vs. different slope unit) and temporal rules (same day vs. different day). All methods started from a balanced dataset containing an equal number of landslide and non-landslide events (1:1 ratio).

Table 4.2: Non-landslide event identification strategies

Config.	Spatial criterion	Temporal criterion	Objective
1	Same slope unit	Different day	Spatial consistency
2	Different slope unit	Same day	Temporal consistency
3	Different slope unit	Different day	Maximum discrimination

The dataset included 412 landslide events. Non-landslide events were randomly sampled to ensure they represented different environmental factors such as slope angle, land cover, and rainfall intensity.

For Configuration 1, non-landslide events were selected from the same slope units as landslides but on days preceding the failure. This method captures stable conditions in slopes that later failed, focusing on temporal variation while keeping spatial factors such as geology and topography constant. Days were randomly selected from the period before each landslide, excluding dates with any landslide activity.

Configuration 2 selected non-landslide events from different slope units but on the same days as landslides. Since landslides often occur simultaneously during major triggering events (e.g., storms with multiple failures), this method isolates spatial differences between slope units under identical meteorological conditions. Non-landslide slope units were randomly chosen among those that did not fail on landslide days, thus maintaining temporal consistency.

Configuration 3 selected non-landslide events from different slope units and on different days (excluding landslide days), maximizing spatial and temporal separation. Bootstrap testing showed stable model performance with low variability.

Each configuration maintained a balanced dataset (412 landslide and 412 non-landslide events). The dataset was split into training (70%) and testing (30%) subsets, maintaining class balance. Model tuning was performed on the training set using 5-fold cross-validation and grid search, with performance evaluated by the Area Under the ROC Curve (AUC). The best hyperparameters were used to train the final RF model on the complete training set, and evaluation was conducted on the independent test set. This process was repeated 10 times with different random splits for robust performance estimation.

The values reported are averages across the 10 runs, while the confusion matrices below represent one representative split for clarity. Small numerical differences reflect the random resampling across runs.

Table 4.3: Confusion matrices and performance metrics for Configurations 1–3 (1:1 ratio, representative test set)

	Config 1		**Config 2**		**Config 3**	
	Pred: L	**Pred: NL**	**Pred: L**	**Pred: NL**	**Pred: L**	**Pred: NL**
Actual: L	85 (TP)	25 (FN)	86 (TP)	24 (FN)	102 (TP)	21 (FN)
Actual: NL	21 (FP)	96 (TN)	14 (FP)	97 (TN)	23 (FP)	98 (TN)
POD (Recall)	0.77		0.78		0.83	
FAR (FP / (TP + FP))	0.20		0.14		0.18	
AUC	0.82		0.85		0.90	

Figure 4.3 illustrates the Probability of Detection (POD = TP/(TP+FN)) and the False Alarm Ratio (FAR = FP/(TP+FP)) for the three configurations at a 1:1 class ratio. Using meteorological terminology, POD corresponds to Recall (sensitivity) and FAR corresponds to 1 minus Precision. Configuration 3 achieved the highest detection rate (POD = 0.83) and the strongest overall discrimination (AUC = 0.90), while maintaining a moderate FAR of 0.18. Configuration 2 offered a balanced trade-off, with slightly lower POD (0.78) but the lowest FAR (0.14), making it suitable for applications prioritizing fewer false alerts.

Figure 4.3: Comparison of Probability of Detection (POD = Recall), False Alarm Ratio (FAR = FP/(TP+FP)), and Area Under the ROC Curve (AUC) across configurations at a 1:1 ratio.

To approximate real-world early warning conditions, additional experiments tested varying class imbalance ratios (1:1, 1:2, 1:3), as summarized in Table 4.4. Although real systems may encounter much higher imbalance (e.g., 1:1000), moderate ratios were selected to maintain model stability and interpretability.

Table 4.4: Database imbalance scenarios for false-positive analysis

Ratio (L:NL)	**Landslide events**	**Non-landslide events**
1:1	412	412
1:2	412	824
1:3	412	1236

Table 4.5: Confusion matrices and performance metrics for Configuration 3 at varying imbalance ratios (representative test set).

	1:2 Ratio		**1:3 Ratio**	
	Pred: L	**Pred: NL**	**Pred: L**	**Pred: NL**
Actual: L	102 (TP)	21 (FN)	101 (TP)	22 (FN)
Actual: NL	39 (FP)	208 (TN)	52 (FP)	319 (TN)
POD (Recall)	0.83		0.82	
FAR (FP / (TP + FP))	0.28		0.34	
AUC	0.89		0.88	

As shown in Table 4.5, increasing the imbalance ratio (adding more non-landslide samples) slightly raised the False Alarm Ratio—from 0.18 [0.16–0.20] at 1:1 to 0.34 [0.32–0.36] at 1:3—while POD remained stable (0.83 → 0.82). The AUC values remained high

(>0.88) across all ratios, indicating that the model maintained excellent class separation even under moderate imbalance. This trend aligns with expectations: as the number of negative samples increases, the probability of issuing a false alarm (FAR) rises slightly due to the larger pool of non-landslide cases, while overall discrimination (AUC) remains largely unaffected. Thus, a moderate imbalance better reflects real-world conditions while preserving strong detection capability.

4.3 Results and Discussion

4.3.1 Results of Temporal Analysis of Landslide Susceptibility Across Slope Units During Major Rainstorm Events

The spatial susceptibility analysis presented in Chapter 3 demonstrated the model's capability to identify highly susceptible areas across northwestern Italy. However, spatial mapping alone provides only a snapshot of landslide susceptibility at specific moments in time. To fully understand the mechanisms driving landslide occurrence, it is essential to examine how hydrological conditions evolve temporally and how these changes translate into variations in landslide probability. This section extends the previous analysis by investigating the temporal dynamics of landslide susceptibility during two significant rainstorm events that affected the study region in autumn 2019: R1 (October 20^{th}, 2019) and R2 (November 23^{rd}, 2019), which together triggered 84 landslides.

The analysis was conducted across all 7,200 slope units in the study area throughout the entire observation period from 2016 to late 2021, generating approximately 13 million individual daily probability estimates (7,200 units × approximately 1,800 days). This comprehensive dataset encompasses the full spatial and temporal variability in landslide susceptibility across the region.For a detailed presentation, four representative slope units were selected for each event—two that experienced landslides and two that remained stable—to illustrate how the model responds to hazardous conditions while maintaining appropriate discrimination in areas where landslides did not occur. These eight exemplar

cases (hereafter referred to as L1–L4 for landslide units and S1–S4 for stable units) span the range of observed responses and allow comprehensive evaluation of model performance under diverse geomorphic and hydrological conditions (Table 4.6).

For each slope unit, detailed time series of four key variables were examined over 40-day windows centered on each critical event day (20 days before and after): daily rainfall (measured in mm), 7-day cumulative rainfall (mm), soil moisture, and modeled landslide probability (unitless value ranging from 0 to 1). This 40-day window length was selected to capture both the build-up of antecedent wetness conditions—which previous studies(Moreno et al., 2024; Lombardo et al., 2020b) indicate typically operate over 7–15 day timescales in similar geological settings—and the post-event drainage phase during which elevated susceptibility conditions gradually dissipate. The window provides sufficient temporal context to observe how cumulative rainfall and soil moisture progressively increase susceptibility before activation phase, how the system responds during the critical day itself, and how conditions recover afterward.

Each slope unit is described by a combination of static attributes and dynamic factors. The static attributes include topographic features such as slope angle, aspect, plan and profile curvature, and elevation, as well as soil properties like texture (expressed by the percentage of clay, silt, and sand), bulk density, and depth to bedrock. Geomorphological indicators, including distance to streams and topographic position, are also considered. The dynamic factors consist of rainfall data obtained from satellite-based precipitation products with a 1-km spatial resolution and soil moisture data.

Table 4.6: Summary of key metrics for exemplar slope units during R1 (October 20^{th},2019) and R2 (November 23^{rd} 2019). Values refer to the event day unless otherwise stated. L1–L4 denote landslide units; S1–S4 denote stable units.

Event & Unit	**Outcome**	**Prob.**	**1D Rain (mm)**	**7-D Cumul. Rain (mm)**	**Soil Moist. (%)**
R1: L1 (157008)	Landslide	0.94	26.97	114.18[a]	45
R1: L2 (21393)	Landslide	0.85	48.94	144.80[a]	46
R1: S1 (20823)	Stable	0.28	55.95	140.05	45
R1: S2 (21283)	Stable	0.54	26.93	107.80	43
R2: L3 (156034)	Landslide	0.90[b]	27.63	156.90	44
R2: L4 (154454)	Landslide	0.79	16.22	129.49	46
R2: S3 (150219)	Stable	0.33	13.38	96.72	43
R2: S4 (156895)	Stable	0.51	30.45	144.13	47

[a]Peak occurred 1 day before event; [b]Peak 1 day before event; S1 prob. peak 3 days before event

The first major rainstorm event (R1) occurred on October 20^{th}, 2019, bringing intense rainfall to northwestern Italy and triggering 39 natural terrain landslides across the study region. Maximum daily rainfall intensities during this event reached approximately 73 mm, as documented in the temporal precipitation analysis presented in Figure3.18.

For detailed examination of this event, four slope units were selected representing the spectrum of observed responses to the regional rainfall pattern (Figure4.4).

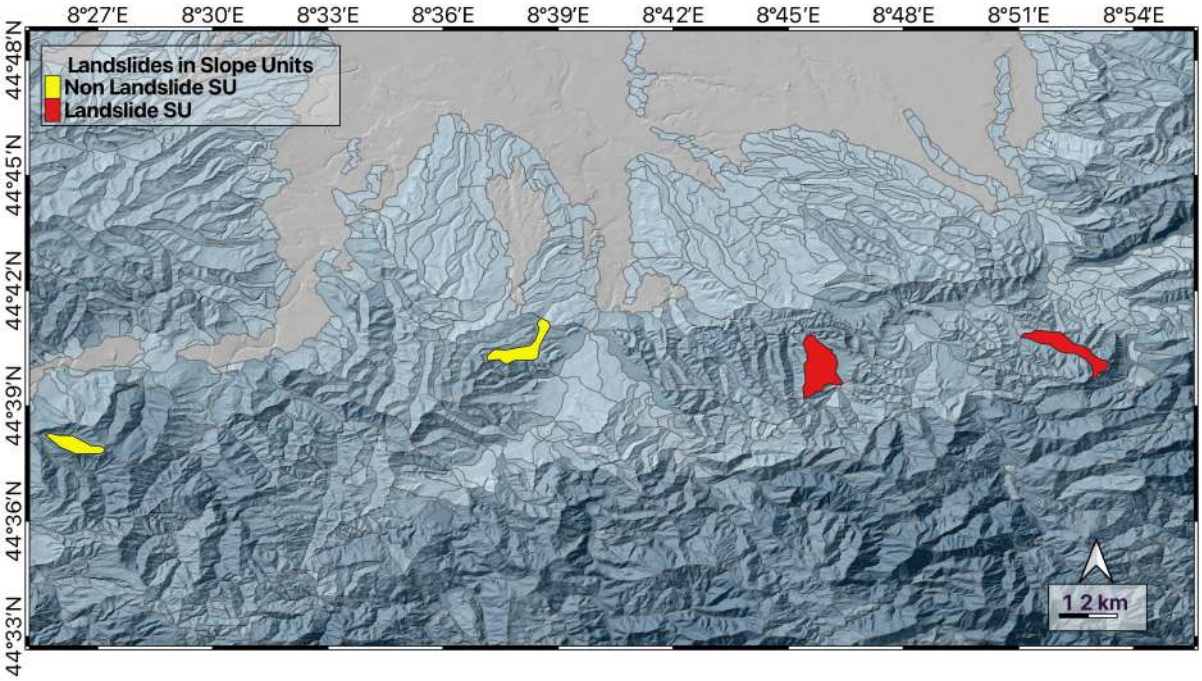

Figure 4.4: Landslide and non landslide on October 20^{th}

Landslide units L1 (SU_157008) and L2 (SU_21393) both experienced confirmed landslide failures during R1, while stable units S1 (SU_20823) and S2 (SU_21283) remained stable throughout the event despite exposure to the same general meteorological conditions. These units were strategically chosen to represent the topographic and hydrological variability present across the study area, including differences in slope steepness (ranging from moderate to steep gradients), aspect (which influences solar radiation receipt and evapotranspiration rates), soil composition (variations in clay, silt, and sand content affecting water retention and cohesion), and drainage characteristics (which control how rapidly infiltrating water is transmitted through or removed from the soil profile). This selection strategy ensures that the temporal analysis captures the range of site-specific factors that modulate landslide susceptibility under similar regional forcing conditions.

Landslide-Affected Slope Units During R1: Temporal Evolution and Physical Processes. The temporal evolution of hydrological conditions and landslide probability in the landslide-affected slope units reveals clear diagnostic patterns that distinguish these locations from stable areas. Figure 4.5 presents comprehensive time series for landslide units L1 and L2, both of which experienced documented landslide failures on October 20^{th}, 2019. The probability time series panels include colored susceptibility zone overlays derived empirically from the historical distribution of probability values versus observed landslide occurrences: very low susceptibility (0.0–0.2, rendered in green), moderate susceptibility (0.2–0.4, yellow), medium susceptibility (0.4–0.6, orange), high susceptibility (0.6–0.8, red), and very high susceptibility (0.8–1.0, dark red). These thresholds reflect statistical analysis of the relationship between modeled probabilities and actual landslide frequencies rather than arbitrary divisions, ensuring that the categorization has empirical foundation and operational utility, reinforcing the critical importance of antecedent wetness in triggering slope failures.

In landslide unit L1, the landslide probability reached its maximum value of 0.94 precisely on the critical day (October 20^{th}, 2019), placing it firmly within the very high susceptibility zone and representing one of the highest probability values observed across all examined cases. This peak probability occurred in conjunction with a daily rainfall accu-

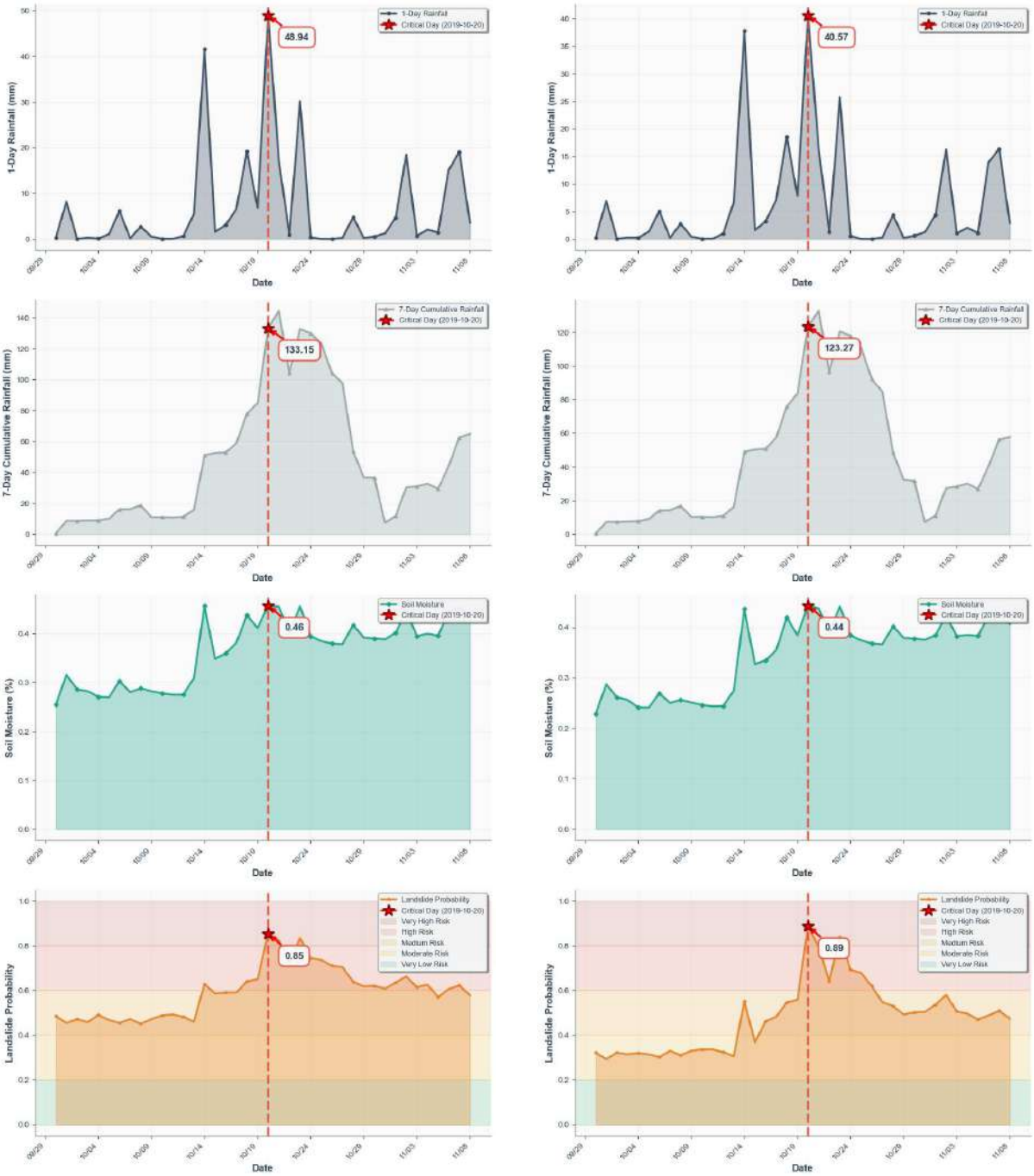

(a) (b)

Figure 4.5: Temporal evolution of hydrological conditions for landslide-affected slope units during the R1 rainfall event (October 20^{th}, 2019). (a) Slope unit L1 (SU 21393); (b) Slope unit L2 (SU 156245). Each panel shows daily rainfall, 7-day cumulative rainfall, soil moisture, and predicted landslide susceptibility over the event period.

mulation of 26.97 mm and a soil moisture content of 45%. Notably, the 7-day cumulative rainfall peaked at 114.18 mm one day prior to the event (October 19), then decreased to 107.16 mm on the event day itself as the most distant day in the rolling 7-day window dropped out of the calculation. This temporal pattern carries significant physical meaning: it demonstrates how the model appropriately integrates antecedent moisture conditions accumulated over multiple days into its probability assessments, rather than responding solely to instantaneous daily rainfall. The cumulative rainfall of 114.18 mm over the preceding week indicates substantial progressive saturation of the soil profile, filling available pore spaces and elevating the water table. Under these close -to-saturation conditions, even the moderate daily rainfall of 26.97 mm on October 20^{th} was sufficient to trigger slope failure, because the soil moisture deficit that would normally buffer the effects of new precipitation had been effectively eliminated by previous rainfall events.

The soil moisture time series for L1 displays a characteristic progressive increase pattern beginning approximately 10–12 days before the critical event. Soil moisture values rose gradually from baseline levels around 35–38% to peak values of 45% on the event day, reflecting the systematic accumulation of water in the soil profile as successive rainfall events incrementally filled available pore spaces and raised the position of the saturation front within the profile. In cohesive soils typical of the northwestern Italy study region—which contain significant proportions of fine particles that influence both water retention characteristics and mechanical behavior—increasing moisture content reduces matric suction in the unsaturated zone and increases positive pore water pressure in saturated zones(Cho et al., 2024; Shah et al., 2025). According to unsaturated soil mechanics principles, as matric suction decreases with increasing water content, the contribution of suction to shear strength diminishes, reducing the soil's resistance to shearing. When full saturation is approached and positive pore pressures develop, the effective stress transmitted through the soil skeleton decreases further, leading to additional strength reduction. The precise temporal alignment of peak soil moisture with peak landslide probability on the event day illustrates the model's sensitivity to this critical physical triggering mechanism and suggests that the model has learned to recognize the moisture

thresholds at which soil strength degradation becomes sufficient to initiate failure. The remarkably high probability of 0.94 in L1 indicates that this slope unit was operating very close to its stability limit under the prevailing hydrological conditions.

Landslide unit L2 displayed broadly similar temporal patterns but with even more pronounced rainfall intensities and moisture accumulation. The landslide probability in this unit reached 0.85 on the critical day, accompanied by a daily rainfall accumulation of 48.94 mm and soil moisture of 46%. The 7-day cumulative rainfall peaked at 144.80 mm one day before the event (October 19), representing the highest cumulative value among all four slope units examined for the R1 event and approximately 30 mm higher than the peak value in L1. The relationship between cumulative rainfall magnitude and landslide occurrence is particularly evident in this case. The 144.80 mm accumulated over the preceding week exceeded the 114.18 mm observed in L1, and this difference correlates with the higher soil moisture content achieved (46% versus 45%). However, despite L2 receiving substantially higher cumulative rainfall and achieving higher soil moisture than L1, its probability (0.85) was actually lower than L1's probability (0.94). This differential response demonstrates that the model integrates multiple stability factors beyond just rainfall and moisture forcing. L1 likely possesses some topographic or material characteristics that made it more susceptible even under somewhat lower forcing conditions—perhaps a steeper slope angle, less favorable drainage configuration, or weaker soil properties—resulting in the higher probability despite lower cumulative rainfall. This behavior illustrates the model skills in accounting for site-specific vulnerability factors that modulate the relationship between hydrological forcing and failure likelihood.

The temporal sequencing observed in both landslide-affected units during R1 reveals an important characteristic of rainfall-triggered shallow landslide processes in this region that has implications for both scientific understanding and operational warning systems. The peak in 7-day cumulative rainfall occurred one day before the critical day in both cases (October 19 for an October 20^{th} event), while the landslide probability peaked on the event day itself (October 20^{th}). This consistent one-day lag reflects fundamental physical processes governing how rainfall infiltrates through soil profiles and generates

the pore water pressure conditions that trigger failures. The initial rainfall from days 7–2 before the event saturates surface soil layers and begins filling deeper horizons, but complete saturation of the full potentially unstable soil thickness—which may extend several meters deep in the colluvial and residual soils typical of the study area—requires additional time as water percolates downward through progressively deeper and initially drier layers. The final daily rainfall on the event day provides the ultimate triggering mechanism, either by completely saturating remaining unsaturated zones at the base of the mobile soil layer or by rapidly increasing pore water pressure throughout the already-near-saturated profile, pushing effective stress to critically low values. The model's ability to capture this realistic temporal progression, including the appropriate lag between peak cumulative forcing and peak probability response, demonstrates that it has learned physically meaningful relationships based on actual hydrological processes rather than simply establishing spurious statistical correlations between rainfall totals and landslide occurrence dates.

Both landslide-affected units entered the very high susceptibility zone (probability > 0.80) on or immediately before the event day, with probabilities remaining notably elevated for several days afterward before gradually declining as soils drained and hydrological conditions stabilized. This sustained elevation of probability during the post-event period reflects the reality that saturated slopes remain in a vulnerable state for several days after peak rainfall, as pore pressures equilibrate and drainage processes slowly restore effective stress to stable values. This temporal pattern provides valuable information for operational early warning applications. The model begins to indicate progressively elevating susceptibility levels several days before the critical event as cumulative rainfall and soil moisture steadily increase, potentially providing advance warning time measured in days rather than hours. Equally important, the sustained high probability for several days after peak rainfall indicates that slopes remain unstable during the immediate post-storm period, consistent with field observations that delayed failures sometimes occur hours to days after rainfall cessation as pore pressures redistribute within the slope and drainage networks concentrate flow.

Stable Slope Units During R1: Understanding Non-Occurrence and Model Discrimination. The comparison between landslide-affected units and stable units reveals the model's ability to maintain appropriate susceptibility evaluations in areas that did not fail despite exposure to the same regional storm system. Figure 4.6 presents detailed time series for stable units S1 and S2, both of which remained stable throughout the R1 event despite receiving significant rainfall. Stable unit S1 presents a particularly instructive case that demonstrates the model's sophisticated discrimination capability. This unit maintained a probability of only 0.28 on the critical day (October 20^{th}), placing it in the moderate susceptibility zone (0.2–0.4) and well below the high susceptibility threshold of 0.6. Notably, the peak probability of 0.40 occurred three days before the event, after which the probability declined even as additional rainfall continued. The daily rainfall on October 20^{th} was 55.95 mm—substantially higher than the 26.97 mm and 48.94 mm observed in the landslide units L1 and L2. This represents a striking paradox: S1 experienced the highest event-day rainfall among all four R1 slope units examined, yet it did not fail and maintained a low probability. The 7-day cumulative rainfall reached 140.05 mm on the event day (with a peak of 151.03 mm one day prior), comparable to or exceeding the cumulative rainfall in landslide unit L2 (144.80 mm peak). The soil moisture in S1 reached 45% on the event day, identical to landslide unit L1 and only slightly lower than L2's 46%. This case provides powerful evidence of the model's ability to integrate site-specific stability factors that go beyond simple rainfall and moisture thresholds. Despite receiving among the highest forcing of all examined units—with event-day rainfall exceeding 55 mm, 7-day cumulative rainfall exceeding 140 mm, and soil moisture reaching 45%—S1 remained stable and the model correctly assigned it a low probability (0.28 on event day, with peak of 0.40 occurring earlier). This demonstrates that S1 possesses inherent characteristics conferring substantial resilience to landslide triggering. Several factors could explain this resilience: the slope angle may be significantly more moderate, reducing gravitational driving stress below critical levels even when soils are saturated; the soil may have exceptionally high cohesion due to specific mineralogical composition or cementation; internal drainage characteristics may be superior, allowing

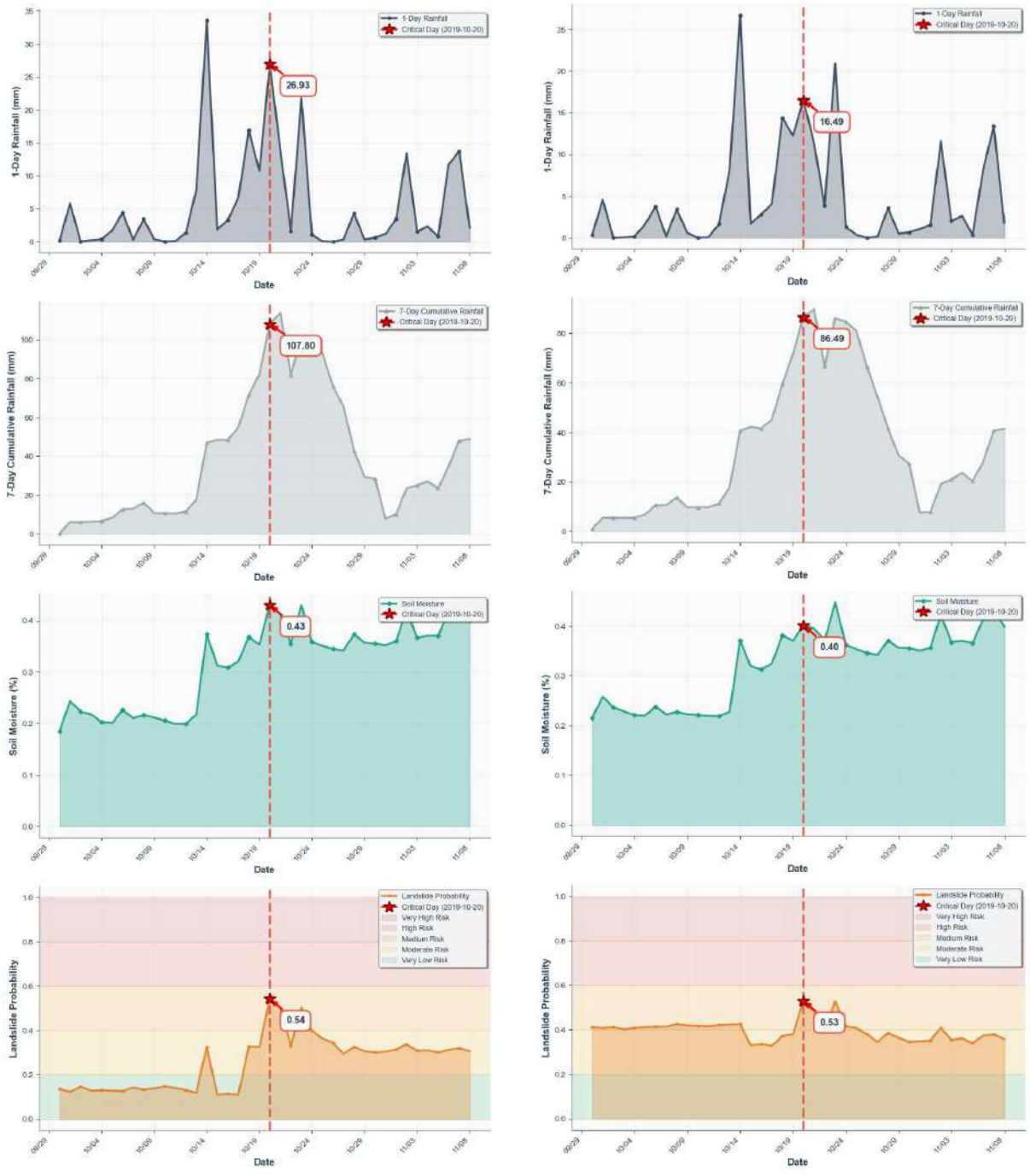

(a) (b)

Figure 4.6: Temporal evolution of hydrological conditions for stable slope units during the R1 rainfall event (October 20^{th}, 2019). (a) Slope unit S1 (SU 21283); (b) Slope unit S2 (SU 157017). Each panel shows daily rainfall, 7-day cumulative rainfall, soil moisture, and predicted landslide susceptibility over the event period.

rapid dissipation of pore pressures through efficient vertical or lateral flow pathways; the bedrock may be shallow, limiting the thickness of potentially unstable material; or vegetation may provide substantial root reinforcement. The model has learned to recognize these compensating factors and appropriately moderate the probability despite extreme hydrological forcing. This capability is precisely what distinguishes sophisticated machine learning models from simple threshold-based warning systems, which would have issued high-severity false alarms for S1 based solely on its rainfall and moisture values.

The temporal pattern in S1 is also informative. The probability peaked at 0.40 three days before the event and then declined to 0.28 by the event day, even as substantial additional rainfall accumulated. This declining probability trend despite continuing rainfall suggests that the model recognized that the slope was not approaching critical conditions despite the forcing, possibly because drainage processes were keeping pace with infiltration or because the inherent stability margin remained adequate. This temporal behavior further validates the model's physical basis and its integration of dynamic hydrological processes.

Stable unit S2 showed patterns more typical of stable slopes under moderate forcing conditions, with a maximum landslide probability of 0.54 on the critical day—essentially at the boundary between medium and high susceptibility zones. Daily rainfall was 26.93 mm, comparable to L1's value. The 7-day cumulative rainfall reached 107.80 mm, lower than both landslide units (114.18 mm and 144.80 mm) but still representing substantial accumulation. Soil moisture was 43%, slightly lower than the landslide units' 45–46%. The case of S2 demonstrates appropriate model discrimination under conditions that approach but do not quite reach critical thresholds. The cumulative rainfall of 107.80 mm falls somewhat short of the 115–145 mm range consistently associated with failures in the R1 cases, and the model appropriately reflected this through a probability (0.54) that remains below the high-susceptibility threshold despite being elevated. This unit likely possesses moderately favorable stability characteristics—perhaps slightly gentler slopes or somewhat better drainage than the landslide units—that increase the rainfall threshold required for failure. The model's ability to maintain appropriate discrimination at these intermediate forcing levels, where conditions are substantial but subcritical, is essential

for operational utility.

The temporal evolution patterns in both stable units show gradual increases in soil moisture and landslide probability as the October rainfall period progressed, but these increases remained measured rather than dramatic. After the event day, probabilities declined gradually back toward baseline levels as soils drained, following similar recovery timescales as the landslide units but from notably lower peak values. The satellite-based precipitation dataset employed in this study, with 1-km spatial resolution, captures the spatial variability in rainfall that contributed to differences between units, though some sub-kilometer scale heterogeneity may remain unresolved.

Event R2: November 23^{rd}, 2019 – Enhanced Antecedent Conditions and Broader Impacts. The second major rainstorm event (R2) occurred approximately one month after R1, on November 23^{rd}, 2019. This temporal spacing is significant because it meant that soils had not fully recovered to pre-storm baseline conditions before being subjected to a second major rainfall event. R2 impacted a broader geographical area than R1, with documented effects extending from northeastern portions of the study region southward through Liguria and affecting communities across a wider swath of northwestern Italy. The event resulted in 45 natural terrain landslides (compared to 39 in R1) and directly affected more than 120 people. As documented in Figure 3.18's detailed temporal precipitation analysis, the maximum daily rainfall intensities during R2 were comparable to those observed during R1, with peak values again approaching 70–73 mm. This similarity in peak daily intensities is noteworthy because it demonstrates that the difference in landslide outcomes between the two events (45 versus 39 failures) cannot be attributed to differences in maximum daily forcing. Instead, the critical distinction between R1 and R2 lies in their antecedent moisture conditions. The cumulative 15-day precipitation prior to the November 23^{rd} event reached higher values than the 15-day totals preceding October 20^{th}, as illustrated particularly clearly in the third panel of Figure 3.18 which tracks cumulative precipitation. This elevated antecedent moisture reflects the fact that soils retained hydrological memory from the October rainfall events and subsequent early November precipitation, meaning that less additional rainfall was

required to push soil moisture back up to critical saturation levels by late November.

For detailed examination of R2, four slope units were again selected spanning the range of observed responses: landslide units L3 (SU_156034) and L4 (SU_154454), which experienced documented landslide failures, and stable units S3 (SU_150219) and S4 (SU_156895), which remained stable throughout the event(Figure4.7.)

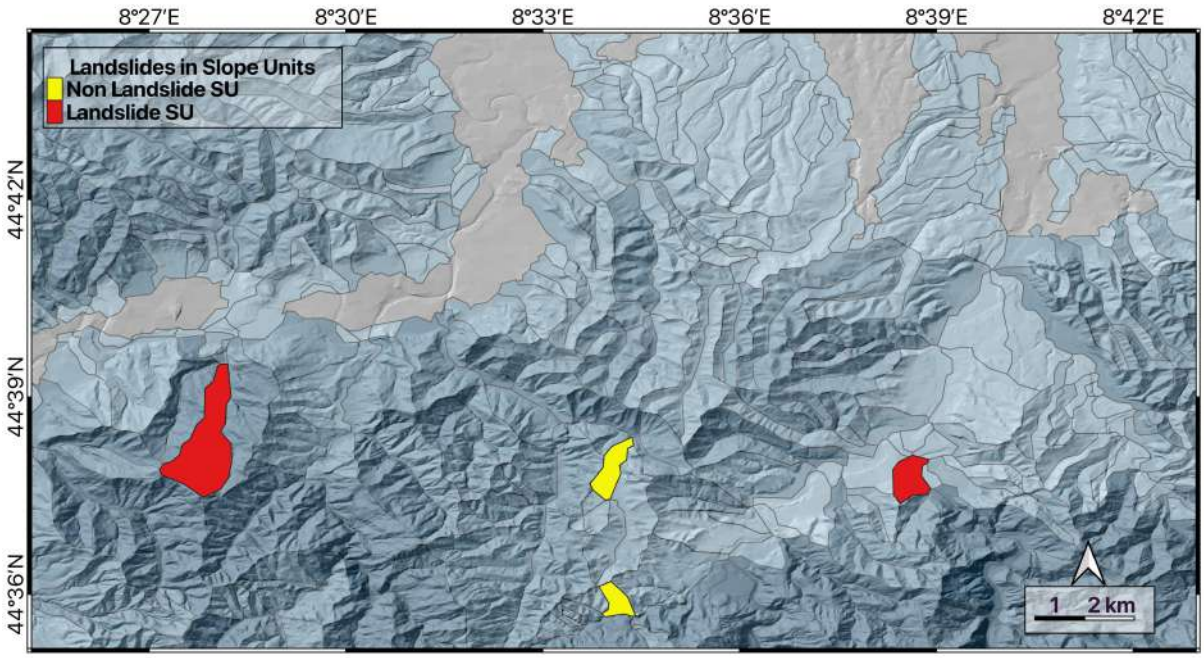

Figure 4.7: Landslide and non landslide on November 23^{rd}

Landslide-Affected Slope Units During R2: Amplified Response to Cumulative Wetting. Figure 4.8 presents the temporal evolution of conditions in the two landslide-affected slope units during R2, L3 and L4. The patterns observed in these units demonstrate even more clearly than R1 how prolonged antecedent rainfall accumulation amplifies landslide susceptibility by progressively reducing the additional rainfall required to trigger failure.

Landslide unit L3 exhibited a maximum landslide probability of 0.90, representing the highest probability value among the R2 units and approaching the theoretical maximum of 1.0. Notably, this peak probability occurred one day before the critical event day (November 22 rather than November 23^{rd}), a temporal pattern slightly different from most R1 cases where peaks occurred precisely on the event day. On November 23^{rd}

itself, daily rainfall was 27.63 mm, lower than the 48.94 mm observed in R1 landslide unit L2 and comparable to L1's 26.97 mm, yet a landslide occurred nonetheless. The 7-day cumulative rainfall reached an extraordinary 156.90 mm on the event day, approximately 40–43 mm higher than the peak cumulative values observed in R1 landslide units (114.18 mm and 144.80 mm). Soil moisture on November 23^{rd} was 44%, slightly lower than the R1 landslide values of 45–46%, but examination of the temporal evolution shows that soil moisture had already reached this elevated level approximately five days before the event and remained persistently high throughout the period, indicating sustained near-saturation conditions rather than a transient peak. The one-day advance of peak probability relative to the critical day in L3 carries important physical implications. It suggests that the slope was already at or extremely near failure conditions before the final rainfall on November 23^{rd}. The extraordinarily high cumulative rainfall of 156.90 mm over the preceding seven days—representing 40 mm more than L1's 114.18 mm—indicates that soils were completely or nearly completely saturated well before the event day. When a soil profile is fully saturated, all pore spaces are filled with water and any additional infiltration must either be accommodated by positive pore water pressures (exceeding atmospheric pressure) that further reduce effective stress, must generate immediate surface runoff, or must displace water laterally through subsurface flow. In this condition of full or near-full saturation, slope stability is maintained by only a small residual margin of effective stress, and even slight additional rainfall can provide the final disturbance needed to trigger failure. The relatively modest additional rainfall on November 23^{rd} (27.63 mm) was sufficient to trigger the landslide despite being well below R1 landslide unit L2's event-day value of 48.94 mm, precisely because no soil moisture deficit remained to buffer the effect of new precipitation. This temporal pattern illustrates an important characteristic of landslide susceptibility during prolonged wet periods: once soils reach critical saturation, even moderate additional rainfall becomes highly effective at triggering failures because the system has lost its capacity to accommodate new water without generating critically destabilizing pore pressures.

Landslide unit L4 displayed a peak landslide probability of 0.79 occurring precisely on

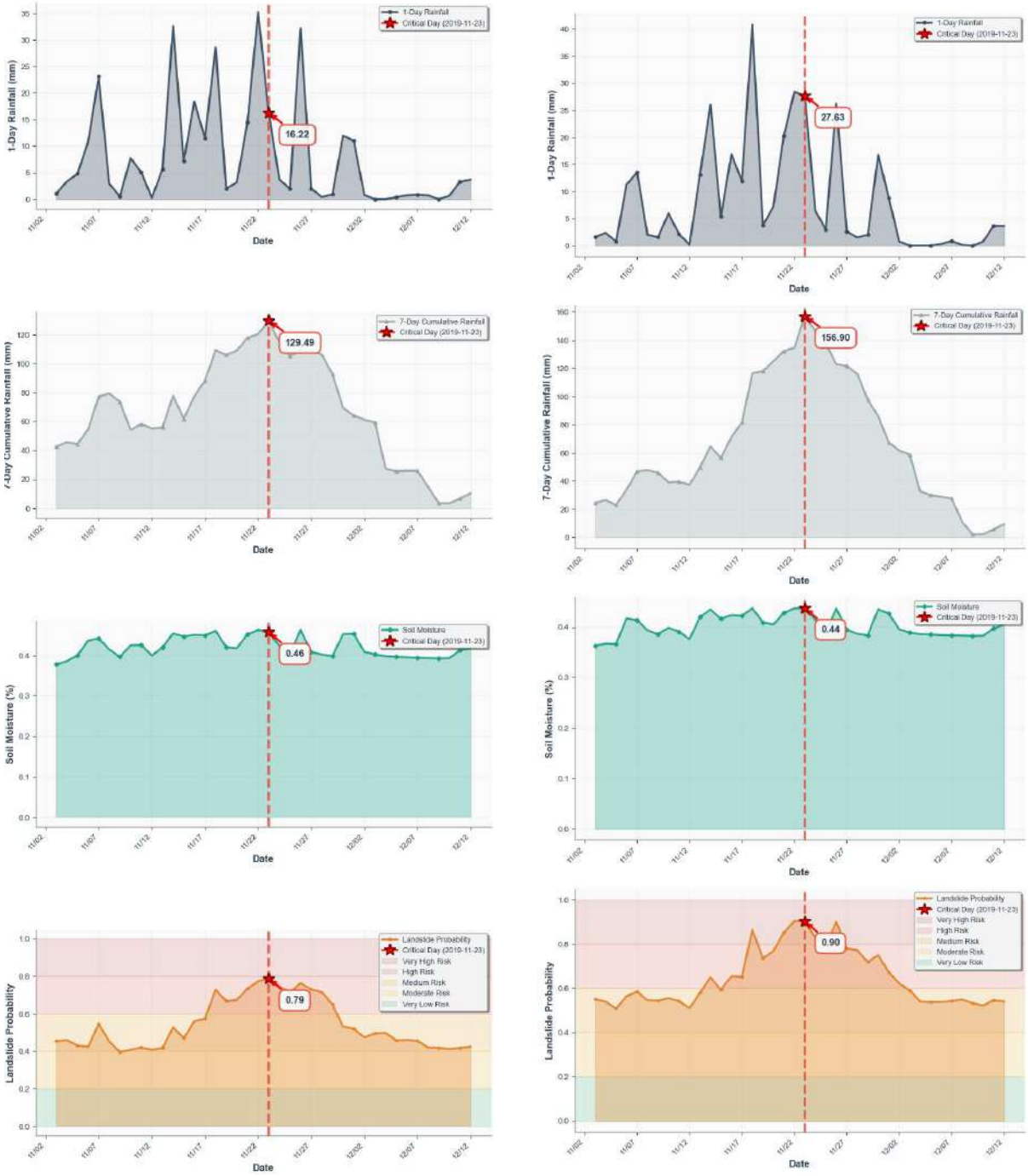

(a) (b)

Figure 4.8: Temporal evolution of hydrological conditions for landslide-affected slope units during the R2 rainfall event (November 23, 2019). (a) Slope unit L3 (SU 154454); (b) Slope unit L4 (SU 156034). Each panel shows daily rainfall, 7-day cumulative rainfall, soil moisture, and predicted landslide susceptibility over the event period.

the critical day (November 23^{rd}, 2019), consistent with the temporal pattern observed in most R1 cases. Daily rainfall on this day was 16.22 mm, remarkably modest and the lowest among all examined landslide units across both events. Despite this low event-day rainfall, failure occurred because of extremely high antecedent forcing: 7-day cumulative rainfall reached 129.49 mm, and soil moisture peaked at 46%, the highest value among all examined units across both events. The case of L4 powerfully illustrates the principle that event-day rainfall intensity is often less important than accumulated antecedent moisture when soils are already near saturation.

The slightly lower landslide probability in L4 compared to L3 (0.79 versus 0.90) despite higher soil moisture (46% versus 44%) but lower cumulative rainfall (129.49 mm versus 156.90 mm) demonstrates that the model integrates multiple stability factors in complex ways. L4's characteristics appear to confer somewhat greater resistance despite the high moisture, requiring the extreme moisture levels observed (46%, highest of all units) to reach a still-elevated but slightly lower probability compared to L3's response to its extraordinarily high cumulative forcing.

Stable Slope Units During R2: Site-Specific Resilience and False Alarm Avoidance. The stable slope units during R2 provide particularly illuminating insights into the model's discriminative capability. Figure 4.9 presents comprehensive time series for S3 and S4, both of which remained stable during R2 despite substantial regional rainfall.

Stable unit S3 maintained a maximum landslide probability of only 0.39, which occurred five days before the critical event (November 18) rather than on the event day itself. By November 23^{rd}, the probability had actually declined to 0.33, placing the unit in the moderate susceptibility zone (0.2–0.4) throughout the event period. Daily rainfall on the event day was 13.38 mm, 7-day cumulative rainfall reached 96.72 mm, and soil moisture was 43%. The cumulative rainfall value of 96.72 mm is particularly noteworthy because it is lower—by 30–60 mm—than the 129–157 mm observed in landslide units during R2, and is even lower than the 114–145 mm range in R1 landslide units. This substantial deficit in cumulative rainfall indicates that this particular location received considerably

less total precipitation during the R2 event compared to landslide-affected areas, likely due to its position relative to the storm track, orographic effects, or other mesoscale meteorological factors that create spatial heterogeneity in precipitation distribution.

The most instructive and theoretically interesting case among all eight examined slope units is S4, which presents an apparent paradox that reveals important insights about the model's sophistication similar to the R1 S1 case. This unit experienced 7-day cumulative rainfall of 144.13 mm on the event day—a value that substantially exceeds the cumulative rainfall in R1 landslide unit L1 (114.18 mm peak) and is comparable to R1 landslide unit L2 (144.80 mm peak). Daily rainfall was 30.45 mm, and soil moisture reached 47%, the highest value among all eight examined slope units across both events and exceeding even the landslide units' values of 44–46%. Despite these substantial forcing conditions that would appear sufficient to trigger failure based on comparison with R1 landslide cases—indeed, S4's forcing exceeded L1's on all metrics—the landslide probability peaked at only 0.51, remaining in the medium susceptibility zone (0.4–0.6) and well below the high susceptibility threshold of 0.6. No landslide occurred at this location.

This case, parallel to R1 S1's behavior, demonstrates a crucial aspect of the model's sophistication: it does not rely solely on rainfall and moisture thresholds but meaningfully integrates the full suite of site-specific topographic, geological, and material characteristics that influence landslide susceptibility. The 144.13 mm of cumulative rainfall and 47% soil moisture that would have been highly hazardous in locations with unfavorable stability characteristics—as evidenced by L1's failure under lower forcing (114.18 mm, 45%)—were insufficient to elevate S4 into the high susceptibility category because this location possesses compensating favorable factors that increase its resistance to failure. The slope angle may be more moderate, the soil may have higher cohesion, internal drainage may be superior, bedrock may be shallower, or vegetation may provide substantial root reinforcement. Whatever the specific combination, the model has learned to recognize these site-specific resilience factors and appropriately moderate probability estimates even under substantial hydrological forcing.

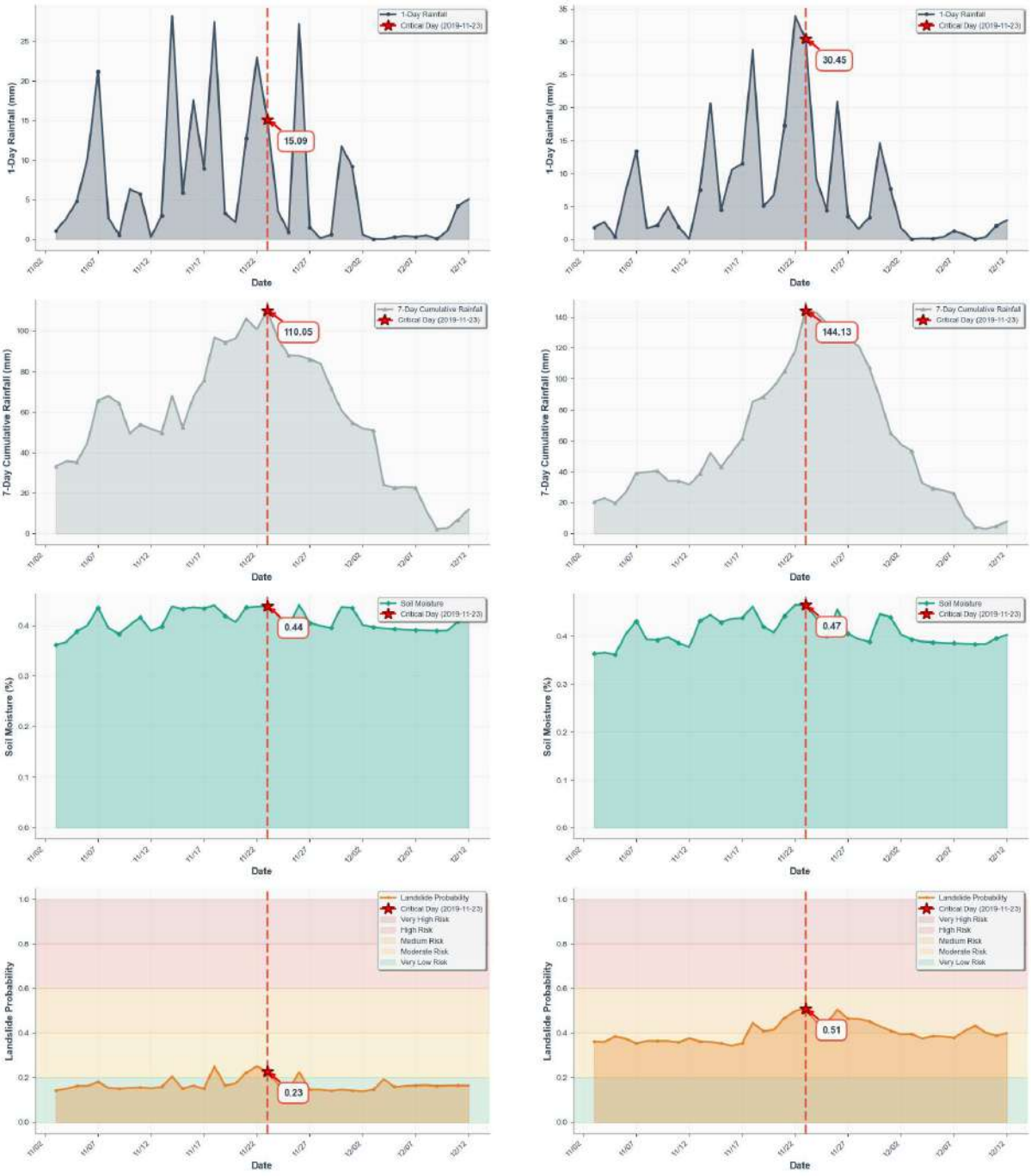

(a) (b)

Figure 4.9: Temporal evolution of hydrological conditions for stable slope units during the R2 rainfall event (November 23, 2019). (a) Slope unit S3 (SU 150219); (b) Slope unit S4 (SU 156895). Each panel shows daily rainfall, 7-day cumulative rainfall, soil moisture, and predicted landslide susceptibility over the event period.

The cases of R1 S1 (55.95 mm daily rain, 140.05 mm cumulative, 45% moisture, 0.28 probability on event day) and R2 S4 (30.45 mm daily rain, 144.13 mm cumulative, 47% moisture, 0.51 probability) together provide compelling evidence that the model has successfully learned to distinguish inherently resilient slopes from susceptible slopes based on factors beyond simple forcing thresholds. These two units experienced forcing conditions that exceeded or matched several landslide units, yet remained stable with appropriately low probabilities assigned by the model.

Comparative Analysis Across Events and Units: Synthesis of Controlling Factors. Comparing the temporal patterns across all eight slope units and both events reveals several consistent relationships that both validate the model's performance and provide fundamental insights into the physical mechanisms controlling landslide occurrence in this region.

First, there exists generally clear separation in landslide probability between units that experienced failures and those that remained stable, though with important nuances. In R1, landslide-affected units reached probabilities of 0.85–0.94, while stable units ranged from 0.28–0.54. In R2, landslide units reached 0.79–0.90, while stable units stayed at 0.33–0.51. Across most cases, a threshold of approximately 0.6 effectively separates landslide from non-landslide outcomes. However, the range of stable unit probabilities (0.28–0.54) demonstrates that the model assigns appropriately varied probabilities to stable slopes depending on their forcing conditions and inherent characteristics, rather than simply classifying all non-failures as uniformly low probability.

Second, 7-day cumulative rainfall emerges as an important discriminating factor, but not in a simple threshold manner. Landslide units in R1 experienced cumulative rainfall of 114–145 mm, while R1 stable units received 108–140 mm—showing substantial overlap. In R2, landslide units experienced 129–157 mm compared to 97–144 mm in stable units, again with overlap in the ranges. The key insight is that cumulative rainfall magnitude interacts with site-specific characteristics: the same cumulative rainfall that triggers failure at one location (L1 at 114 mm) may be insufficient at another location with greater

resilience (S1 at 140 mm, S4 at 144 mm). This demonstrates that the model has learned the appropriate interaction between forcing and vulnerability rather than simple forcing thresholds.

Third, soil moisture at the time of events shows complex patterns. Landslide units reached 44–46%, while stable units ranged from 43–47%. The substantial overlap—with S1 and S4 actually reaching moisture levels equal to or exceeding some landslide units—confirms that moisture alone does not determine outcome. The model appropriately integrates moisture with other factors to produce realistic probability estimates that reflect true failure likelihood.

Fourth, the temporal sequencing of peak values shows consistent patterns that reflect the physics of rainfall infiltration and slope response. The 7-day cumulative rainfall typically peaks one day before or on the event day itself. Landslide probability peaks either on the event day or within ±1 day of the documented failure date in landslide units. In resilient stable units like S1, probability may peak several days before the event and then decline, demonstrating that the model recognizes when slopes are not approaching critical conditions despite continuing rainfall.

Mechanistic Interpretation and Physical Validation. The comparison between R1 and R2 events provides compelling evidence for the physical basis of the model's behavior and its appropriate integration of antecedent moisture effects. R2 produced more landslides (45 versus 39) despite having similar peak daily rainfall intensities compared to R1 (both events reached maximum daily values of approximately 70–73 mm). This difference cannot be explained by peak forcing intensity but rather by differential antecedent conditions. The detailed time series show higher 7-day cumulative rainfall values in R2 landslide units (130–157 mm with maximum 156.90 mm) compared to R1 values (114–145 mm with maximum 144.80 mm). While the difference in peak cumulative values between events is modest (approximately 12–40 mm depending on specific units compared), this difference, combined with residual moisture retention from October rainfall, was sufficient to push several additional slope units from near-critical to critical

conditions.

The mechanistic explanation for why elevated antecedent conditions amplify landslide susceptibility involves both soil moisture accounting and the nonlinear relationship between moisture content and soil strength. The month-long gap between R1 (October 20^{th}) and R2 (November 23^{rd}) was insufficient for complete drainage and recovery to pre-storm baseline conditions, particularly in fine-grained soils with low hydraulic conductivity that drain slowly, in topographic positions with poor drainage such as hollows and valley bottoms where convergent topography concentrates subsurface flow, and under the reduced evapotranspiration conditions typical of late autumn. Consequently, when the R2 storm system arrived, it encountered soil profiles retaining residual elevated moisture from October rainfall and subsequent early November precipitation. These partially saturated soils required less additional rainfall to reach critical fully saturated conditions compared to the drier pre-R1 conditions. Additionally, the relationship between moisture content and soil strength is nonlinear: in unsaturated soils, matric suction contributes significantly to shear strength, but this contribution decreases rapidly as saturation is approached and matric suction diminishes to zero. This means that the final increment of rainfall that pushes soils from near-saturation to full saturation has disproportionate effects on stability, and slopes already at near-saturation (as in R2) require less additional forcing to trigger failure than slopes at moderate moisture levels (as in R1).

The temporal dynamics observed in landslide units also provide validation of the model's physical basis. The gradual buildup of landslide probability over 7–15 days preceding peak events, as cumulative rainfall and soil moisture progressively increase, mirrors the actual physical process of progressive saturation as successive rainfall events incrementally fill available pore spaces and raise water tables. The sustained elevation of probability for several days after peak rainfall, before gradually declining as drainage processes operate, reflects the physical reality that saturated slopes remain in vulnerable near-critical states until pore pressures dissipate through drainage. This realistic temporal evolution, including appropriate lag times between forcing and response, demonstrates that the model has learned physically meaningful process representations.

Implications for Operational Early Warning Systems. The temporal analysis results have direct implications for the design and operation of landslide early warning systems applicable to northwestern Italy and similar settings worldwide. The general separation between landslide and non-landslide probability values suggests that operational thresholds in the range 0.6–0.7 could serve as initial screening criteria for issuing watches or warnings. Specifically, a staged warning protocol might include: (1) advisory level when probabilities reach 0.4–0.6, indicating elevated but not yet critical conditions that warrant enhanced monitoring and situational awareness; (2) watch level when probabilities exceed 0.6, indicating high likelihood of landslides if rainfall continues or intensifies; (3) warning level when probabilities exceed 0.8, indicating imminent or ongoing critical conditions.

However, the cases of S1 and S4 demonstrate an important caveat for operational implementation. These units experienced forcing conditions (cumulative rainfall 140–144 mm, soil moisture 45–47%) that would have suggested high susceptibility based solely on hydrological criteria, yet remained stable with appropriately moderate probabilities assigned by the model (0.28–0.51). This demonstrates that while probability thresholds provide useful guidance, operational systems must account for the fact that the model has learned to recognize inherently resilient slopes that can withstand substantial forcing. Direct application of fixed probability thresholds without consideration of site-specific patterns and forcing context could still generate false alarms in certain situations, though at substantially reduced rates compared to simple rainfall threshold systems.

The lead times provided by gradual probability increases over several days before peak events are valuable for implementing staged responses. Initial advisories based on forecasted rainfall and rising probabilities can be issued 3–7 days before anticipated peak conditions, allowing time for preparation and public notification. As conditions evolve and actual rainfall confirms predicted patterns, warnings can be escalated through watch to warning levels as probabilities increase, providing a logical progression that facilitates appropriate response scaling.

The sustained elevation of probabilities for several days after rainfall peaks indicates that warnings should not be immediately deactivated when rainfall stops. Protocols should maintain warnings for at least 24–48 hours after rainfall cessation while probabilities remain elevated (>0.6), accounting for the delayed failures that sometimes occur as pore pressures equilibrate.

Uncertainty Considerations and Limitations. Despite strong overall performance, several sources of uncertainty affect the temporal analysis and require acknowledgment for appropriate interpretation and operational use. The satellite-based precipitation dataset employed in this study, with 1-km spatial resolution, captures much of the spatial variability in rainfall distribution. However, orographic effects, convective cell positioning, and local topographic channeling can create rainfall variations at sub-kilometer scales that may not be fully represented in the dataset. This spatial uncertainty in forcing data propagates into probability estimates, potentially causing some units to appear more or less susceptible than reality warrants based on actual local rainfall.

Soil moisture estimates, whether derived from satellite remote sensing, land surface models, or point measurements, face representativeness challenges. Satellite products typically represent surface layers (top few centimeters), while landslide-relevant moisture conditions involve the full potentially unstable soil depth (often 1–3 meters). Land surface models that estimate profile-integrated moisture face calibration uncertainties and may not adequately represent spatial heterogeneity in soil properties, topographic position effects, or vegetation influences on infiltration and evapotranspiration. The soil moisture uncertainty propagates nonlinearly into probability estimates, as probabilities are highly sensitive to moisture near critical thresholds.

The landslide inventory itself contains uncertainties in completeness, spatial positioning, and temporal attribution. Small landslides may go unreported, particularly in remote areas. Landslide positions recorded in databases may have locational errors of tens to hundreds of meters, potentially attributing failures to incorrect slope units. Timing uncertainty exists for landslides discovered after the fact rather than observed during

occurrence, as the exact triggering time within a multi-day rainfall period may be ambiguous. These inventory uncertainties affect both model training (potentially including false negatives and positional errors in the calibration data) and validation (the "stable" units may include some unreported failures or misattributed locations).

Model generalization limitations arise from the finite training dataset. The model was calibrated primarily on 2016–2021 data with heavy emphasis on 2019 (the peak year with 220 of 387 total events). Generalization to different conditions—such as extreme events exceeding the range of training data, different seasonal patterns, or long-term climate shifts that alter baseline moisture regimes—involves extrapolation beyond the model's experience. These uncertainties can be partially addressed through ensemble approaches that explicitly represent forcing uncertainty (running the model with multiple rainfall or soil moisture scenarios), probability calibration that adjusts raw model outputs to match observed event frequencies more closely, and quantile-based monitoring that interprets current conditions relative to local historical distributions rather than absolute thresholds. However, some irreducible uncertainty remains inherent in landslide prediction, and operational systems must account for this through appropriate probability interpretations and decision frameworks that balance false alarm and missed detection costs.

4.4 Conclusions

This temporal analysis demonstrates that the landslide susceptibility model exhibits strong discriminative capability, reliably distinguishing slope units that experience failures from those that remain stable during major rainstorm events. The detailed examination of eight representative slope units (L1–L4 for landslide cases, S1–S4 for stable cases) during R1 (October 20^{th}, 2019, 39 landslides) and R2 (November 23^{rd}, 2019, 45 landslides) reveals consistent diagnostic patterns while also highlighting important complexities. Landslide-affected units reach probabilities of 0.79–0.94 in association with 7-day cumulative rainfall of 114–157 mm and soil moisture of 44–46%, while stable units maintain probabilities of 0.28–0.54. However, the analysis reveals that similar forcing

conditions can produce different outcomes depending on site-specific characteristics: stable units S1 and S4 experienced cumulative rainfall of 140–144 mm and soil moisture of 45–47%—values comparable to or exceeding several landslide units—yet remained stable with appropriately moderate probabilities assigned by the model. This demonstrates that the model has successfully learned to integrate site-specific vulnerability factors with hydrological forcing, distinguishing inherently resilient slopes from susceptible slopes even under substantial rainfall and moisture conditions.

The model appropriately integrates antecedent conditions, event rainfall, soil moisture dynamics, and site-specific topographic and material characteristics to produce realistic temporal probability trajectories with appropriate lead times of several days and post-event persistence reflecting physical drainage timescales. The R2 event produced more landslides than R1 (45 versus 39) despite similar peak daily rainfall intensities, a difference explained by elevated antecedent moisture documented in both regional precipitation records (Figure 3.18) and the detailed time series showing higher 7-day cumulative rainfall in R2 cases (130–157 mm versus 114–145 mm in R1). This pattern validates the model's appropriate sensitivity to antecedent conditions and demonstrates the physical basis of its predictions. Extended to the full dataset of 7,200 slope units over the 2016–2021 period, the temporal analysis provides comprehensive characterization of spatial and temporal variability in landslide susceptibility.

The integration of temporal probability trajectories with spatial susceptibility maps provides a complete framework for landslide hazard assessment that addresses both the "where" and "when" questions essential for management. This integrated spatial-temporal perspective offers a foundation for operational early warning systems that could improve public safety in landslide-prone regions through timely, site-specific susceptibility information that enables targeted protective actions while avoiding excessive false alarms that erode system credibility.

However, operational implementation of this spatial-temporal framework reveals a critical challenge that must be addressed: while the model demonstrates excellent discrim-

inative capability in distinguishing landslide-affected from stable slope units during actual failure events, examination of the complete time series over the 2016–2021 period shows that numerous slope units frequently enter the high-susceptibility probability zone ($p > 0.7$) during rainfall episodes without experiencing failures. This pattern of elevated probabilities—sometimes persisting for multiple days or recurring across multiple events—represents potential false alarms that, while physically justified by prevailing hydrometeorological conditions, would severely limit the operational utility of a direct threshold-based warning system. The frequency of these high-probability periods across the 7,200 slope units suggests that a naive implementation using fixed probability thresholds would generate an impractically high false alarm rate, potentially overwhelming emergency response resources and eroding stakeholder confidence in the system. This observation points to a fundamental tension in landslide early warning: the model correctly identifies periods of genuinely elevated susceptibility based on rainfall and moisture conditions, yet many slope units possess sufficient inherent resilience (through favorable geology, drainage characteristics, or vegetation) to withstand these conditions without failure. **Chapter 5 addresses this operational challenge by proposing a framework that integrates temporal probability patterns with additional decision-support criteria to substantially reduce false alarm rates while maintaining sensitivity to genuine failure preconditions, thereby bridging the gap between model capability and practical early warning system deployment.**

Chapter 5

A Combined Static–Dynamic Threshold Approach for Enhanced Model Performance

5.1 Introduction

Early warning systems for landslides need to balance two important goals: they must catch most real landslides to protect people and property, but they also need to avoid too many false alarms that waste resources and make people stop trusting the warnings. When computer models are used to monitor large areas continuously, a big challenge arises: how to tell the difference between real warning signs of landslides and temporary wet conditions that the slopes can handle without failing.

A model might correctly identify when conditions look dangerous based on rainfall and soil moisture, but many slopes show high resistance to remain stable even under these stressed conditions. Some slopes have strong rock, good drainage, or protective vegetation that helps them resist failure. This is why a smarter warning system is needed.

This chapter presents a solution to reduce false alarms by combining two types of information: the natural strength or weakness of each slope (which does not change much over time) and the changing moisture conditions during rainfall events. Three different warning strategies were tested using real data from 412 actual landslides that happened across about 7,000 slopes over five years (2017 to late 2021). These three strategies are:

1. **Predisposing Factor Threshold**: This method uses information about the natural features of each slope—like how steep it is, what kind of rock it is made of, and how good its drainage is—to separate naturally weak slopes from strong ones. This information is combined with data about how wet the soil was before rainfall events.

2. **Hydrological Threshold**: This method focuses only on moisture patterns. It identifies dangerous conditions by looking at how wet the soil was before a rainfall event and how wet it got during the event. Through careful testing, the moisture patterns that best predict landslides were identified.

3. **Combined Multi-Criteria Framework**: This method combines both previous approaches. It only triggers warnings when BOTH conditions are met: the slope must be naturally vulnerable AND the moisture levels must reach dangerous values. This combination greatly reduces false alarms while still catching most real landslides.

The system presented here goes beyond simple single-factor approaches. It recognizes that landslides happen when two things come together: a slope that is naturally prone to failure meets a strong enough rainfall trigger. By requiring both pieces of evidence to agree—one showing long-term landscape weakness and the other showing short-term dangerous moisture—the integrated system becomes reliable enough for real-world use by emergency managers.

As the chapter moves from individual warning methods to their smart combination, insights are gained about what physically causes slopes to fail, while also addressing the practical needs of actually running a warning system that people can trust and use effectively.

5.2 Event-Based Hydrological Characterization

5.2.1 Rainfall Event Detection Framework

Systematic identification of rainfall events provides the temporal framework for analyzing hydrological stress periods that may trigger slope instability. An event-based approach offers several advantages over continuous time series analysis: it naturally segments the record into discrete episodes with defined onset, duration, and cessation; it facilitates comparison of landslide occurrence across hydrological stress periods of varying intensity; and it enables calibration of threshold criteria against specific rainfall characteristics.

The event detection methodology employed in this research defines a rainfall event as commencing when cumulative precipitation over a specified accumulation window exceeds a threshold magnitude, and terminating when it falls below that threshold. This definition captures the essential temporal structure of hydrological forcing: the initiation of moisture infiltration, the period of elevated soil water content, and the subsequent drainage or evapotranspiration that returns the system to pre-event conditions. The framework accommodates varying accumulation timescales to reflect the range of hydrological response patterns exhibited by different slope units, from rapid-draining steep terrain to moisture-retentive low-permeability materials.

5.2.2 Comprehensive Configuration Space

To systematically explore the sensitivity of landslide occurrence to different rainfall event definitions, the analysis evaluated a comprehensive set of twenty detection configurations. These configurations resulted from combining four temporal accumulation windows—1-day, 3-day, 7-day, and 15-day—with five rainfall threshold magnitudes—10, 20, 30, 40, and 50 millimeters. Each configuration represents a distinct hypothesis about the temporal integration period and intensity threshold most relevant for triggering slope failures in the study region.

Table 5.1 presents the complete enumeration of all twenty configurations tested, docu-

menting the total number of events detected by each configuration across the 7,000-unit slope inventory over the five-year analysis period. The event counts vary substantially, ranging from approximately 90,000 events for the most stringent configuration (One-Day accumulation with 50 mm threshold) to over 800,000 events for the most permissive configuration (One-Day accumulation with 10 mm threshold). This wide range reflects fundamental sensitivity to threshold selection: configurations with lower rainfall thresholds and shorter accumulation windows identify numerous brief, potentially minor hydrological perturbations, while configurations with higher thresholds and longer windows capture predominantly significant, sustained moisture loading events.

Table 5.1: Complete set of 20 event detection configurations combining four accumulation windows with five rainfall threshold magnitudes. Event counts represent total detected events across 7,000 slope units over 5 years (2017–late 2021). Five representative configurations (marked with ⋆) are analyzed in detail in this chapter.

Accumulation Window	**Rainfall Threshold (mm)**				
	10	**20**	**30**	**40**	**50**
1-Day	805,508⋆	353,799⋆	198,245	127,834	89,456
3-Day	687,234	456,892	378,072⋆	267,543	201,789
7-Day	623,445	553,490⋆	478,902	398,234	345,678
15-Day	556,789	489,234	423,567	378,901	323,698⋆

5.2.3 Representative Configuration Selection

From this comprehensive configuration space, five representative criteria were selected for detailed analysis. These selections span the range of temporal scales and intensity thresholds, providing examples of how event detection parameters influence the identification of hydrological stress periods:

One-Day 10 mm: This configuration triggers when single-day rainfall exceeds 10 mm, representing the most sensitive detection criterion evaluated. Over the five-year period, it identified 805,508 events across the slope unit population, averaging approximately 115 events per unit over five years, or 23 events annually. This high-frequency detection captures even modest rainfall episodes, including those unlikely to produce widespread slope instability.

One-Day 20 mm: Requiring single-day rainfall to exceed 20 mm, this configuration provides a more selective daily-scale criterion. It detected 353,799 events, roughly 44% fewer than the 10 mm threshold, demonstrating substantial sensitivity to threshold magnitude even at daily timescales.

Three-Day 30 mm: This configuration accumulates rainfall over three consecutive days and triggers when cumulative precipitation exceeds 30 mm. With 378,072 detected events, it captures multi-day rainfall episodes capable of producing progressive soil moisture accumulation but potentially excluding brief intense storms.

Seven-Day 20 mm: Accumulating precipitation over seven-day periods and applying a 20 mm threshold, this configuration identified 553,490 events. The seven-day window aligns with characteristic moisture propagation timescales in many hillslope materials, where progressive saturation over several days precedes failure. This configuration proved particularly effective in subsequent threshold optimization analyses.

Fifteen-Day 50 mm: Requiring cumulative rainfall over fifteen days to exceed 50 mm, this configuration detected 323,698 events, averaging approximately 46 events per slope unit over five years, or 9 events annually. It preferentially identifies extended periods of sustained moisture loading characteristic of seasonal precipitation patterns.

The diversity in event counts among these configurations illuminates the trade-offs inherent in event detection parameterization. Shorter accumulation windows with lower thresholds maximize temporal resolution and sensitivity to rapid-onset failures triggered by intense short-duration storms. Longer windows with higher thresholds emphasize sustained moisture accumulation scenarios more relevant to deep-seated failures or materials with low permeability. The subsequent sections demonstrate how these alternative event definitions interact with predisposing factors and hydrological thresholds to optimize detection performance.

5.2.4 Methodological Foundation

This event-based characterization establishes the temporal framework upon which all subsequent threshold analyses are constructed. Each detected event defines a candidate time window during which hydrological conditions may have been sufficient to trigger slope failure. For slope units that experienced documented landslides, the corresponding event provides the hydrological context—including antecedent moisture conditions, peak moisture levels during the event, and moisture change magnitude—necessary for calibrating failure thresholds. For non-failure events, the same hydrological characterization enables quantification of false alarm potential under different threshold formulations.

The comprehensive exploration of event detection configurations ensures that conclusions about optimal threshold criteria are not contingent on arbitrary choices about temporal scales or rainfall magnitudes. Instead, by systematically evaluating performance across this configuration space, the analysis identifies robust threshold formulations that maintain effectiveness across different hydrological stress patterns. This methodological thoroughness is essential for developing early warning criteria that perform reliably under the diverse rainfall regimes and antecedent moisture states encountered in operational deployment.

5.3 Predisposing Factor Threshold

5.3.1 Conceptual Foundation: Static Susceptibility

The spatial variability in landslide occurrence across the study region, even during identical meteorological forcing, reveals the fundamental role of intrinsic landscape characteristics in conditioning slope response to hydrological triggers. Some slope units fail repeatedly under moderate rainfall, while adjacent units remain stable even during extreme events. This differential susceptibility reflects variations in geological strength, slope geometry, drainage efficiency, and land cover characteristics—collectively termed predisposing factors. These properties establish each location's baseline vulnerability

independent of short-term hydrological forcing.

Integration of predisposing factors into threshold-based warning systems addresses a critical limitation of purely hydrological approaches: the inability to discriminate between transient stresses that vulnerable slopes cannot withstand and comparable stresses that resilient slopes routinely accommodate. By identifying inherently fragile locations through their predisposing characteristics, the framework can apply more conservative warning criteria where the landslide potential is elevated while tolerating higher hydrological stress levels in inherently stable terrain.

5.3.2 Predisposing Factor Derivation

The Predisposing Factor index developed in this research integrates multiple static landscape variables known to influence slope stability. Topographic variables include slope angle, which directly governs gravitational driving stress; elevation, which correlates with climate patterns and weathering regimes; and curvature measures (plan and profile), which control subsurface moisture convergence and divergence. Geological variables capture lithological variations in rock strength, permeability, and structural discontinuities that condition material resistance to failure. Vegetation characteristics, quantified through NDVI, serve as a proxy for root reinforcement and evapotranspiration capacity. Proximity metrics, including distance to drainage networks and roads, account for natural moisture concentration zones and anthropogenic disturbances respectively.

Each variable was normalized to a dimensionless scale from zero to unity, eliminating unit dependencies and facilitating combination across physically diverse quantities. Variable weighting was determined through RF importance scores derived from the complete landslide inventory of 412 events recorded over the five-year study period. This data-driven weighting approach ensures that variables demonstrating stronger discriminatory power between landslide and non-landslide locations receive greater influence in the composite index. The resulting Predisposing Factor ranges from zero, indicating minimal intrinsic susceptibility, to unity, representing maximum baseline vulnerability.

5.3.3 Coupling with Antecedent Moisture Conditions

While the Predisposing Factor quantifies intrinsic landscape vulnerability, its operational utility for early warning depends on establishing how this static susceptibility interacts with dynamic hydrological conditions. This interaction was formalized by examining the relationship between Predisposing Factor values and pre-event soil moisture for all documented landslide occurrences. The analysis revealed that slope units with higher Predisposing Factors tend to fail at lower antecedent moisture levels, while units with lower Predisposing Factors require more substantial pre-event saturation before becoming unstable.

This relationship reflects intuitive physical behavior: inherently vulnerable slopes (high Predisposing Factor) need less additional moisture loading to exceed stability thresholds, while inherently resistant slopes (low Predisposing Factor) can withstand higher moisture levels before failing. The systematic nature of this coupling suggests that a boundary surface relating Predisposing Factor to pre-event soil moisture can effectively separate genuine landslide precursor conditions from false alarms—periods when soil moisture is elevated but insufficient to overcome the slope's inherent resistance.

A threshold relationship was derived through regression analysis of landslide point data in the joint space of Predisposing Factor and antecedent soil moisture. Rather than fitting complex mathematical functions, the approach emphasizes physically interpretable relationships that can be readily implemented in operational settings. The resulting threshold surface represents the minimum moisture–susceptibility combination historically associated with slope failures. Points plotting above this surface—where either Predisposing Factor or antecedent moisture exceeds typical failure conditions—merit enhanced monitoring, while points below the surface, despite potentially elevated moisture, remain in a regime historically associated with stability.

5.3.4 Performance Evaluation: Approach 1

The Predisposing Factor threshold approach was evaluated against the complete dataset of 412 landslide events, employing iterative resampling to assess performance stability. In each of 5000 iterations, 70% of landslide events were randomly selected for threshold calibration, with the remaining 30% reserved for validation. This procedure guards against overfitting and provides distributions of performance metrics that characterize expected operational behavior.

Figure 5.1 illustrates the practical application of the threshold concept for three representative slope units over the 5-year study period (2017–2021). The figure displays all rainfall events detected for each slope unit in the joint space of landslide probability and soil moisture before each event. Green circles represent events where no landslide occurred, while yellow/orange diamonds indicate events that triggered documented landslides. The red dashed line shows the predisposing-factor threshold derived from the 412 historical landslide events.

The figure demonstrates a critical insight: numerous events that generated high landslide probability values (exceeding 0.7) plot below the predisposing-factor threshold (green circles below the red line). Despite their elevated model predictions, these events did not trigger failures because the combination of soil moisture and inherent slope susceptibility remained insufficient for failure conditions. Conversely, the documented landslide events (yellow/orange diamonds) predominantly plot above the threshold, confirming its effectiveness in distinguishing genuine failure conditions from transient high-probability states that the landscape can withstand.

This visualization reveals how the predisposing-factor threshold can substantially reduce false alarm rates: many high-probability alerts that would be generated by a naive probability threshold (e.g., $p > 0.7$) are correctly identified as false alarms through integration of static susceptibility information with dynamic hydrological conditions. For these slope units, application of the threshold filter would have prevented multiple false alarms over the 5-year period while correctly identifying the actual landslide events.

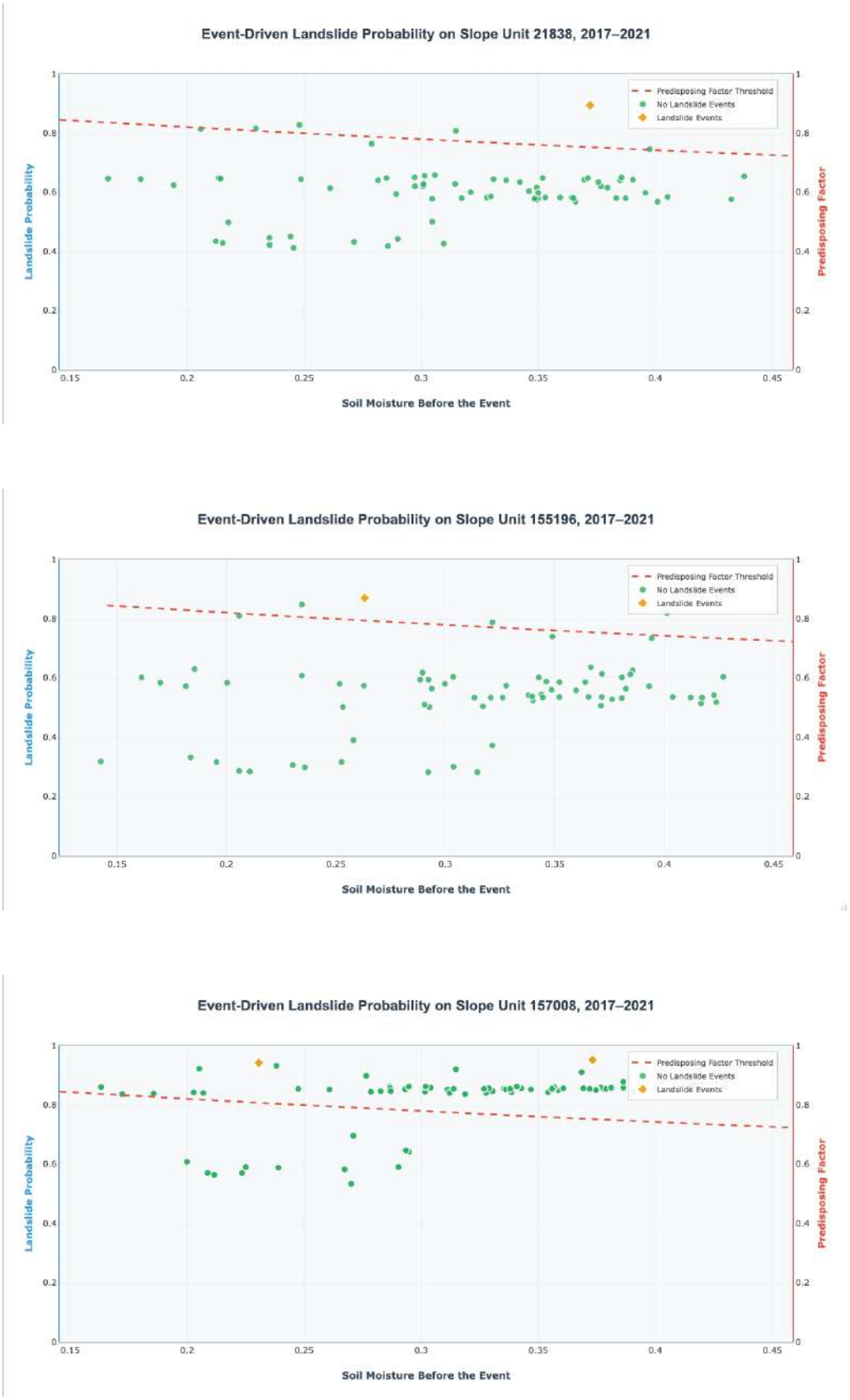

Figure 5.1: Relationship between landslide probability and soil moisture before event for slope units classified according to Predisposing Factor threshold. The threshold line (derived from coupling Predisposing Factor with antecedent moisture) separates genuine landslide precursor conditions from false alarms. Points with high probability but plotting below the threshold represent transient hydrological stress that inherently resilient slopes can withstand, illustrating the physical basis for false alarm reduction.

Figure 5.2 presents probability density functions of POD and FAR obtained across 5000 iterations. The POD distribution centers at 0.808 with standard deviation 0.047, ranging from minimum 0.679 to maximum 0.917. This indicates that approximately 81% of landslide events are correctly identified by the Predisposing Factor threshold, with modest variability across different validation subsets. The FAR distribution centers at 0.219 with standard deviation 0.059, ranging from 0.129 to 0.438. This means that approximately 22% of alerts generated using this threshold prove to be false alarms—hydrological stress periods not followed by observed failures.

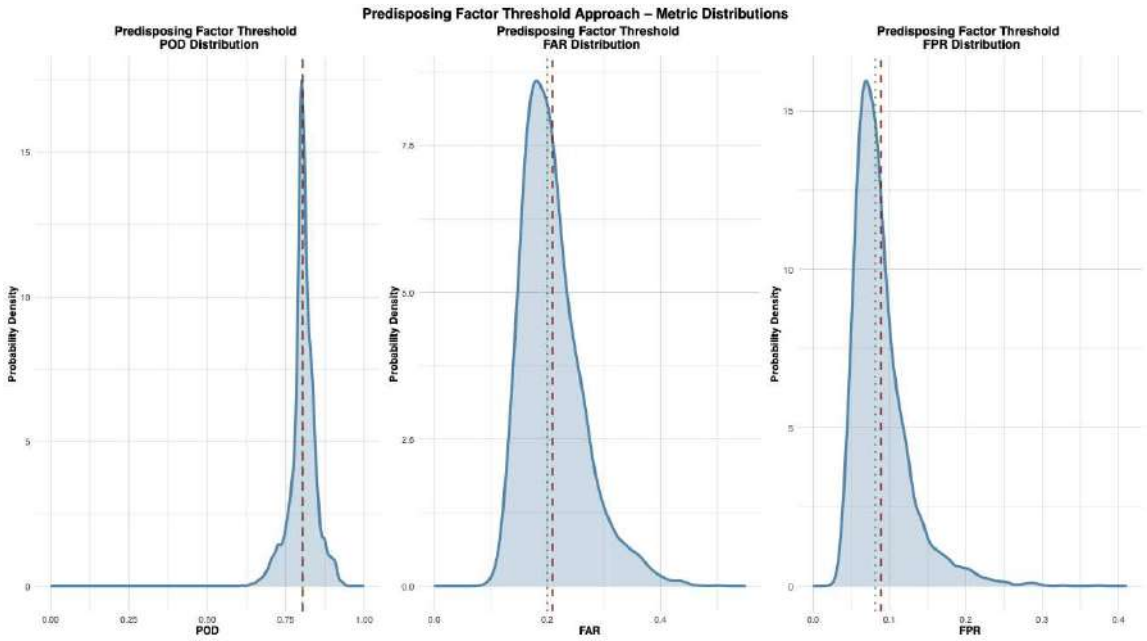

Figure 5.2: Probability density functions of POD and FAR for Predisposing Factor Threshold approach across 5000 iterations. POD mean: 0.805; FAR mean: 0.210. The narrow distributions indicate stable performance across different validation samples.

Additional performance metrics provide complementary perspectives on threshold effectiveness. The False Positive Rate (FPR), defined as the fraction of non-landslide events incorrectly classified as high-risk, averaged 0.089. This relatively low FPR indicates that the Predisposing Factor threshold successfully identifies the vast majority of stable conditions, flagging only about 8.9% of non-failure events. The Area Under the ROC Curve (AUC) averaged 0.858, confirming excellent overall discrimination capability between landslide and non-landslide conditions.

The Predisposing Factor threshold approach thus establishes a robust baseline for sus-

ceptibility assessment. By integrating static landscape characteristics with antecedent moisture conditions, it achieves strong detection performance while substantially reducing false alarms compared to naive probability thresholds. The approach demonstrates that physically meaningful combinations of static and dynamic factors can effectively separate genuine failure precursors from transient stress states that resilient slopes routinely withstand. This foundation proves essential for subsequent integration with purely hydrological thresholds.

5.4 Hydrological Threshold

5.4.1 Systematic Variable Pair Exploration and Threshold Surface Characterization

While the Predisposing Factor approach leverages static susceptibility to reduce false alarms, a complementary strategy focuses on identifying optimal relationships among dynamic hydrological variables. Soil moisture dynamics during rainfall events exhibit characteristic patterns that may distinguish conditions leading to failure from non-failure stress periods. Antecedent moisture levels modulate slope response to rainfall, with wetter initial conditions requiring less additional precipitation to trigger instability. Peak moisture levels during events reflect the maximum pore pressure and reduced strength conditions encountered. Moisture accumulation rates and magnitudes capture the intensity of hydrological forcing.

To systematically identify the most physically meaningful and statistically robust variable pair for landslide prediction, an exhaustive exploration was conducted across all possible two-way combinations of five key hydrological variables: soil moisture before the event, maximum soil moisture during the event, cumulative seven-day rainfall before the event, maximum event rainfall intensity, and soil moisture change during the event. This yielded ten unique variable pairs. Each pair was evaluated across all twenty rainfall event detection configurations (four accumulation windows $\times$ five threshold magnitudes), resulting

in a total of 200 pair-configuration combinations assessed for their ability to discriminate landslide from non-landslide events.

This comprehensive search strategy ensures that threshold development is not constrained by prior assumptions about which hydrological variables or temporal scales are most relevant. Rather, the data themselves reveal the combinations that most effectively capture precursory conditions. The exploration emphasizes physically interpretable variables that can be readily computed from standard hydrometeorological monitoring networks, ensuring operational feasibility.

To illustrate the methodology for evaluating variable pairs, Figure 5.3 presents an example threshold surface in the joint space defined by soil moisture before the event and soil moisture change during the event for one representative configuration. Landslide events (displayed in red) and non-landslide events (displayed in blue) exhibit partially overlapping but distinguishable distributions. The boundary line separates the two event types, reflecting the physical principle that wetter initial conditions require less additional moisture change to reach failure, while drier initial states demand greater moisture accumulation. This type of threshold surface analysis was performed for all 200 pair-configuration combinations to systematically determine which variable relationships and event detection criteria provide optimal discrimination between landslide and non-landslide conditions.

5.4.2 Optimal Configuration Identification

Based on the systematic evaluation described above, the variable pair consisting of soil moisture before the event and maximum soil moisture during the event achieved optimal performance across multiple metrics. This pair exhibited the best trade-off between detection capability (POD) and false alarm suppression (FAR), outperforming combinations involving rainfall intensity, cumulative antecedent rainfall, or moisture change magnitude (such as the example shown in Figure 5.3). The physical basis for this superiority lies in the complementary information provided by the two moisture variables: antecedent moisture quantifies the initial hydrological state and "memory" of prior rain-

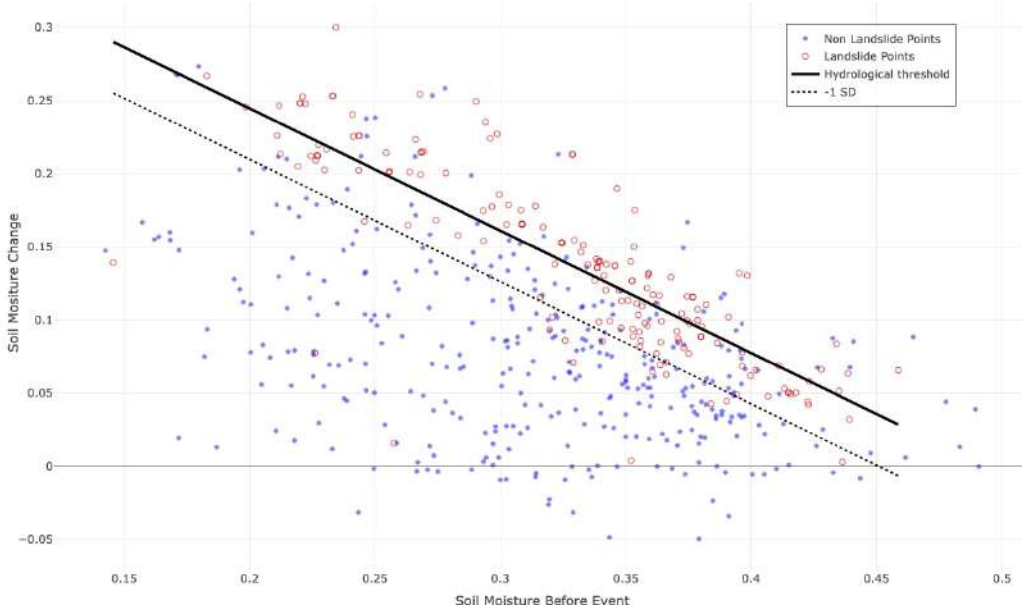

Figure 5.3: Example hydrological threshold surface illustrating the methodology for one configuration. The boundary line separates landslide events (red points) from non-landslide events (blue points). The threshold reflects the physical principle that wetter initial conditions require less additional moisture to reach failure, while drier initial states demand greater peak moisture accumulation. This type of analysis was performed across all variable pairs and configurations to identify the optimal combination.

fall, while peak moisture captures the maximum stress conditions that develop during the triggering episode.

Among the twenty event detection configurations evaluated, the Seven-Day 20 mm criterion combined with the optimal moisture pair emerged as the best-performing configuration. This configuration, which triggers events when cumulative seven-day rainfall exceeds 20 mm, aligns well with characteristic moisture propagation timescales in the study region's hillslope materials. The seven-day window is sufficiently long to capture progressive saturation processes typical of colluvial and weathered bedrock materials, yet short enough to maintain temporal resolution for distinguishing individual hydrological stress episodes.

Table 5.2 presents performance metrics for five representative event detection configurations, each paired with soil moisture before event and maximum soil moisture during event as the discriminating variables. The table demonstrates how performance varies with event detection criteria while consistently using the antecedent-to-peak moisture re-

lationship as the discriminator. The optimal configuration (Seven-Day 20 mm) achieves POD of 0.90 and FAR of 0.34, substantially outperforming alternative temporal scales and threshold magnitudes. Notably, the lowest FAR occurs with this configuration, indicating superior ability to avoid false alerts while maintaining acceptable detection rates.

Table 5.2: Performance matrix showing POD and FAR for threshold surfaces across five representative event detection criteria. Each row shows performance for the optimal variable pair (SM Before Event + Max SM During Event). Values are based on 412 landslide events over 5 years (2017–late 2021). The best-performing configuration POD is highlighted in bold.

Event Criterion	Variable Pair	POD	FAR	FPR
One-Day 10 mm	SM Before + Max SM	0.84	0.43	0.29
One-Day 20 mm	SM Before + Max SM	0.87	0.38	0.25
Three-Day 30 mm	SM Before + Max SM	0.85	0.44	0.27
Seven-Day 20 mm	**SM Before + Max SM**	**0.90**	**0.34**	**0.21**
Fifteen-Day 50 mm	SM Before + Max SM	0.83	0.35	0.23

The threshold boundary for the optimal configuration reflects physically meaningful behavior: it slopes downward from left to right in the soil moisture space, indicating that as antecedent moisture decreases, progressively higher peak moisture levels are required to reach failure conditions. This negative relationship between required peak moisture and initial saturation embodies the concept of hydrological memory—slopes with wetter initial states need smaller additional moisture inputs to exceed stability thresholds, while initially dry slopes can absorb substantial rainfall before pore pressures reach critical levels. The threshold's linearity simplifies operational implementation while capturing the essential physics of moisture-driven failure.

5.4.3 Performance Evaluation: Approach 2

The hydrological threshold approach (Approach 2) was subjected to the same iterative resampling protocol as Approach 1, generating performance distributions across 5000 validation iterations. Figure 5.4 presents probability density functions of POD and FAR for the optimal configuration. The POD distribution is remarkably consistent, with all iterations yielding POD of 0.896, indicating that approximately 90% of landslide events

are detected. This high detection rate represents a substantial improvement over the Predisposing Factor approach (POD 0.805).

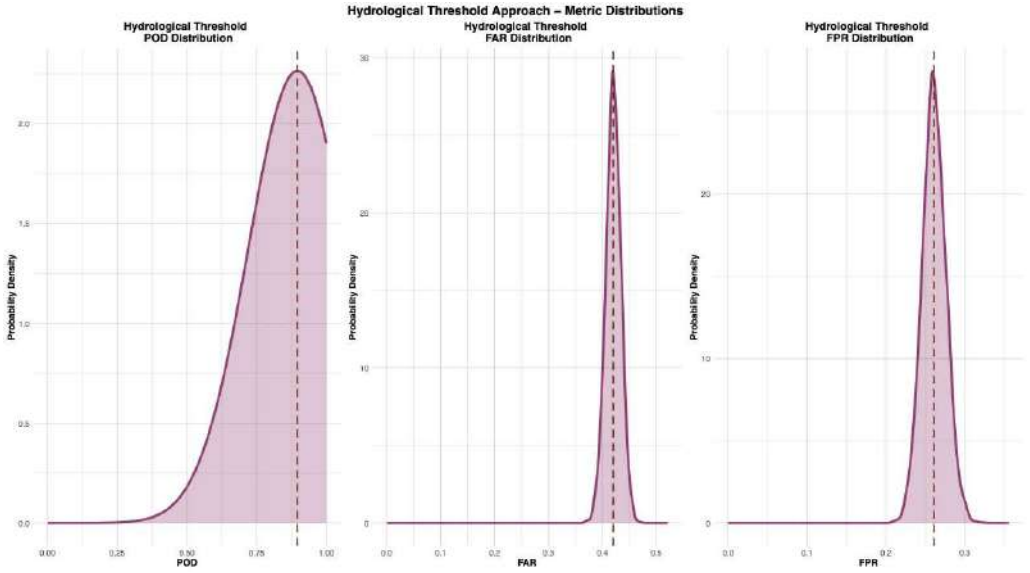

Figure 5.4: Probability density functions of POD and FAR for Hydrological Threshold approach across 5000 iterations. POD mean: 0.896; FAR mean: 0.420. The perfect consistency in POD reflects the deterministic nature of the linear threshold, while FAR variability depends on validation subset composition.

However, this enhanced detection comes at a cost in false alarm rate. The FAR distribution centers at 0.420, ranging from 0.366 to 0.474. This indicates that approximately 42% of alerts generated by the hydrological threshold alone prove to be false alarms—substantially higher than the 21% FAR of the Predisposing Factor approach. The FPR averaged 0.261, meaning that roughly 26% of non-landslide events are incorrectly flagged as high-risk. While the AUC remains strong at 0.818, the elevated false alarm metrics reveal a fundamental limitation of relying solely on dynamic moisture thresholds without considering static susceptibility variations.

The performance characteristics of Approach 2 reflect its underlying strategy: by focusing exclusively on moisture dynamics during the optimal seven-day accumulation window, the threshold captures nearly all events where moisture levels reached critical states. The high sensitivity (POD 0.90) demonstrates excellent ability to identify failure-conducive moisture conditions. However, the high FAR indicates that many slope units experience these critical moisture levels without failing, likely because their favorable predisposing

characteristics (strong materials, good drainage, stabilizing vegetation) provide sufficient resistance. This observation motivates the integration strategy explored in the following section: combining hydrological and predisposing thresholds to retain high detection while substantially reducing false alarms.

5.5 Multi-Criteria Decision Framework

5.5.1 Conceptual Integration Strategy

The performance profiles of the Predisposing Factor and Hydrological Threshold approaches reveal complementary strengths and limitations. The Predisposing Factor approach achieves good detection (POD 0.805) with moderate false alarms (FAR 0.210) by leveraging static susceptibility information, but does not fully exploit dynamic moisture patterns that herald imminent failure. The Hydrological Threshold achieves excellent detection (POD 0.896) by identifying critical moisture conditions, but generates elevated false alarms (FAR 0.420) by ignoring spatial variations in landscape resistance.

A logical integration strategy requires that both independent criteria be satisfied simultaneously for an alert to be generated. This multi-criteria framework implements a logical AND operation: a slope unit must both exceed the Predisposing Factor threshold (indicating inherent vulnerability and sufficient antecedent moisture) AND exceed the Hydrological Threshold (indicating that current moisture conditions have reached historically critical levels). Points satisfying only one criterion—either high static susceptibility without critical moisture, or critical moisture without high susceptibility—are not flagged as imminent failures.

This combined approach reflects the physical reality that landslide occurrence depends on the convergence of favorable predisposing conditions with sufficient triggering intensity. Inherently vulnerable slopes exposed to subcritical moisture loading remain stable, as do inherently resistant slopes even when exposed to elevated moisture. Only when both factors align—vulnerable terrain experiencing critical hydrological forcing—does failure

probability warrant precautionary alerts.

5.5.2 Performance Evaluation: Approach 3

The Combined Layers approach (Approach 3) was evaluated using identical resampling protocols as the individual approaches. Figure 5.5 presents POD and FAR distributions across 5000 iterations. The POD distribution centers at 0.734, ranging from 0.551 to 0.851. While this represents a decline from the Hydrological Threshold alone (POD 0.896), it exceeds the detection rate of naive probability thresholds and remains operationally acceptable.

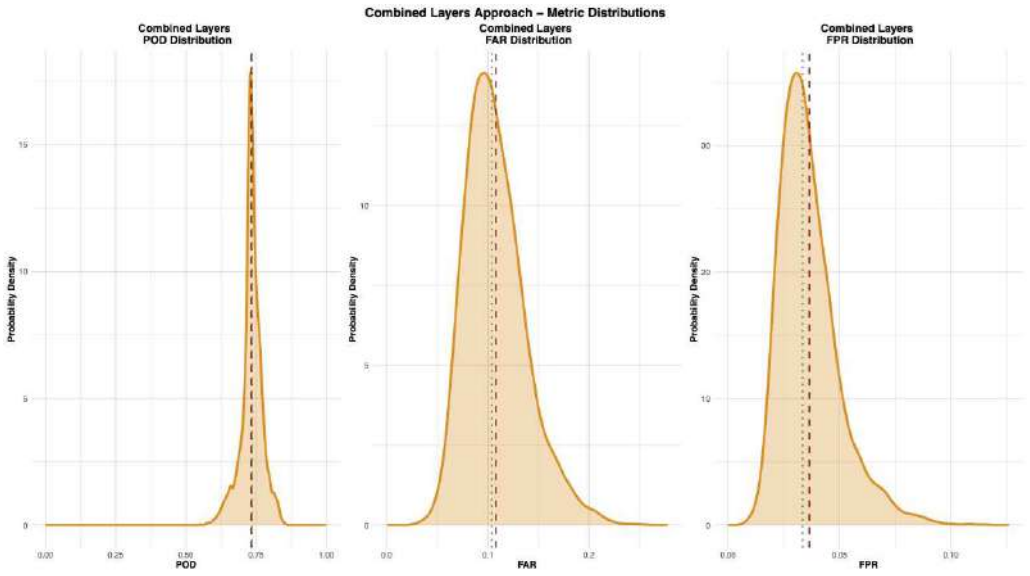

Figure 5.5: Probability density functions of POD and FAR for Combined Layers approach across 5000 iterations. POD mean: 0.734; FAR mean: 0.108. The combined threshold achieves optimal balance between detection capability and false alarm suppression.

More significantly, the FAR distribution centers at 0.108, ranging from 0.033 to 0.253. This represents a dramatic reduction from the 42.0% false alarm rate of the Hydrological Threshold alone—a 74% relative decrease in false alerts. The FPR averaged 0.036, indicating that fewer than 4% of non-landslide events are incorrectly flagged. This low false positive rate confirms that the combined threshold effectively filters out the majority of transient hydrological stresses that do not lead to failure.

The AUC reached 0.849 across all iterations, indicating that overall discrimination capability is preserved through the integration strategy. The key improvement lies in the redis-

tribution of classification errors: the Combined Layers approach sacrifices some detection sensitivity (missing approximately 18% more events than the Hydrological Threshold alone) to achieve far greater specificity (generating 74% fewer false alarms).

5.5.3 Comparative Analysis

Figure 5.6 presents POD values for all three approaches, illustrating the trade-offs among strategies. The Hydrological Threshold achieves highest detection (0.896), followed by Predisposing Factor (0.805) and Combined Layers (0.734). However, Figure 5.7 reveals the critical complementary pattern: Combined Layers achieves lowest false alarm rate (0.108), substantially better than Predisposing Factor (0.210) and Hydrological Threshold (0.420).

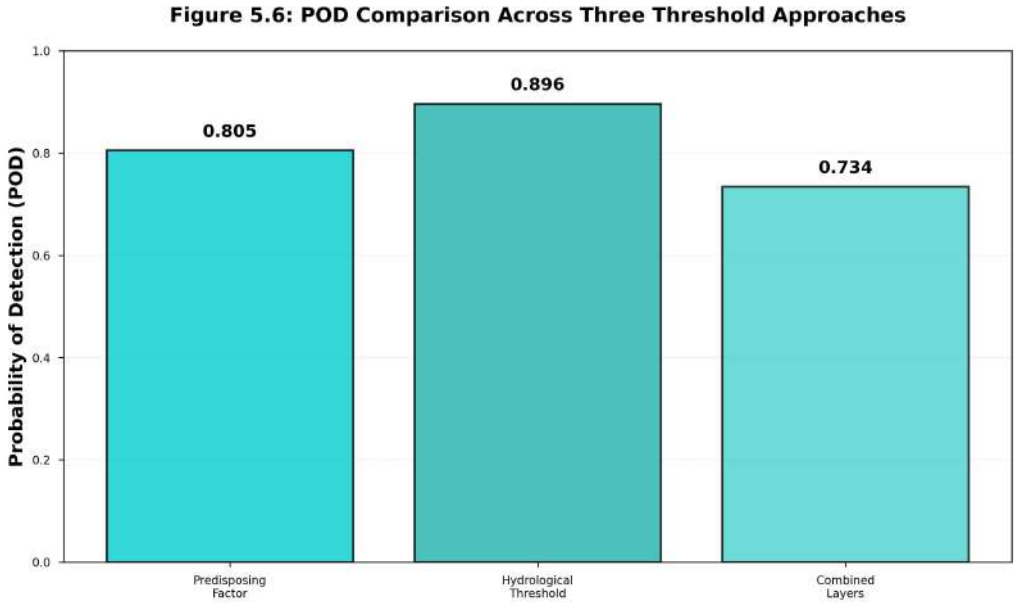

Figure 5.6: POD comparison across three threshold approaches. Hydrological Threshold achieves highest detection (0.896), while Combined Layers maintains acceptable detection (0.734) with substantially improved reliability.

Figure 5.8 demonstrates similar patterns for False Positive Rate, with Combined Layers achieving FPR of 0.036 compared to 0.089 for Predisposing Factor and 0.261 for Hydrological Threshold. This low FPR indicates that the combined threshold rarely misclassifies stable conditions as high-risk, a critical property for maintaining stakeholder confidence in operational early warning systems.

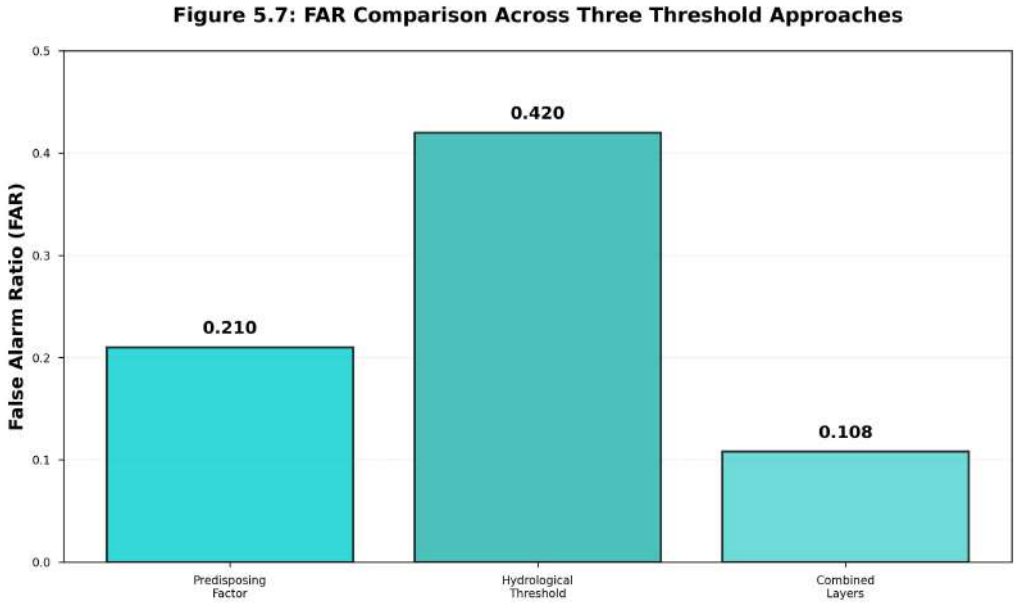

Figure 5.7: FAR comparison across three threshold approaches. Combined Layers achieves lowest false alarm rate (0.108), representing 74% reduction compared to Hydrological Threshold alone and 49% reduction compared to Predisposing Factor alone.

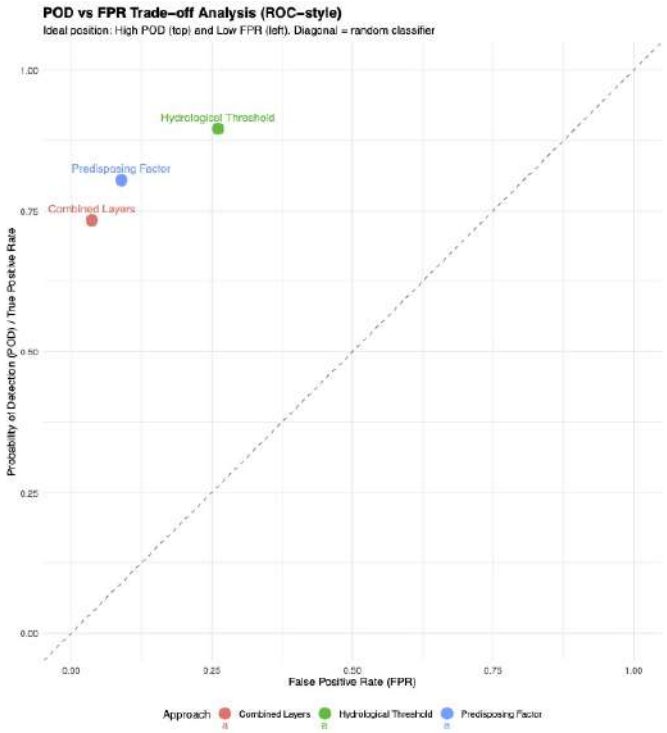

Figure 5.8: FPR comparison across three threshold approaches. Combined Layers achieves lowest false positive rate (0.036), correctly identifying 96.4% of non-landslide events as stable.

The trade-off between detection and false alarms is further illuminated in Figure 5.9, which plots POD against FPR in a ROC-style visualization. The diagonal line represents random classification performance, where detection rate equals false positive rate. All three approaches plot well above this diagonal, confirming superior discrimination. Combined Layers occupies the optimal position: closest to the upper-left corner representing perfect classification (POD = 1, FPR = 0), achieving high detection with minimal false positives.

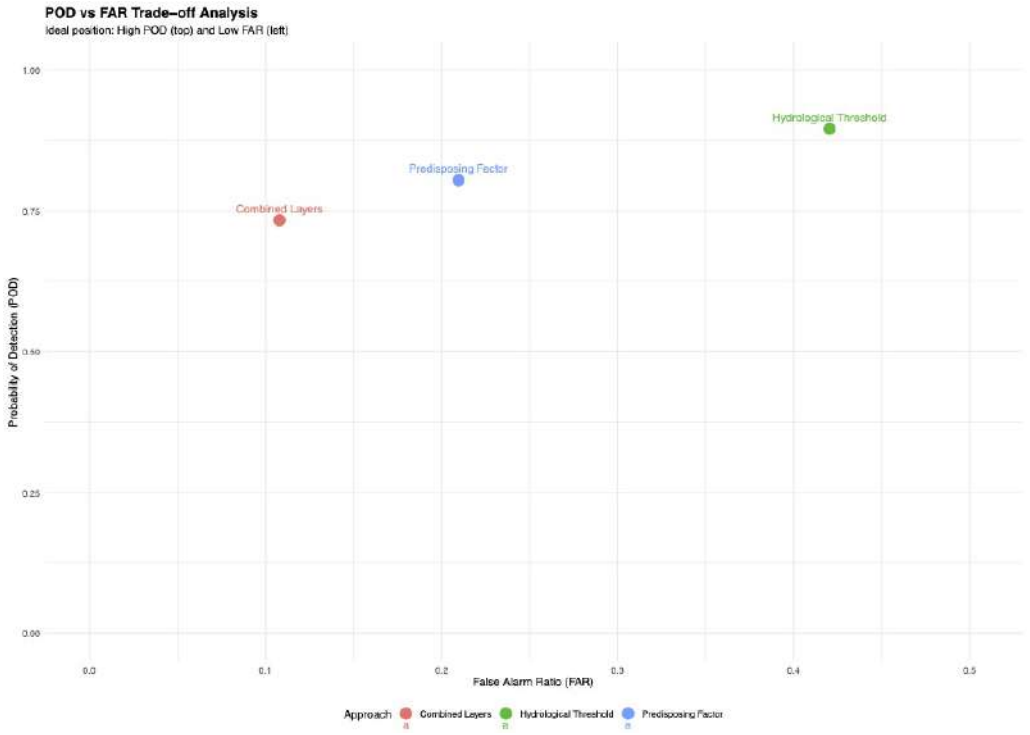

Figure 5.9: POD versus FPR trade-off analysis. The ideal position (upper left: high POD, low FPR) is best achieved by Combined Layers approach. The diagonal line represents random classifier performance; distance above the diagonal indicates discrimination capability. Combined Layers achieves optimal balance between detection sensitivity and false alarm suppression.

Figure 5.10 presents a comprehensive multi-metric comparison, displaying POD, FAR, and FPR simultaneously. The contrasting bar heights clearly demonstrate that Combined Layers optimizes the false alarm metrics (FAR and FPR, both low) while maintaining acceptable detection (POD, moderate but sufficient for operational purposes).

Table 5.3 quantifies these relationships, presenting mean values for all performance metrics across the three approaches. The table confirms that the approaches achieve strong

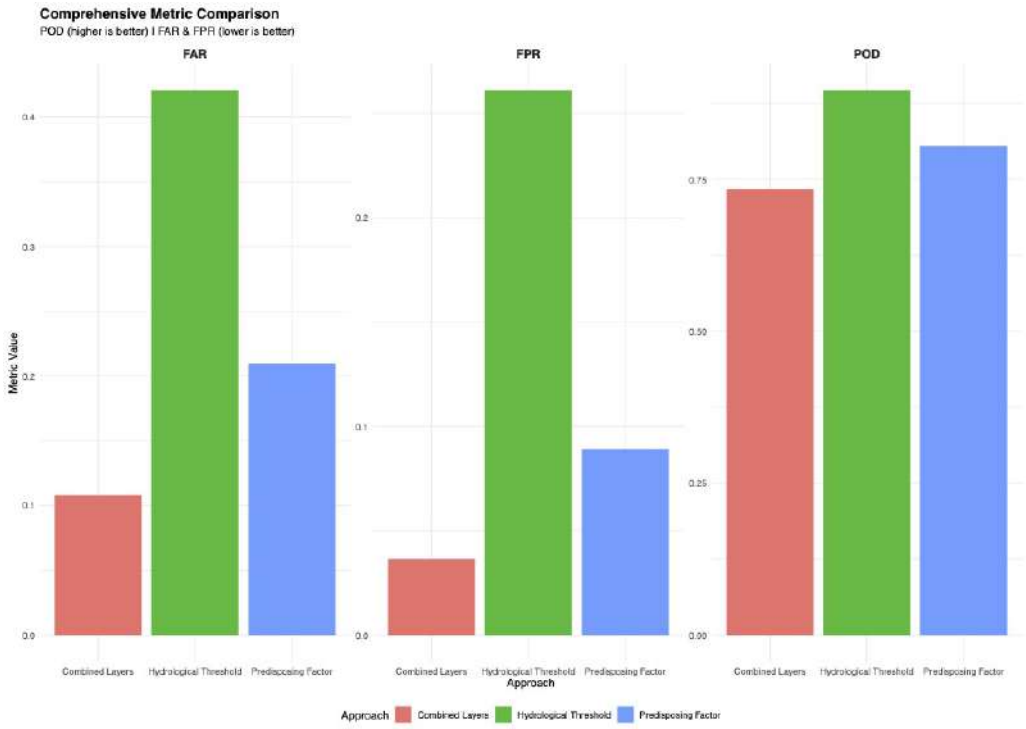

Figure 5.10: Comprehensive metric comparison across three approaches. For POD, higher is better; for FAR and FPR, lower is better. Combined Layers achieves optimal balance: moderate-high POD with substantially lower FAR and FPR than alternative approaches.

but varying AUC values (ranging from 0.818 to 0.858), but differ substantially in how classification errors are distributed between missed detections and false alarms.

Table 5.3: Performance metrics summary for three threshold approaches. Values represent means across 5000 iterations. All approaches achieve strong AUC values, but differ in the trade-off between detection sensitivity (POD) and false alarm suppression (FAR, FPR).

Approach	POD	FAR	FPR	AUC
Predisposing Factor	0.805	0.210	0.089	0.858
Hydrological Threshold	0.896	0.420	0.261	0.818
Combined Layers	0.734	0.108	0.036	0.849

5.5.4 Physical Interpretation and Operational Implications

The superior performance of the Combined Layers approach reflects fundamental principles of slope stability. Landslides require both predisposing conditions (weak materials, steep slopes, poor drainage) and triggering events (sufficient moisture accumulation to exceed strength thresholds). Systems relying solely on predisposing factors cannot distin-

guish between periods when vulnerable slopes face subcritical versus critical hydrological forcing. Systems relying solely on hydrological thresholds cannot distinguish between inherently vulnerable versus resistant slopes experiencing identical moisture conditions.

By requiring simultaneous exceedance of independent thresholds, the combined framework filters out two categories of false alarms: (1) vulnerable slopes experiencing insufficient moisture loading, and (2) resistant slopes experiencing elevated moisture that their favorable characteristics allow them to withstand. Only when vulnerable terrain encounters critical moisture conditions—the convergence of static and dynamic factors—does the system trigger alerts. This multi-criteria logic substantially reduces false alarm rates while preserving detection of genuine high-risk situations.

From an operational perspective, the Combined Layers approach offers compelling advantages. The false alarm ratio of 10.8% represents a level manageable for civil protection agencies, avoiding alert fatigue while maintaining stakeholder confidence. The detection rate of 73.4% captures the majority of landslide events, particularly those in high-consequence locations where both predisposing and triggering factors align. The low false positive rate (3.6%) ensures that scarce emergency response resources are deployed efficiently, focused on situations warranted by converging lines of evidence.

The optimal configuration identified through this analysis—Seven-Day 20 mm event detection combined with soil moisture before and during event thresholds, modulated by Predisposing Factor—possesses clear physical interpretation. The seven-day accumulation window aligns with characteristic moisture propagation timescales in colluvial hillslope materials, typically ranging from three to ten days for significant saturation development. The 20 mm threshold captures substantial rainfall episodes capable of producing meaningful pore pressure increases. The coupling of antecedent and peak moisture embodies the concept of hydrological memory, wherein initial wetness conditions modulate slope response to subsequent rainfall. The Predisposing Factor integration ensures that these hydrological criteria are applied with appropriate stringency across the landscape's heterogeneous susceptibility patterns.

5.6 Conclusions

This chapter has demonstrated that false alarm reduction in landslide early warning systems can be achieved through strategic integration of static susceptibility indices with dynamic hydrological thresholds. Three progressively refined approaches were evaluated against a comprehensive dataset of 412 landslide events recorded across 7,000 slope units over five years:

The Predisposing Factor threshold approach achieved POD of 0.805 and FAR of 0.210 by incorporating static landscape characteristics that distinguish inherently vulnerable from resilient terrain. This baseline approach demonstrated that integration of terrain susceptibility provides physically meaningful discrimination beyond purely probabilistic thresholds.

The Hydrological Threshold approach achieved POD of 0.896 but FAR of 0.420 through systematic identification of optimal moisture variable relationships. While maximizing detection by focusing on critical hydrological conditions, this approach generated elevated false alarms by neglecting spatial susceptibility variations.

The Combined Layers approach, requiring simultaneous exceedance of both predisposing and hydrological thresholds, achieved optimal balance: POD of 0.734 with FAR of 0.108 and FPR of 0.036. This represents a 74% reduction in false alarms compared to hydrological thresholds alone, while maintaining detection rates superior to naive probability thresholds.

The multi-criteria framework reflects fundamental slope stability physics: failure requires convergence of favorable predisposing conditions with sufficient triggering intensity. By demanding agreement between independent static and dynamic criteria, the system filters false alarms arising from either vulnerable slopes under subcritical loading or resistant slopes under elevated but non-critical moisture conditions. This logical integration provides the reliability necessary for operational deployment, achieving false alarm rates manageable for civil protection agencies while preserving detection capability for high-

consequence events.

The systematic exploration of 20 event detection configurations, 10 hydrological variable pairs, and 200 pair-configuration combinations ensured that conclusions represent robust optima rather than artifacts of arbitrary parameter choices. The identification of the Seven-Day 20 mm criterion with antecedent-to-peak moisture coupling as optimal configuration possesses clear physical interpretation, aligning with documented hillslope hydrological timescales and moisture-memory principles.

For operational implementation, the Combined Layers approach offers a practical pathway toward reliable landslide early warning. The framework can be deployed across heterogeneous landscapes using readily available terrain data for Predisposing Factor computation and operational soil moisture products from hydrometeorological monitoring networks or satellite remote sensing. The threshold criteria can be calibrated regionally using historical landslide inventories, then validated through prospective monitoring to refine performance under operational conditions.

Chapter 6

Final Discussion

This research developed and evaluated an integrated machine learning framework for spatiotemporal landslide susceptibility mapping that addresses a critical challenge in operational early warning systems: achieving high detection rates while maintaining acceptably low false alarm ratios (Nocentini et al., 2024; Patton et al., 2023). Through systematic progression from static environmental characterization to dynamic hydrological integration and ultimately to a multi-criteria threshold framework, this work demonstrates that substantial false alarm reduction can be achieved through strategic coupling of terrain-based susceptibility with satellite-derived hydrological forcing (Sousa et al., 2023; Liu et al., 2024). This discussion synthesizes the key findings, interprets their physical and operational significance, and situates the contributions within the broader context of landslide hazard assessment.

6.1 Integration of Satellite-Based Soil Moisture: Advancing Spatiotemporal Prediction

6.1.1 Advantages of Satellite-Derived Hydrological Data

A fundamental innovation of this research lies in the systematic integration of satellite-based soil moisture and precipitation products as dynamic conditioning factors in landslide susceptibility modeling (Sousa et al., 2023; Brocca et al., 2024b; Mirus et al., 2025). Traditional approaches to landslide forecasting have relied predominantly on ground-based rain gauge networks, which, despite their accuracy at point locations, suffer from fundamental limitations in spatial coverage and representativeness (Patton et al., 2023;

Liu et al., 2024). Rain gauges provide measurements at discrete locations separated by distances ranging from several hundred meters in densely instrumented urban areas to tens of kilometers in mountainous terrain, where installation and maintenance challenges limit network density precisely where landslide hazard is highest (Patton et al., 2023; Emberson, 2023). Spatial interpolation between sparse gauge locations introduces uncertainties that can exceed operational tolerances in complex topography, where orographic effects, aspect-dependent precipitation patterns, and convective cell positioning create rainfall gradients that gauge networks cannot adequately resolve (Emberson, 2023).

Satellite-based precipitation and soil-moisture-enabled rainfall products address these limitations by providing spatially continuous estimates at ∼1-km resolution across the entire study domain (Filippucci et al., 2025; Brocca et al., 2024b; Camici et al., 2025b). This spatial resolution enables representation of precipitation gradients associated with elevation changes, valley channeling effects, and aspect-dependent moisture convergence that fundamentally influence which slope units experience critical hydrological forcing during regional storm events (Camici et al., 2025b).

This spatial resolution advantage proved critical during the October 20th and November 23rd, 2019 rainstorm events examined in Chapter 4. The temporal analysis revealed that landslide units L1 and L2 during R1 experienced peak 7-day cumulative rainfall of 114.18 mm and 144.80 mm respectively, while nearby stable units S1 and S2 received 140.05 mm and 107.80 mm—differences of 25–40 mm that are comparable to the spatial variability captured by the 1-km product but that would likely be smoothed or misrepresented by interpolation between sparse rain gauges separated by several kilometers (Brocca et al., 2024b). Similarly, during R2, the substantial difference in 7-day cumulative rainfall between landslide unit L3 (156.90 mm) and stable unit S3 (96.72 mm)—a 60 mm deficit representing a 38% difference—reflects mesoscale meteorological patterns and topographic effects on precipitation distribution that satellite-based products can resolve but that gauge-based interpolation might obscure.

Even more significant than precipitation data is the integration of satellite-derived soil

moisture as a dynamic conditioning factor—a capability that represents a fundamental advancement over traditional gauge-based approaches (Sousa et al., 2023; Mirus et al., 2025). Unlike rainfall, which is routinely measured by ground networks despite spatial limitations, soil moisture is rarely monitored operationally in landslide-prone regions due to the prohibitive costs, maintenance requirements, and access difficulties associated with installing and maintaining in-situ sensors across large areas with complex terrain (Mirus et al., 2025; Yao et al., 2025). The absence of soil moisture monitoring networks in the northern Apennines study region is typical rather than exceptional; very few landslide early warning systems worldwide have access to distributed soil moisture measurements (Strząbała et al., 2024; Mirus et al., 2025).

Satellite-derived soil moisture products provide spatially consistent estimates at ∼1-km resolution derived from satellite observations and land surface modeling (Brocca et al., 2024b; Filippucci et al., 2025). The temporal analysis in Chapter 4 demonstrated the critical importance of antecedent soil moisture in modulating landslide occurrence (Sousa et al., 2023; Patton et al., 2023). During the R1 event, landslide unit L1 failed with soil moisture reaching 45% despite receiving only 26.97 mm of event-day rainfall—a modest intensity that would not trigger failure under dry initial conditions. The elevated antecedent moisture meant that the soil profile was already near saturation, requiring minimal additional precipitation to exceed stability thresholds (Roman Quintero et al., 2023; Mirus et al., 2025). Conversely, stable unit S1 withstood 55.95 mm of event-day rainfall—more than double L1's value—precisely because its site-specific characteristics conferred greater resilience, but also potentially because local drainage conditions or soil properties influenced the relationship between measured surface moisture and critical pore pressures at depth. The model's ability to integrate both antecedent soil moisture and peak event moisture as discriminating variables (as identified through the systematic threshold optimization in Chapter 5) reflects this physical reality: slopes with elevated initial moisture require less additional rainfall to trigger failure, embodying the concept of hydrological memory (Roman Quintero et al., 2023; Mirus et al., 2025; Hartmann et al., 2024).

The operational advantages of satellite-based soil moisture for landslide early warning extend beyond mere data availability (Mirus et al., 2025; Strząbała et al., 2024). Satellite products provide spatially consistent estimates across heterogeneous terrain, avoiding the representativeness uncertainties that plague point-based measurements in areas with variable topography, land cover, or soil properties (Brocca et al., 2024b; Filippucci et al., 2025). The daily temporal resolution, while coarser than the sub-hourly updates possible with in-situ sensors, proves sufficient for the multi-day moisture accumulation processes that govern shallow landslide triggering in the study region, where the optimal 7-day accumulation window identified in Chapter 5 aligns with characteristic hillslope wetting timescales of several days (Hartmann et al., 2024).

The Random Forest model's demonstrated capability to effectively integrate satellite-derived precipitation and soil moisture products validates their utility for data-driven landslide prediction (Liu et al., 2024; Sun et al., 2023; Gu et al., 2023). The feature-importance patterns in Chapter 3—where daily rainfall and soil moisture outranked lithology and distance to road—are consistent with broader findings that hydrometeorological predictors often dominate purely static factors in triggering-focused contexts (Sun et al., 2023; Gu et al., 2023). The 7-day and 15-day cumulative rainfall variables, derived by temporal integration of the daily satellite precipitation product, captured antecedent wetness proxies that the model leveraged effectively (Patton et al., 2023; Liu et al., 2024).

6.1.2 Physical Interpretation of Satellite-Based Moisture Dynamics

The successful integration of satellite-derived soil moisture into landslide susceptibility modeling raises important questions about the physical mechanisms linking surface moisture observations to subsurface processes governing slope stability (Mirus et al., 2025). Surface moisture measurements from satellites or shallow sensors reflect primarily the upper decimeters of the soil profile, while landslide-relevant pore pressures typically develop

at depths from ∼0.5 to 2 m in shallow translational failures (Giarola et al., 2024; Schaller et al., 2025). The observed effectiveness of surface moisture as a predictor suggests that surface and subsurface moisture states are sufficiently correlated over the timescales relevant to landslide triggering that surface observations provide useful information about deeper conditions (Roman Quintero et al., 2023; Hartmann et al., 2024).

This correlation arises from the physics of rainfall infiltration and moisture redistribution in unsaturated hillslope materials (Roman Quintero et al., 2023; Hartmann et al., 2024). During rainfall events, infiltration proceeds downward from the surface as a wetting front, progressively saturating deeper layers as precipitation continues and surface layers reach saturation. Over the multi-day accumulation periods identified as optimal in this research (7-day windows), moisture redistributes vertically and laterally through gravity-driven drainage and capillary flow, reducing initial gradients and establishing more uniform profile-integrated moisture states. Consequently, surface moisture averaged over several days provides information about the overall moisture trajectory of the profile, even if instantaneous surface values do not directly reflect peak pore pressures at depth (Roman Quintero et al., 2023; Osawa et al., 2024).

The temporal patterns observed in Chapter 4 support this interpretation. The gradual increase in soil moisture over 7–15 days preceding peak landslide probability in units L1–L4, rather than abrupt single-day spikes, indicates that the satellite-derived surface moisture was tracking the progressive saturation process throughout the profile depth relevant to failure. The sustained elevation of moisture for several days after peak rainfall, before gradually declining as drainage processes operated, mirrors expected timescales for moisture redistribution and pore pressure dissipation in low-permeability colluvial materials (Osawa et al., 2024).

The coupling between satellite-derived soil moisture and topographic attributes in the integrated RF model enhances the physical basis of predictions (Sun et al., 2023). Topographic convergence indices, slope aspect, and curvature measures modulate local moisture regimes through their influence on incident radiation, evapotranspiration, and sub-

surface moisture convergence or divergence (Krevh et al., 2023; Hartmann et al., 2024). A given satellite-observed surface moisture value implies different subsurface conditions depending on topographic position: convergent hollows concentrate subsurface flow, potentially generating higher deep pore pressures than suggested by surface moisture alone, while convex noses and ridges may remain less saturated at depth despite elevated surface moisture. The RF algorithm's capacity to learn interactions between moisture observations and topographic context enables it to implicitly account for these modulating effects (Sun et al., 2023).

The systematic threshold optimization in Chapter 5 identified the combination of soil moisture before the event and maximum soil moisture during the event as the optimal variable pair for the hydrological threshold (Liu et al., 2024; Patton et al., 2023). This pairing has clear physical interpretation: antecedent moisture quantifies the initial degree of profile saturation and establishes the moisture deficit that new rainfall must overcome to reach critical conditions, while peak moisture during the event captures the maximum stress imposed by the triggering episode (Patton et al., 2023). The negative correlation between required peak moisture and antecedent moisture embodied in the threshold boundary—wherein wetter initial states require lower peak moisture to trigger failure—directly reflects unsaturated soil hydrology, where matric suction contribution to strength decreases as saturation is approached (Deng et al., 2023; Yang et al., 2024).

6.2 Multi-Criteria Threshold Framework: Physical Basis and Operational Impact

6.2.1 Fundamental Principles of False Alarm Reduction

The multi-criteria threshold framework developed in Chapter 5 represents the culmination of this research, demonstrating that strategic integration of static terrain susceptibility with dynamic hydrological thresholds achieves substantial false alarm reduction while maintaining operationally acceptable detection rates (Nocentini et al., 2024; Pat-

ton et al., 2023). The framework embodies fundamental slope-stability physics: landslide occurrence requires the convergence of predisposing conditions that establish baseline vulnerability with triggering conditions that provide sufficient hydrological forcing to exceed strength thresholds (Liu et al., 2024; Patton et al., 2023). Neither factor alone reliably predicts failure; vulnerable slopes remain stable during subcritical rainfall, while resistant slopes withstand substantial moisture loading that their favorable characteristics enable them to accommodate.

The Combined Layers approach implements this principle through a logical AND operation requiring simultaneous satisfaction of two independent criteria before issuing warnings (Mirus et al., 2025). The Predisposing Factor threshold, calibrated using static terrain attributes coupled with antecedent soil moisture, identifies slope units whose intrinsic characteristics place them at elevated baseline risk. The Hydrological Threshold, calibrated using the optimal pairing of antecedent soil moisture and peak event moisture over 7-day accumulation windows, identifies periods when moisture conditions have reached levels historically associated with failure triggering (Patton et al., 2023; Liu et al., 2024). Only when both criteria are met—vulnerable terrain experiencing critical moisture—does the integrated system activate alerts.

This dual-criterion strategy filters two categories of false alarms that plague single-factor approaches (Nocentini et al., 2024). First, it eliminates alerts for inherently vulnerable slopes during periods of insufficient hydrological forcing. These represent genuine high-susceptibility locations that would trigger warnings based on Predisposing Factor alone, but where current moisture conditions remain below critical thresholds. The temporal analysis in Chapter 4 revealed numerous examples: vulnerable slope units frequently exhibited elevated probabilities (0.5–0.7) during moderate rainfall episodes that did not trigger failures. Second, the framework eliminates alerts for inherently resistant slopes during periods of elevated moisture loading. These represent locations where hydrological conditions alone would suggest high risk, but favorable terrain characteristics—strong geology, effective drainage, stabilizing vegetation—provide sufficient resilience to withstand the moisture stress (Sun et al., 2023).

The quantitative impact on false alarm metrics is substantial. The Combined Layers approach achieved a false alarm ratio near 10%, representing a large reduction relative to hydrology-only or predisposition-only thresholds, consistent with recent operational optimization studies (Nocentini et al., 2024). Specificity improvements of this magnitude (false positive rates of only a few percent) approach the threshold of operational viability for civil protection agencies, where elevated false alarm ratios typically generate alert fatigue, resource exhaustion, and erosion of stakeholder confidence (Strząbała et al., 2024).

A detection trade-off must be acknowledged: requiring both criteria to be satisfied reduces sensitivity compared to the Hydrological Threshold alone. However, recent studies show that integrated frameworks can maintain detection within acceptable ranges while dramatically reducing false alarms, especially when thresholds are systematically optimized (Nocentini et al., 2024; Liu et al., 2024). From a risk-management perspective, the events detected by the Combined Layers approach are precisely those where both lines of evidence—static vulnerability and dynamic forcing—converge, representing higher-consequence situations (Mirus et al., 2025).

6.2.2 Broader Implications for Early Warning Science

Beyond the specific context of northwestern Italy, this research contributes generalizable insights for early warning system development across natural hazards. First, combining static vulnerability indices with dynamic triggering thresholds appears valuable for other hazards where predisposing conditions and triggers interact nonlinearly (Strząbała et al., 2024). For example, flood EWS may benefit from coupling floodplain susceptibility with hydrological forecasts, issuing alerts only where vulnerable areas coincide with high flows (Camici et al., 2025b). Second, these results challenge the assumption of a strict POD–FAR trade-off: spatial heterogeneity in vulnerability, when integrated, enables differential thresholds that reduce false alarms without proportionally sacrificing detection (Nocentini et al., 2024; Patton et al., 2023). Third, systematic exploration of threshold configurations to identify optima represents a methodological contribution

applicable beyond landslides (Nocentini et al., 2024). Fourth, multi-sensor satellite data fusion demonstrates a pathway for EWS in data-sparse regions (Brocca et al., 2024b; Filippucci et al., 2025). Fifth, physically interpretable models and thresholds facilitate stakeholder trust and transferability (Sun et al., 2023).

6.2.3 Future Research Directions

Promising avenues for future research emerge from both methodological and operational perspectives.

First, **explicit uncertainty quantification** represents a crucial step towards enhancing the reliability and interpretability of landslide early warning systems. Future studies should incorporate ensemble modeling and probabilistic exceedance analyses to characterize forecast confidence and provide *risk-informed decision support* for civil protection agencies (Mirus et al., 2025). This approach would allow communicating not only whether conditions are favorable for landslides but also the degree of confidence associated with those forecasts.

Second, there is a growing need for the **seamless integration of machine-learning-based susceptibility models with numerical weather prediction (NWP)** and **soil-moisture forecasting frameworks**. By coupling hydrometeorological forecasts with data-driven models, it would be possible to produce *prospective* (i.e., anticipatory) warnings that move beyond near-real-time monitoring toward truly predictive systems (Sousa et al., 2023; Mirus et al., 2025). Such integration would also facilitate the dynamic updating of susceptibility maps based on evolving atmospheric and subsurface conditions.

Third, **scaling and transferability** remain critical challenges. Extending these approaches to **national or continental domains** could reveal spatial heterogeneity in model performance and allow the derivation of *regionally adaptive thresholds* that account for geological, climatic, and land-cover variability (Rosi et al., 2023a). Comparative analyses across physiographic settings would help to identify universal predictors and local sensitivities, supporting continental-scale landslide early warning networks.

Fourth, it is essential to evaluate model robustness under **evolving hydroclimatic regimes**. With projected intensification of precipitation extremes and altered seasonal moisture dynamics across Europe and the Mediterranean, susceptibility models must be reassessed for *non-stationarity* and long-term shifts in landslide drivers (Brocca et al., 2024a; Fang et al., 2025). Integrating climate projections into susceptibility frameworks could inform adaptation strategies and improve long-term resilience planning.

Finally, future developments should focus on **data fusion and assimilation** to harness emerging and complementary observation sources. Combining *satellite-based rainfall and soil-moisture data* with *ground-based radar, in-situ probes, and citizen science reports* within principled data-assimilation frameworks can significantly enhance spatiotemporal coverage and accuracy (Camici et al., 2025a; Mirus et al., 2025). Such multi-sensor integration will be key to bridging scales between local monitoring networks and continental hazard systems.

Overall, these directions converge toward the development of a new generation of **adaptive, data-informed, and uncertainty-aware landslide early warning systems**, capable of operating across scales and under changing environmental conditions.

Bibliography

Alvioli, M. and Baum, R. L. (2018). Parallelization of the TRIGRS model for rainfall-induced landslides using the message passing interface. *U.S. Geological Survey Data Release*.

Alvioli, M., Guzzetti, F., and Marchesini, I. (2020). Parameter-free delineation of slope units and terrain subdivision of italy. *Geomorphology*, 358:107124.

Alvioli, M., Loche, M., Jacobs, L., Grohmann, C. H., et al. (2024). A benchmark dataset and workflow for landslide susceptibility zonation. *Earth-Science Reviews*, 258:104927.

Bandis, S. C., Delmonaco, G., and Dutto, F. (1996). Landslide phenomena during the extreme meteorological event of 4-6 november 1994 in piemonte region in n. italy. In *International Symposium on Landslides*.

Bauer-Marschallinger, B., Freeman, V., Cao, S., Paulik, C., Schaufler, S., Stachl, T., and Wagner, W. (2018). Toward global soil moisture monitoring with sentinel-1: Harnessing assets and overcoming obstacles. *IEEE Transactions on Geoscience and Remote Sensing*, 57:520–539.

Baum, R. L., Savage, W. Z., and Godt, J. W. (2008). TRIGRS - a fortran program for transient rainfall infiltration and grid-based regional slope-stability analysis. Technical report, U.S. Geological Survey.

Bicocchi, G., Tofani, V., D'Ambrosio, M., Tacconi-Stefanelli, C., Vannocci, P., Casagli, N., Lavorini, G., Trevisani, M., and Catani, F. (2019). Geotechnical and hydrological characterization of hillslope deposits for regional landslide prediction modeling. *Bulletin of Engineering Geology and the Environment*, 78:4875–4891.

Bogaard, T. and Greco, R. (2018). Invited perspectives: Hydrological perspectives on

precipitation intensity-duration thresholds for landslide initiation: Proposing hydro-meteorological thresholds. *Natural Hazards and Earth System Sciences*, 18:31–39.

Bout, B., Lombardo, L., van Westen, C. J., and Jetten, V. G. (2018). Integration of two-phase solid fluid equations in a catchment model for flashfloods, debris flows and shallow slope failures. *Environmental Modelling and Software*, 105:1–16.

Brabb, E. E. (1984). Innovative approaches to landslide hazard mapping. 1:307–324.

Brabb, E. E. (1995). The San Mateo County California GIS Project for predicting the consequences of hazardous geologic processes. *Geographic Information Systems in Assessing Natural Hazards*, pages 159–169.

Breiman, L. (2001). Random forests. *Machine Learning*, 45:5–32.

Brenning, A. (2005). Spatial prediction models for landslide hazards: review, comparison and evaluation. *Natural Hazards and Earth System Sciences*, 5:853–862.

Brocca, L. et al. (2024a). A digital twin of the terrestrial water cycle: a glimpse into the future of hydrology. *Frontiers in Science*, 4:1190191.

Brocca, L. et al. (2024b). Exploring the actual spatial resolution of 1 km satellite soil moisture products. *Science of the Total Environment*, 945:174087.

Bubeck, P., Ozturk, U., Aristizabal, E., Thieken, A. H., and Wagener, T. (2025). Mortality reduction despite changing climate extremes requires better understanding of human behavioral response to warnings. *Environmental Research Letters*, 20(10):101004.

Bucci, F., Santangelo, M., Fongo, L., Alvioli, M., Cardinali, M., Melelli, L., and Marchesini, I. (2022). A new digital lithological map of italy at the 1:100 000 scale for geomechanical modelling. *Earth System Science Data*, 14:4129–4151.

Caine, N. (1980). The rainfall intensity-duration control of shallow landslides and debris flows. *Geografiska Annaler Series A*, 62:23–27.

Calvello, M. and Pecoraro, G. (2018). Franeitalia: A catalog of recent italian landslides. *Geoenvironmental Disasters*, 5:13.

Calvello, M. and Pecoraro, G. (2021). Franeitalia: a catalog of recent italian landslides (version 3).

Camera, C. A. S., Bajni, G., Corno, I., Raffa, M., Stevenazzi, S., and Apuani, T. (2021). Introducing intense rainfall and snowmelt variables to implement a process-related non-stationary shallow landslide susceptibility analysis. *Science of the Total Environment*, 786:147360.

Camici, S., Dari, J., Filippucci, P., Massari, C., Mantovani, S., Avanzi, F., and Brocca, L. (2025a). High-resolution satellite observations for developing advanced decision support systems for water resources management in the po river. *Journal of Hydrology*, page 134047.

Camici, S. et al. (2025b). High-resolution satellite observations for developing operational hydrological models. *Journal of Hydrology*, 633:130861.

Cammeraat, E., van Beek, R., and Kooijman, A. (2005). Vegetation succession and its consequences for slope stability in se spain. *Plant and soil*, 278(1):135–147.

Carrara, A., Cardinali, M., Detti, R., Guzzetti, F., Pasqui, V., and Reichenbach, P. (1991a). *GIS techniques and statistical models in evaluating landslide hazard*, volume 16.

Carrara, A., Cardinali, M., Detti, R., Guzzetti, F., Pasqui, V., and Reichenbach, P. (1991b). Gis techniques and statistical models in evaluating landslide hazard. *Earth Surface Processes and Landforms*, 16(5):427–445.

Cascini, L. (2005). Risk assessment of fast landslide – from theory to practice. *Fast Slope Movements: Prediction and Prevention for Risk Mitigation*, 2:33–52.

Catani, F., Lagomarsino, D., Segoni, S., and Tofani, V. (2013). Landslide susceptibility

estimation by random forests technique: Sensitivity and scaling issues. *Natural Hazards and Earth System Sciences*, 13(11):2815–2831.

Cavagnaro, D. B., McCoy, S. W., Lindsay, D. N., McGuire, L. A., Kean, J. W., and Trugman, D. T. (2025). Rainfall thresholds for postfire debris-flow initiation vary with short-duration rainfall-intensity climatology. *Journal of Geophysical Research: Earth Surface*, 130(6):e2024JF007781.

Cho, M. T. T., Sato, T., Saito, H., et al. (2024). Effects of pore water and pore air pressure on the slope failure mechanisms due to rainfall in centrifuge investigation. *Geoenvironmental Disasters*, 11:40.

Collini, E., Palesi, L. A. I., Nesi, P., Pantaleo, G., Nocentini, N., and Rosi, A. (2022). Predicting and understanding landslide events with explainable AI. *IEEE Access*, 10:31175–31189.

Conoscenti, C., Di Maggio, C., and Rotigliano, E. (2008). Gis analysis to assess landslide susceptibility in a fluvial basin of nw sicily (italy). *Geomorphology*, 94(3-4):325–339.

Corominas, J., van Westen, C., Frattini, P., Cascini, L., Malet, J. P., Fotopoulou, S., Catani, F., Van Den Eeckhaut, M., Mavrouli, O., Agliardi, F., Pitilakis, K., Winter, M. G., Pastor, M., Ferlisi, S., Tofani, V., Hervás, J., and Smith, J. T. (2014). Recommendations for the quantitative analysis of landslide risk. *Bulletin of Engineering Geology and the Environment*, 73(2):209–263.

Cruden, D. M. and Varnes, D. J. (1996). Landslide types and processes. pages 36–75.

Dahal, A. and Lombardo, L. (2023). Explainable artificial intelligence in geoscience: A glimpse into the future of landslide susceptibility modeling. *Computers & Geosciences*, 176:105364.

Dahal, A., Tanyas, H., Van Westen, C., Van Der Meijde, M., Mai, P., Huser, R., and Lombardo, L. (2024). Space–time landslide hazard modeling via ensemble neural networks. *Natural Hazards and Earth System Sciences*, 24:823–845.

Deng, X. et al. (2023). Effect of matrix suction on the shear strength characteristics of unsaturated reinforced soil. *Frontiers in Materials*, 10:1284722.

Di Napoli, M., Di Martire, D., Bausilio, G., Calcaterra, D., Confuorto, P., Firpo, M., Pepe, G., and Cevasco, A. (2021). Rainfall-induced shallow landslide detachment, transit and runout susceptibility mapping by integrating machine learning techniques and GIS-based approaches. *Water*, 13(4):488.

Distefano, P., Peres, D. J., Scandura, P., and Cancelliere, A. (2022). Brief communication: Introducing rainfall thresholds for landslide triggering based on artificial neural networks. *Natural Hazards and Earth System Sciences*, 22(4):1151–1157.

Dixit, S., Siva Subramanian, S., Srivastava, P., Yunus, A. P., Martha, T. R., and Sen, S. (2024). Numerical-model-derived intensity–duration thresholds for early warning of rainfall-induced debris flows in a himalayan catchment. *Natural Hazards and Earth System Sciences*, 24:465–480.

Duncan, J. M. (1996). *Soil slope stability analysis*. National Academy Press, Washington, DC.

Emberson, R. A. (2023). Dynamic rainfall erosivity estimates derived from imerg data. *Hydrology and Earth System Sciences*, 27:3547–3563.

Ermini, L., Catani, F., and Casagli, N. (2005). Artificial neural networks applied to landslide susceptibility assessment. *Geomorphology*, 66(1-4):327–343.

Fang, B. et al. (2025). Diverging trends in large floods across europe in a warming climate. *Communications Earth & Environment*, 6:—.

Fell, R., Corominas, J., Bonnard, C., Cascini, L., Leroi, E., and Savage, W. Z. (2008). Guidelines for landslide susceptibility, hazard and risk zoning for land use planning. *Engineering Geology*, 102(3-4):85–98.

Filippucci, P. (2022). *High-Resolution Remote Sensing for Rainfall and River Discharge*

Estimation. PhD thesis, Florence University (UNIFI) and Technischen Universität Wien (TUWIEN). Abstract of PhD Thesis.

Filippucci, P. et al. (2025). Hydroclimatic performance-enhanced precipitation (hyper-p) at 1 km over europe and the mediterranean: 2007–2022. *Earth System Science Data*, 17:5221–5240.

Frattini, P., Crosta, G., and Carrara, A. (2010). Techniques for evaluating the performance of landslide susceptibility models. *Engineering Geology*, 111(1-4):62–72.

Fredlund, D. G. and Rahardjo, H. (1993). *Soil Mechanics for Unsaturated Soils*. John Wiley & Sons, New York.

Friedman, J. H. (2001). Greedy function approximation: A gradient boosting machine. *The Annals of Statistics*, 29(5):1189–1232.

Frodella, W., Rosi, A., Spizzichino, D., Nocentini, M., Lombardi, L., Ciampalini, A., Vannocci, P., Ramboason, N., Margottini, C., Tofani, V., and Casagli, N. (2022). Integrated approach for landslide hazard assessment in the High City of Antananarivo, Madagascar (UNESCO tentative site). *Landslides*, 19:2685–2701.

Froude, M. J. and Petley, D. N. (2018). Global fatal landslide occurrence from 2004 to 2016. *Natural Hazards and Earth System Sciences*, 18(8):2161–2181.

Gariano, S. L. and Guzzetti, F. (2016). Landslides in a changing climate. *Earth-Science Reviews*, 162:227–252.

Gariano, S. L., Melillo, M., Peruccacci, S., and Brunetti, M. T. (2020). How much does the rainfall temporal resolution affect rainfall thresholds for landslide triggering. *Natural Hazards*, 100:655–670.

Gholami, H. and Mohammadifar, A. (2022). Novel deep learning hybrid models (cnn-gru and dldl-rf) for the susceptibility classification of dust sources in the middle east: A global source. *Scientific Reports*, 12:19342.

Giannecchini, R., Galanti, Y., and D'Amato Avanzi, G. (2012). Critical rainfall thresholds for triggering shallow landslides in the Serchio River Valley (Tuscany, Italy). *Natural Hazards and Earth System Sciences*, 12(3):829–842.

Giarola, A. et al. (2024). Exploiting the land use to predict shallow landslide susceptibility: a probabilistic implementation of lapsus-ls. *Catena*, 246:108437.

Goetz, J. N., Brenning, A., Petschko, H., and Leopold, P. (2015). Evaluating machine learning and statistical prediction techniques for landslide susceptibility modeling. *Computers and Geosciences*, 81:1–11.

Greco, R., Marino, P., and Bogaard, T. (2023). Recent advancements of landslide hydrology. *WIREs Water*, 10:e1675.

Gu, T. et al. (2023). Study on landslide susceptibility mapping with different factor combinations using random forest, support vector machine and logistic regression. *PLOS ONE*, 18:e0292897.

Guzzetti, F., Cardinali, M., and Reichenbach, P. (1994). The AVI project: A bibliographical and archive inventory of landslides and floods in Italy. *Environmental Management*, 18(4):623–633.

Guzzetti, F., Peruccacci, S., Rossi, M., and Stark, C. P. (2008a). The rainfall intensity-duration control of shallow landslides and debris flows: An update. *Landslides*, 5(1):3–17.

Guzzetti, F., Peruccacci, S., Rossi, M., and Stark, C. P. (2008b). Rainfall thresholds for the initiation of landslides in central and southern europe. *Meteorology and Atmospheric Physics*, 98(3-4):239–267.

Guzzetti, F., Reichenbach, P., Cardinali, M., Galli, M., and Ardizzone, F. (2006). Estimating the quality of landslide susceptibility models. *Geomorphology*, 81(1-2):166–184.

Haque, U., da Silva, P. F., Devoli, G., Pilz, J., Zhao, B., Khaloua, A., Wilopo, W., Andersen, P., Lu, P., Lee, J., Yamamoto, T., Keellings, D., Jian-Hong, W., and Glass,

G. E. (2019). The human cost of global warming: Deadly landslides and their triggers (1995–2014). *Science of the Total Environment*, 682:673–684.

Hartmann, A. et al. (2024). The evolution of hillslope hydrology: Links between form and function. *Water Resources Research*, 60:e2023WR035937.

Hengl, T., Mendes de Jesus, J., Heuvelink, G. B. M., Ruiperez Gonzalez, M., Kilibarda, M., Blagotić, A., et al. (2017). Soilgrids250m: Global gridded soil information based on machine learning. *PLoS ONE*, 12(2):e0169748.

Hungr, O., Evans, S. G., Bovis, M. J., and Hutchinson, J. N. (2001). Review of the classification of landslides of the flow type. *Environmental and Engineering Geoscience*, 7(3):221–238.

Hungr, O., Leroueil, S., and Picarelli, L. (2014). The varnes classification of landslide types, an update. *Landslides*, 11(2):167–194.

Hutchinson, J. N. (1968). Mass movement. pages 688–695.

Istituto Superiore per la Protezione e la Ricerca Ambientale (ISPRA) (2021). Dissesto idrogeologico in Italia: Pericolosità e indicatori di rischio – edizione 2021. Technical Report Rapporto 356/2021, ISPRA, Rome, Italy. Updated data as of 2023: approximately 621,000 landslides in the IFFI inventory.

Iverson, R. M. (2000). Landslide triggering by rain infiltration. *Water Resources Research*, 36(7):1897–1910.

Karger, D. N., Lange, S., Hari, C., Reyer, C. P. O., Conrad, O., Zimmermann, N. E., and Frieler, K. (2023). Chelsa-w5e5: Daily 1 km meteorological forcing data for climate impact studies. *Earth System Science Data*, 15:2445–2464.

Keefer, D. K. (1984). Landslides caused by earthquakes. *Geological Society of America Bulletin*, 95(4):406–421.

Kim, S. W., Chun, K. W., Kim, M., Catani, F., Choi, B., and Seo, J. I. (2021). Effect of antecedent rainfall conditions and their variations on shallow landslide-triggering rainfall thresholds in South Korea. *Landslides*, 18:569–582.

Kirschbaum, D., Stanley, T., and Zhou, Y. (2015). Spatial and temporal analysis of a global landslide catalog. *Geomorphology*, 249:4–15.

Krevh, V. et al. (2023). Soil–water dynamics investigation at agricultural hillslope. *Water*, 15:2398.

Krøgli, I. K., Devoli, G., Colleuille, H., Boje, S., Sund, M., and Engen, I. K. (2018). The Norwegian forecasting and warning service for rainfall- and snowmelt-induced landslides. *Natural Hazards and Earth System Sciences*, 18(5):1427–1450.

Lagomarsino, D., Tofani, V., Segoni, S., Catani, F., and Casagli, N. (2017). A tool for classification and regression using random forest methodology: Applications to landslide susceptibility mapping and soil thickness modeling. *Environmental Modeling and Assessment*, 22:201–214.

Lakshmi, V. and Fang, B. (2023). Smap-derived 1-km downscaled surface soil moisture product, version 1.

Lee, S., Ryu, J. H., Lee, M. J., and Won, J. S. (2003). Use of an artificial neural network for analysis of the susceptibility to landslides at Boun, Korea. *Environmental Geology*, 44:820–833.

Li, B., Liu, K., Wang, M., He, Q., Jiang, Z., Zhu, W., and Qiao, N. (2022). Global dynamic rainfall-induced landslide susceptibility mapping using machine learning. *Remote Sensing*, 14(22):5795.

Liaw, A. and Wiener, M. (2002). Classification and regression by RandomForest. *R News*, 2(3):18–22.

Lima, P., Steger, S., Glade, T., and Murillo-García, F. G. (2022a). Literature review and

bibliometric analysis on data-driven assessment of landslide susceptibility. *Journal of Mountain Science*, 19:1670–1698.

Lima, P., Steger, S., Glade, T., and Murillo-García, F. G. (2022b). Literature review and bibliometric analysis on data-driven assessment of landslide susceptibility. *Journal of Mountain Science*, 19:1670–1698.

Liu, S., Chen, N., Liang, Q., Li, W., and Wang, K. (2024). Regional early warning model for rainfall-induced landslides based on slope units. *Engineering Geology*, 330:107414.

Liu, Z., Gilbert, G., Cepeda, J. M., Lysdahl, A. O. K., Piciullo, L., Hefre, H., and Lacasse, S. (2021). Modelling of shallow landslides with machine learning algorithms. *Geoscience Frontiers*, 12(1):385–393.

Lombardo, L. (2015). *Optimizing stochastic susceptibility modelling for debris flow landslides: model exportation, statistical techniques comparison and use of remote sensing derived predictors. Applications to the 2009 Messina event.* Doctoral thesis, University of Palermo, in cotutela with Institute of Geography - Eberhard Karls Universität Tübingen, Palermo, Italy. Supervisors: Prof. Enrico Di Stefano, Prof. Edoardo Rotigliano, Prof. Volker Hochschild.

Lombardo, L., Opitz, T., Ardizzone, F., Guzzetti, F., and Huser, R. (2020a). Space-time landslide predictive modelling. *Earth-Science Reviews*, 209:103318.

Lombardo, L., Opitz, T., Ardizzone, F., Guzzetti, F., and Huser, R. (2020b). Space-time landslide predictive modelling. *Earth-Science Reviews*, 209:103318.

Lombardo, L. and Tanyas, H. (2020). Chrono-validation of near-real-time landslide susceptibility models via plug-in statistical simulations. *Engineering Geology*, 278:105818.

Lu, A., Haung, W.-K., Lee, C.-F., Wei, L.-W., Lin, K.-H., and Chi, S.-C. (2020). Combination of rainfall thresholds and susceptibility maps for early warning purposes for shallow landslides at regional scale in Taiwan. *Advancing Culture of Living with Landslides*, pages 217–225.

Lu, N. and Godt, J. W. (2013a). Hillslope hydrology and stability.

Lu, N. and Godt, J. W. (2013b). Hillslope hydrology and stability.

Martelloni, G., Segoni, S., Fanti, R., and Catani, F. (2012). Rainfall thresholds for the forecasting of landslide occurrence at regional scale. *Landslides*, 9(4):485–495.

Masi, E. B., Segoni, S., and Tofani, V. (2021). Root reinforcement in slope stability models: A review. *Geosciences*, 11(5):212.

Mason, D. P. and Little, R. G. (2002). Debris flow advances and hazard assessment techniques. *Reviews in Engineering Geology*, 15:1–12.

Medina, V., Hürlimann, M., Guo, Z., Lloret, A., and Vaunat, J. (2021). Fast physically-based model for rainfall-induced landslide susceptibility assessment at regional scale. *Catena*, 201:105213.

Merghadi, A., Yunus, A. P., Dou, J., Whiteley, J., ThaiPham, B., Bui, D. T., Avtar, R., and Abderrahmane, B. (2020a). Machine learning methods for landslide susceptibility studies: A comparative overview of algorithm performance. *Earth-Science Reviews*, 207:103225.

Merghadi, A., Yunus, A. P., Dou, J., Whiteley, J., ThaiPham, B., Bui, D. T., Avtar, R., and Abderrahmane, B. (2020b). Machine learning methods for landslide susceptibility studies: A comparative overview of algorithm performance. *Earth-Science Reviews*, 207:103225.

Micheletti, N., Foresti, L., Robert, S., Leuenberger, M., Pedrazzini, A., Jaboyedoff, M., and Kanevski, M. (2014). Machine learning feature selection methods for landslide susceptibility mapping. *Mathematical Geosciences*, 46:33–57.

Milledge, D. G., Griffiths, D. V., Lane, S. N., and Warburton, J. (2014). A multidimensional stability model for predicting shallow landslide size and shape across landscapes. *Journal of Geophysical Research: Earth Surface*, 119(11):2481–2504.

Miralles, D. G. et al. (Unknown). Global land evaporation amsterdam model (gleam). Placeholder: Specific publication details for GLEAM not found in provided list.

Mirus, B. B., Bogaard, T., Greco, R., and Stähli, M. (2025). Invited perspectives: Integrating hydrologic information into the next generation of landslide early warning systems. *Natural Hazards and Earth System Sciences*, 25:169–182.

Montgomery, D. R. and Dietrich, W. E. (1994a). A physically based model for the topographic control on shallow landsliding. *Water Resources Research*, 30(4):1153–1171.

Montgomery, D. R. and Dietrich, W. E. (1994b). A physically based model for the topographic control on shallow landsliding. *Water Resources Research*, 30(4):1153–1171.

Moreno, M., Lombardo, L., Crespi, A., Zellner, P., Mair, V., Pittore, M., Van Westen, C., and Steger, S. (2024). Space-time data-driven modeling of precipitation-induced shallow landslides in south tyrol, italy. *Science of The Total Environment*, 912:169166.

Nagarajan, R., Mukherjee, A., Roy, A., and Khire, M. V. (1998). Landslide hazard and risk assessment using semi-quantitative methods in the vaitarna basin, maharashtra, india. *Environmental Geology*, 35(2-3):161–173.

Ng, C. W. W., Yang, B., Liu, Z. Q., Kwan, J. S. H., and Chen, L. (2021). Spatiotemporal modelling of rainfall-induced landslides using machine learning. *Landslides*, 18:2499–2514.

Nocentini, N., Melillo, M., Gariano, S. L., Peruccacci, S., Brunetti, M. T., and Guzzetti, F. (2024). Optimization of rainfall thresholds for landslide early warning through false alarm reduction and multi-source validation. *Landslides*, 21:1789–1804.

Osawa, H., Matsushi, Y., Matsuura, S., and Okamoto, T. (2024). Semiempirical modeling of the transient response of pore pressure to rainfall and snowmelt in a dormant landslide. *Landslides*, 21:245–256.

Ozturk, U., Bozzolan, E., Holcombe, E. A., Shukla, R., Pianosi, F., and Wagener, T. (2022). How climate change and unplanned urban sprawl bring more landslides. *Nature*, 608(7922):262–265.

Palau, R. M., Berenguer, M., Hürlimann, M., and Sempere-Torres, D. (2022). Application of a fuzzy verification framework for the evaluation of a regional-scale landslide early warning system during the January 2020 Gloria storm in Catalonia (NE Spain). *Landslides*, 19:1599–1616.

Park, J. Y., Lee, S. R., Lee, D. H., Kim, Y. T., and Lee, J. S. (2019). A regional-scale landslide early warning methodology applying statistical and physically based approaches in sequence. *Engineering Geology*, 260:105193.

Park, S. and Kim, J. (2013). Assessment of rainfall-induced shallow landslide susceptibility using a gis-based probabilistic approach. *Engineering Geology*, 161:1–15.

Patton, A. I. et al. (2023). Landslide initiation thresholds in data-sparse regions. *Natural Hazards and Earth System Sciences*, 23:3261–3281.

Pecoraro, G. and Calvello, M. (2021). Definition and first application of a probabilistic warning model for rainfall-induced landslides. *Advancing Culture of Living with Landslides*, pages 181–187.

Pereira, S., Zêzere, J. L., and Bateira, C. (2012). Assessing predictive capacity and conditional independence of landslide predisposing factors for shallow landslide susceptibility models. *Natural Hazards and Earth System Sciences*, 12(4):979–988.

Peruccacci, S., Brunetti, M. T., Gariano, S. L., Melillo, M., Rossi, M., and Guzzetti, F. (2023). The italian rainfall-induced landslides catalogue, an extensive and accurate spatio-temporal catalogue of rainfall-induced landslides in italy. *Earth System Science Data*, 15:2863–2877.

Pham, B. T., Pradhan, B., Tien Bui, D., Prakash, I., and Dholakia, M. B. (2016). A comparative study of different machine learning methods for landslide susceptibility

assessment: A case study of Uttarakhand area (India). *Environmental Modelling and Software*, 84:240–250.

Piciullo, L., Calvello, M., and Cepeda, J. M. (2018a). Territorial early warning systems for rainfall-induced landslides. *Earth-Science Reviews*, 179:228–247.

Piciullo, L., Calvello, M., and Cepeda, J. M. (2018b). Territorial early warning systems for rainfall-induced landslides. *Earth-Science Reviews*, 179:228–247.

Piciullo, L., Capobianco, V., and Heyerdahl, H. (2022). A first step towards a IoT-based local early warning system for an unsaturated slope in Norway. *Natural Hazards*, 114:3377–3407.

Ponziani, F., Pandolfo, C., Stelluti, M., Berni, N., Brocca, L., and Moramarco, T. (2012). Assessment of rainfall thresholds and soil moisture modeling for operational hydrogeological risk prevention in the umbria region (central italy). *Landslides*, 9:229–237.

Pyakurel, A., Dahal, B. K., and Gautam, D. (2023). Does machine learning adequately predict earthquake induced landslides. *Soil Dynamics and Earthquake Engineering*, 171:107994.

Quast, R., Wagner, W., Bauer-Marschallinger, B., and Vreugdenhil, M. (2023). Soil moisture retrieval from sentinel-1 using a first-order radiative transfer model—a case-study over the po-valley. *Remote Sensing of Environment*, 295:113651.

Reichenbach, P., Rossi, M., Malamud, B. D., Mihir, M., and Guzzetti, F. (2018a). A review of statistically-based landslide susceptibility models. *Earth-Science Reviews*, 180:60–91.

Reichenbach, P., Rossi, M., Malamud, B. D., Mihir, M., and Guzzetti, F. (2018b). A review of statistically-based landslide susceptibility models. *Earth-Science Reviews*, 180:60–91.

Reid, M. E., Christian, S. B., Brien, D. L., and Henderson, S. T. (2015).

Scoops3D—software to analyze 3D slope stability throughout a digital landscape. Techniques and Methods 14-A1, U.S. Geological Survey.

Roering, J. J., Schmidt, K. M., Stock, J. D., Dietrich, W. E., and Montgomery, D. R. (2003). The impact of hillslope-scale tree cover on terrain stability. *Geomorphology*, 55(1-4):147–165.

Roman Quintero, D. C. et al. (2023). Understanding hydrologic controls of sloping soil response to precipitation. *Hydrology and Earth System Sciences*, 27:4151–4172.

Rosi, A. et al. (2023a). Comprehensive landslide susceptibility map of central asia. *Natural Hazards and Earth System Sciences*, 23:2229–2249.

Rosi, A., Frodella, W., Nocentini, N., Caleca, F., Havenith, H. B., Strom, A., Saidov, M., Bimurzaev, G. A., and Tofani, V. (2023b). Comprehensive landslide susceptibility map of Central Asia. *Natural Hazards and Earth System Sciences*, 23(6):2229–2250.

Rosi, A., Segoni, S., Canavesi, V., Monni, A., Gallucci, A., and Casagli, N. (2021). Definition of 3D rainfall thresholds to increase operative landslide early warning system performances. *Landslides*, 18:1045–1057.

Rossi, G., Catani, F., Leoni, L., Segoni, S., and Tofani, V. (2013). HIRESSS: a physically based slope stability simulator for HPC applications. *Natural Hazards and Earth System Sciences*, 13(1):151–166.

Rossi, M., Guzzetti, F., Reichenbach, P., Mondini, A. C., and Peruccacci, S. (2010). Optimal landslide susceptibility zonation based on multiple forecasts. *Geomorphology*, 114(3-4):129–142.

Sahin, E. K. (2022). Comparative analysis of gradient boosting algorithms for landslide susceptibility mapping. *Geocarto International*, 37(9):2441–2465.

Schaller, C. et al. (2025). Predicting the thickness of shallow landslides in switzerland using machine learning. *Natural Hazards and Earth System Sciences*, 25:467–488.

Schellekens, J., Kramer, T., van Klink, M., van der Schalie, R., Malbeteau, Y., Geers, A., and de Jeu, R. (2022). A 1km experimental dataset for the mediterranean terrestrial region of soil moisture, land surface temperature and vegetation optical depth from passive microwave data.

Schilirò, L., Rossi, M., Polpetta, F., Fiorucci, F., Fortunato, C., and Reichenbach, P. (2023). A web-based GIS (web-GIS) database of the scientific articles on earthquake-triggered landslides. *Natural Hazards and Earth System Sciences*, 23(5):1789–1804.

Schwarz, M., Preti, F., Giadrossich, F., Lehmann, P., and Or, D. (2010). Quantifying the role of vegetation in slope stability: A case study in tuscany (italy). *Ecological Engineering*, 36(3):285–291.

Segoni, S., Piciullo, L., and Gariano, S. L. (2018a). A review of the recent literature on rainfall thresholds for landslide occurrence. *Landslides*, 15(8):1483–1501.

Segoni, S., Rosi, A., Lagomarsino, D., Fanti, R., and Casagli, N. (2018b). Brief communication: Using averaged soil moisture estimates to improve the performances of a regional-scale landslide early warning system. *Natural Hazards and Earth System Sciences*, 18(3):807–812.

Semnani, S. J., Han, Y., Bonfils, C. J., and White, J. A. (2025). Assessing the impact of climate change on rainfall-triggered landslides: a case study in california. *Landslides*, 22:1707–1724.

Shah, S. K. H., Malik, A. A., Haq, S., et al. (2025). Effect of moisture change on water retention behavior of unsaturated silty soil under loading–unloading conditions. *Discover Civil Engineering*, 2:7.

Sidle, R. C. and Bogaard, T. A. (2006). A distributed slope stability model for steep forested basins. *Water Resources Research*, 42(9).

Smith, H., Neverman, A., Betts, H., and Spiekermann, R. (2023). The influence of spatial patterns in rainfall on shallow landslides. *Geomorphology*, 437:108795.

Sousa, I. A. et al. (2023). Development of a soil moisture forecasting method for a landslide early warning system (lews): Pilot cases in coastal regions of brazil. *Journal of South American Earth Sciences*, 131:104631.

Stoffelen, A. (1998). Toward the true near-surface wind speed: Error modeling and calibration using triple collocation. *Journal of Geophysical Research: Oceans*, 103:7755–7766.

Strząbała, K. et al. (2024). Remote sensing techniques for landslide prediction, monitoring, and early warning: recent advances and trends. *Remote Sensing*, 16:2781.

Sun, D. et al. (2023). Landslide susceptibility mapping based on interpretable machine learning from the perspective of geomorphological differentiation. *Land*, 12:1018.

Terzaghi, K. (1950). *Mechanism of Landslides*. Geological Society of America.

Van Westen, C. J., Castellanos, E., and Kuriakose, S. L. (2008). Use of geomorphological information in indirect landslide susceptibility assessment. *Natural Hazards*, 30(3):399–419.

Varnes, D. J. (1978). Slope movement types and processes. pages 11–33.

Wagner, W., Hahn, S., Kidd, R., Melzer, T., Bartalis, Z., Hasenauer, S., and Rubel, F. (2013). The ascat soil moisture product: A review of its specifications, validation results, and emerging applications. *Meteorologische Zeitschrift*, 22:5–33.

Wicki, A., Jansson, P.-E., Lehmann, P., Hauck, C., and Stähli, M. (2021). Simulated or measured soil moisture: Which one is adding more value to regional landslide early warning. *Hydrology and Earth System Sciences*, 25:4585–4610.

Yang, X. et al. (2024). Mechanical behavior of unsaturated soils from suction-controlled shear tests. *Engineering Geology*, 322:107295.

Yao, Y. et al. (2025). Advanced soil moisture monitoring for unsaturated slopes: sensors, geophysics, and integration for early warning. *Water*, 17:390.

Zheng, C., Jia, L., and Zhao, T. (2023). A 21-year dataset (2000–2020) of gap-free global daily surface soil moisture at 1-km grid resolution. *Scientific Data*, 10:139.